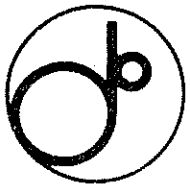

KEK Internal 80-1
May 1980
I/B

KENS REPORT I

February 1980

edited by

Yoshikazu ISHIKAWA

NATIONAL LABORATORY FOR
HIGH ENERGY PHYSICS

National Laboratory for High Energy Physics, 1980

KEK Reports are available from

Technical Information Office
National Laboratory for High Energy Physics
Oho-machi, Tsukuba-gun,
Ibaraki-ken, 305
JAPAN

Phone: 0298-64-1171
Telex: 3652-534 (Domestic)
(0)3652-534 (International)
Cable: KEKOHO

Preface

This KENS Report is the first research report published at KEK (National Laboratory for High Energy Physics) after the construction of the KENS facility (the spallation neutron source facility at KEK) was started. We collect in it the papers discussing the results of the mock-up experiments and computer simulation calculations performed for the technical development in connection with the construction of the KENS facility as well as the papers describing the details of the spectrometers which are going to be installed at KENS. The experimental results obtained with the Tohoku Linac Neutron Source are also included only for the case where the experiments were practiced for the development of new techniques. This report, thus, summarizes the progress we have made in this year as an extention of a previous KEK report (KEK-78-19).

The most of papers in this report were presented in the Informal ICANS meeting at Rutherford Laboratory on September 10-12, 1979. Therefore the report can also be served as the Proceedings of the meeting prepared by Japanese group. In this connection we thank the Japan Society for the Promotion of Science which supported this meeting and made the Japanese participants attend it.

The first stage of construction of the KENS facility will be accomplished at the end of March, 1980. We expect to have neutron beams in July until when we hope to complete the data collection system. The test experiments will start from September in the earliest case.

We are going to have the 4th ICANS meeting on October 20-24, 1980 at KEK and the results of discussions in this meeting will be published in the next KENS Report. The original papers concerning the experimental results obtained at KENS facility will be published hereafter as KEK Report B. If you are interested in receiving continuously these reports, please contact with either Prof. N. Watanabe, National Laboratory for High Energy Physics, or me.

Yoshikazu ISHIKAWA
Professor of Physics,
Tohoku University and National
Laboratory for High Energy Physics

Content

1. Present status of construction of KENS facility

H. Sasaki, N. Watanabe and Y. Ishikawa*

National Laboratory for High Energy Physics, Tsukuba

* Physics Department, Tohoku University, Sendai

1.1 Proton beam transportation

The KEK proton accelerator complex is a cascade machine of two synchrotrons, a 12 GeV main synchrotron and a 500 MeV fast cycling booster synchrotron. Three quarters of the delivering capability of the proton beam from the booster are available for other purposes than the main ring injection without disturbing its operation. Utilization of such an excess of the beam pulses has been discussed for a long period among many scientists in various fields of researches, such as nuclear physics, neutron physics, radiation science and medicine. Three projects were finally proposed; neutron scattering experiments, meson physics and medical use. Booster Synchrotron Utilization Facility (BSF) has been established to organize these projects at the beginning of 1978 fiscal year. The project of the neutron scattering experiments with pulsed neutrons was approved by the government in 1977 and its construction was started. The meson project, which is promoted by Meson Science Laboratory in the University of Tokyo, was also approved in 1978. The proposal of medical use of the booster beam was submitted to the government through Tsukuba University and is also approved in 1980. The first stage of the construction of the facility will

be completed at the first half of 1980. The layout of the facility is shown in Fig.1. The construction of the building including the electric and cooling plants for the facility was started in August 1978 and finished at the end of 1979.

In 1977, the booster beam had been separated from the main ring injection course and transferred to a beam dump located outside of the main ring enclosure. The beam line, which supplies the booster beam to the new facility, extends from the beam dump. After passing through a 40 m long transporting section, the beam is switched to any experimental areas by means of a pulsed switching magnet PHB2 synchronizing to the repetition of the booster synchrotron. By turning off the magnetic field, the beam hits directly the pulsed neutron source for the neutron scattering experiments. By choosing the polarity of the magnetic field, the beam can be switched to the meson experimental area or to the secondary proton beam line for the medical use. The beam line consists of a matching section (Q13 to Q19) and several sets of π-section (Q20 to Q23, Q24 to Q27, Q28 to Q31, Q24, 25, 26M, 27M and Q24, 25, 26P, 27P). The matching section is designed so that the output beam of the beam-dump line is matched to the beam profile required at the neutron and meson production target. The beam is focussed at a point located between Q19 and Q20, and then transferred to the neutron or meson production target through π-sections. Each π-section is basically a quartet system composed of four quadrupole magnets in series connection. Fig.2 shows the betatron amplitude and dispersion functions of this beam line.

Various kinds of magnet (23 quadrupole magnets, 2 bending magnets, one pulsed bending mgnet for beam switching, and 9 steering magnets) and their power supplies for the beam transport line were manufactured and set. Length and bore radius of the quadrupole magnet are 30 cm and 5.7 cm

respectively. Typical distribution of the field gradient are shown in Fig.3, where the field gradient is obtained by measuring directly the error fields of the quadrupole field and integrating them with respect to the horizontal displacement x. To realize a linear effective length of the field gradient over a wide range by simple procedure, end-cut correction of the pole is carried out by cutting the end of pole with a plane. The effect of the correction on the effective length is also shown in Fig.3.

All the vacuum vessels including bellows of the beam line are made of aluminium alloy except a ceramic chamber for the pulsed bending magent. From the viewpoint of the residual radioactivities induced by exposing 500 MeV proton beam, aluminium is considerably preferable to stainless steel, though the latter is popular in manufacturing vacuum vessels. With exposure time of ten days, for example, aluminium shows the residual activities of 1/4 ∿ 1/30 two days after turning off the beam or 1/60 ∿ 1/230 for eight days as compared with those of stainless steel. Al-Mg alloy and Al-Cu alloy are applied to the body and the flange for the vessels respectively. The welding technique between those kinds of material is established at present even though accompanying some difficulties. Metal gaskets Helicoflex are in use to seal vacuum.

The beam monitor system of the beam line consists of eleven beam profile monitors and six intensity monitors. It is possible to measure the beam emittance with proper combination of the profile monitors giving no disturbance to the beam transportation. Manufacturing of most of these monitors was completed.

The system for the beam line control, the access control and the radiation protection for personnel are now under construction and will be almost completed at the end of this fiscal year. The beam line control

is divided into three parts such as, beam injection control, ON/OFF and UP/DOWN of magnet power supplies and timing control. 5TI programmable sequence controller (sequencer) is used for sequence control. After accepting the beam request status from the experimental facilities, a sequencer checks all the conditions concerning the beam injection and determines the beam delivery mode. The signals of the beam delivery mode are fed to the control desk and the timing system. The timing system generates a triggering pulse to PHB2 power supply at a programmed timing. The MELCOM-70 mini-computer system is used for the control of magnet power supplies, data-taking and displaying the beam profile and any other informations on BSF status on graphic display unit or CRT and also recording the acquired data.

Beam line tunnel, experimental areas and transfer tunnels are all controlled areas. All doors to those areas are usually locked electrically. Access to those areas is possible by means of a key to release the electric lock. Personal keys are set to a key board. When the key is released, the beam switch of the control desk can not be turned on. The radioactive contamination of personnels or equipments is checked with a gate monitor, which is located at the entry to the primary beam line.

The first beam will be delivered to the facility in the middle of 1980.

1.2 Neutron scattering facility (KENS)

The layout of the KENS facility determined is displayed in Figs.4 and 5. Note that this layout includes only the spectrometers for which the approval for construction has been obtained. The facility is composed of three big rooms. The neutron source is located nearly at the center of one big room - the main experimental hall (Fig.4). The room is practically

divided into two areas A and B by the biological shield. This is mainly for the experiments with thermal and epithermal neutrons. Another long room (Fig.5) is the experimental area for cold neutrons. In addition to these two experimental areas, there is a room for data processing and control where the main computer as well as the interfaces to connect the computer to each spectrometer will be accommodated (cf. Fig.4). The whole building with the internal facilities as electricity and water supply was completed in November 1979.

The present status of construction of each item of the KENS facility is summaried as below.

1. Target station

The KENS target assembly consists of a target, two kinds of moderator, Be reflector and their shieldings. The tungsten target with its cooling system and the Be reflector about 200 kg in weight had been manufactured in 1977 and a mechanical system to combine them was constructed in 1978. The whole assembly is going to be set on a movable target station in order to remove backward the target assembly from the center of the biological shield to the target handling area. Figure 6 displays the frame structure of the target assembly. They are made by aluminium metal to reduce the induced radio activity as much as possible. The design of the target handling system is now in progress and will be completed until the end of June 1980.

2. Biological shield

The biological sheild for the KENS is composed of two parts, the fixed shield mainly made of heavy concrete with fourteen beam tubes in

it and the movable part made of the iron and concrete blocks. Except three tubes into which the neutron guide tubes for cold neutrons are inserted, each beam tube is equipped with a 0.9 m long iron shutter which moves in the vertical direction. The shutter cases to accommodate these shutters can also be removed upwards like other movable shield blocks. Figures 7 (a), (b) and (c) are the cross sectional view of the shield actually constructed. It is really admirable that the large movable shield blocks ($2.3 \times 3.2 \times 3\ m^3$) composed of more than 30 pieces of blocks was set within an accuracy of 3 mm in the fixed shield.

3. Cold neutron source

The cold neutron moderator installed at KEK was decided to be made of a solid mathane plate of $13^W \times 5^D \times 15^H\ cm^3$ which is placed in the upper side of the target. The moderator is cooled down to 20°K by circulation of helium gas which is cooled by a small cryogenerator with a cooling power of 25 W at 20°K (PGH 105). The moderator and a heat exchanger are encased in a small vacuum vessel 280 mm in height and 190 mm in the maximum diameter which will be installed inside the target assembly. The distance between the moderator bottom to the upper surface of the target was designed to be 17 mm. The details of the cold neutron source are described in 2.1 of this report.

4. Cold neutron guide tubes

Three neutron guide tubes to transport cold neutrons to the cold neutron experimental area were designed. Each guide tube consists of three parts, a 3.5 m long straight section inside the biological shield, a curved section with a cross section of $20 \times 50\ mm^2$ and a radius of

curvature of 820 m, which is 9 m long and is placed inside the concrete shield and a section to the spectrometer. Ni float glass made by Nippon Sheet Glass Co. was used for the neutron reflector. The curved section is a composite of 1 m long straight section. A simulation calculation had also been performed to estimate the spacial and energy distribution of neutrons at the exit of the guide tube. The results are presented in 3 of this report.

The tail cutters to pass only the neutrons with wave lengths ranging between 4 Å and 12 Å were also constructed. The tail cutter, incorporated with our pulsed neutron source operating at 20 Hz, enables us to obtained a quasi-continuous neutron beam at the end of 25 m flight path. The beam cutting was practiced by rotating at 20 Hz a Cd coated disk 40 cm in diameter with a proper window at the position of 5 m far from the neutron source. The synchronization of the rotation of the chopper with the neutron pulse was achieved by using a high power stepping motor (Tōyō plat: PM 5-60: 360 deg/250 pulse) which was operated with the 5 kHz pulses supplied by a pulse generator synchronizing the repetition of the booster synchrotron. The phase of the chopper also controlled by the proton beam pulse.

5. Spectrometers

In the first stage of construction five spectrometers and their data acquisition systems have been constructed. The details of them are discussed in the section 4 and 5 of this report.

Figure Captions

Fig.1 Layout of KEK Booster Synchrotron Utilization Facility.

Fig.2 Betatron amplitude and dispersion functions of the booster beam line.

Fig.3 Field gradient distribution and effective length of the quadrupole magnets for the booster beam line.

Fig.4 KENS neutron scattering facility, Neutron experimental area A and B.

Fig.5 KENS neutron scattering facility, Cold neutron experimental area.

Fig.6 A picture of the movable target station together with a part of the target asembly.

Fig.7 A picture of the movable shield assembly.

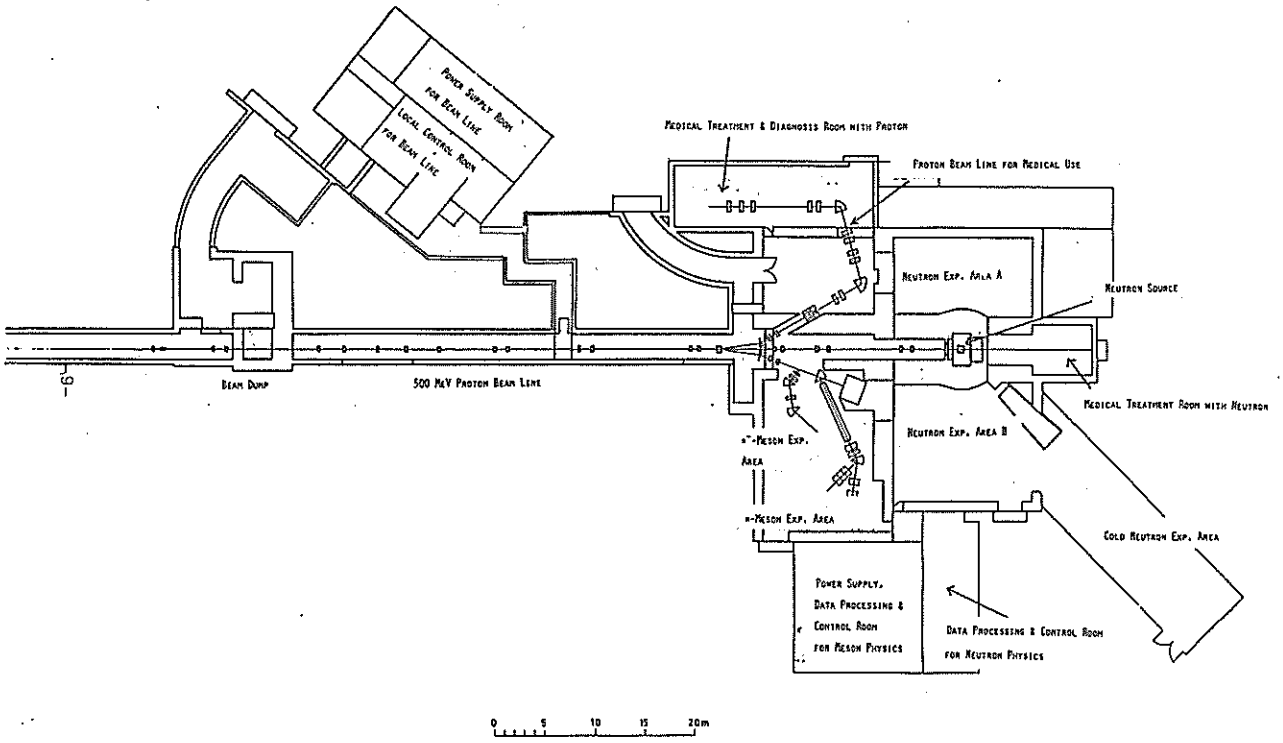
Power Supply Room for Beam Line
Local Control Room for Beam Line
Medical Treatment & Diagnosis Room with Proton
Proton Beam Line for Medical Use
Neutron Exp. Area A
Neutron Source
Beam Dump
500 MeV Proton Beam Line
Medical Treatment Room with Neutron
π⁺-Meson Exp. Area
Neutron Exp. Area B
π⁻-Meson Exp. Area
Cold Neutron Exp. Area
Power Supply, Data Processing & Control Room for Meson Physics
Data Processing & Control Room for Neutron Physics
0 5 10 15 20m

Fig. 1

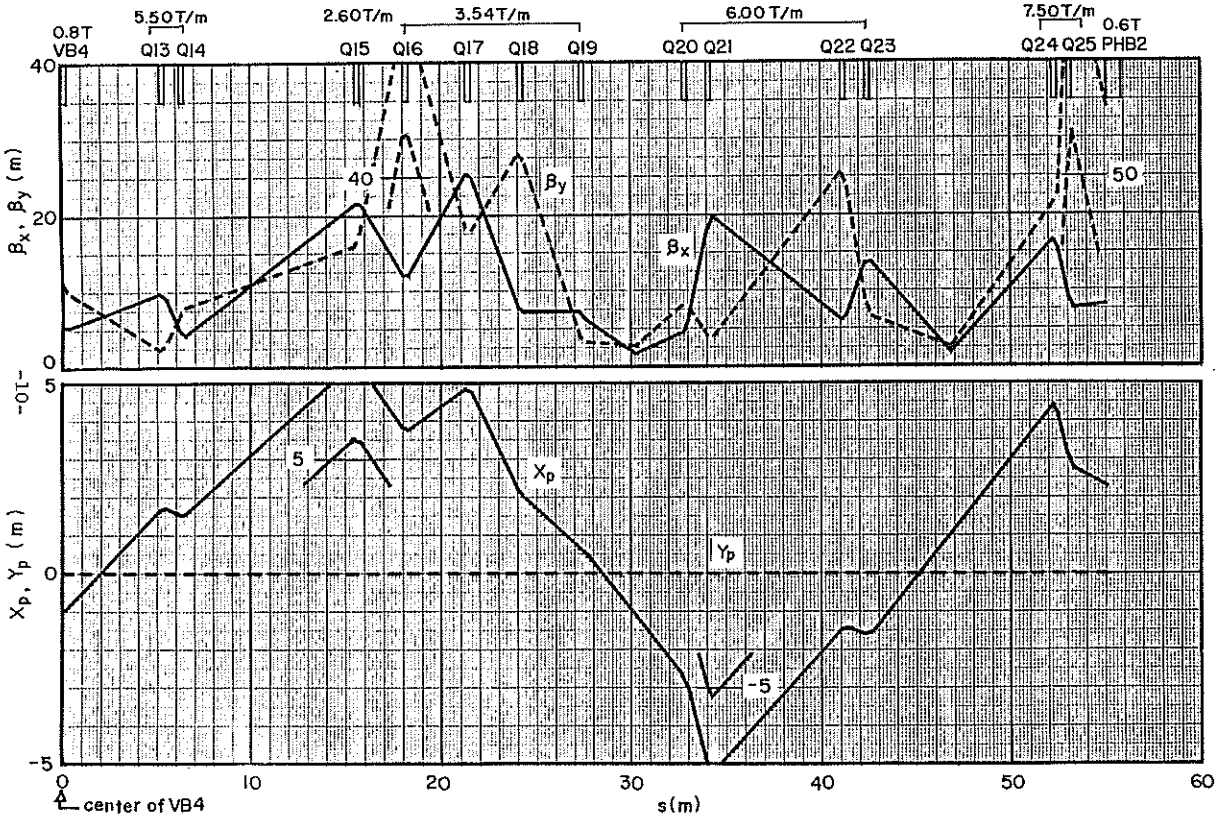
0.8T VB4
5.50T/m Q13 Q14
2.60T/m Q15
3.54T/m Q16 Q17 Q18 Q19
6.00T/m Q20 Q21 Q22 Q23
7.50T/m Q24 Q25
0.6T PHB2
40
20
0
β_x, β_y (m)
β_y
β_x
50
5
-5
X_p, Y_p (m)
X_p
Y_p
0 10 20 30 40 50 60
s(m)
center of VB4

Fig. 2(a)

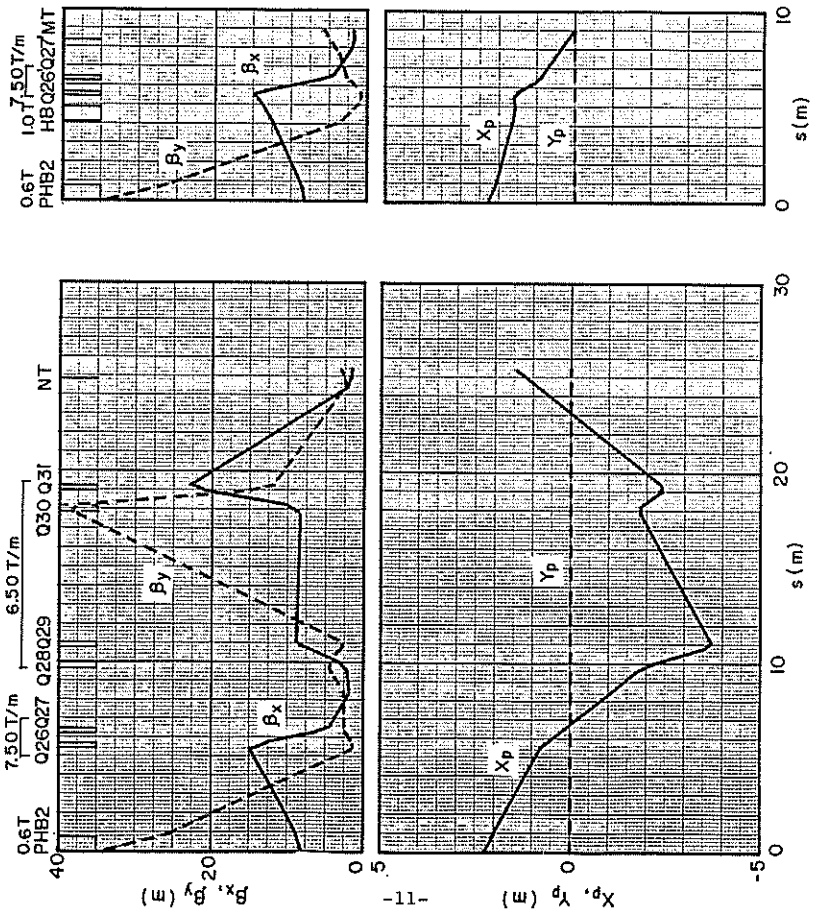
0.6T PHB2
7.50 T/m HBQ26Q27MT
β_x
β_y
X_p
Y_p
s (m)
7.50 T/m Q26Q27
Q28Q29
6.50 T/m
Q30 Q31
NT
β_x, β_y (m)
X_p, Y_p (m)

Fig. 2(b)

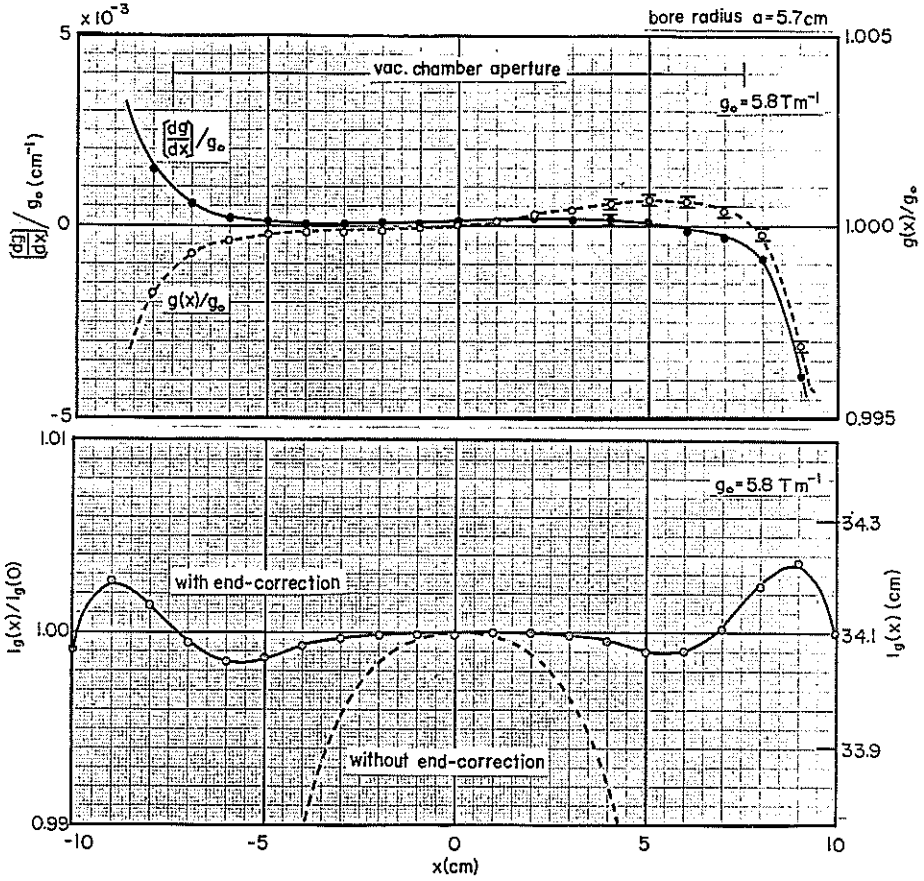
x10^{-3}
bore radius a=5.7cm
vac. chamber aperture
g_o=5.8Tm^{-1}
$\frac{dg}{dx}/g_o$
g(x)/g_o
$\frac{dg}{dx}/g_o$ (cm^{-1})
g(x)/g_o
g_o=5.8 Tm^{-1}
with end-correction
without end-correction
$l_g(x)/l_g(0)$
$l_g(x)$ (cm)
x(cm)

Fig. 3

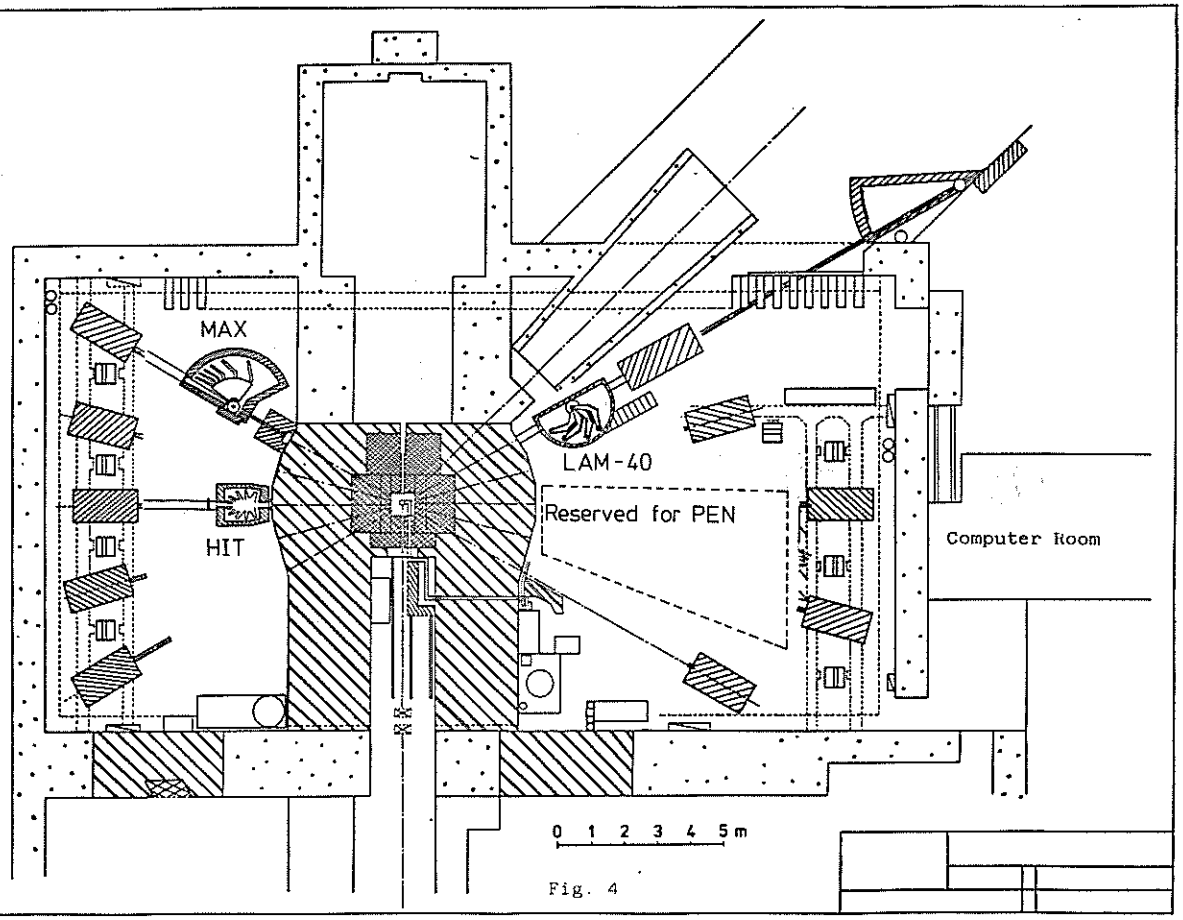
MAX
HIT
LAM-40
Reserved for PEN
Computer Room
0 1 2 3 4 5m

Fig. 4

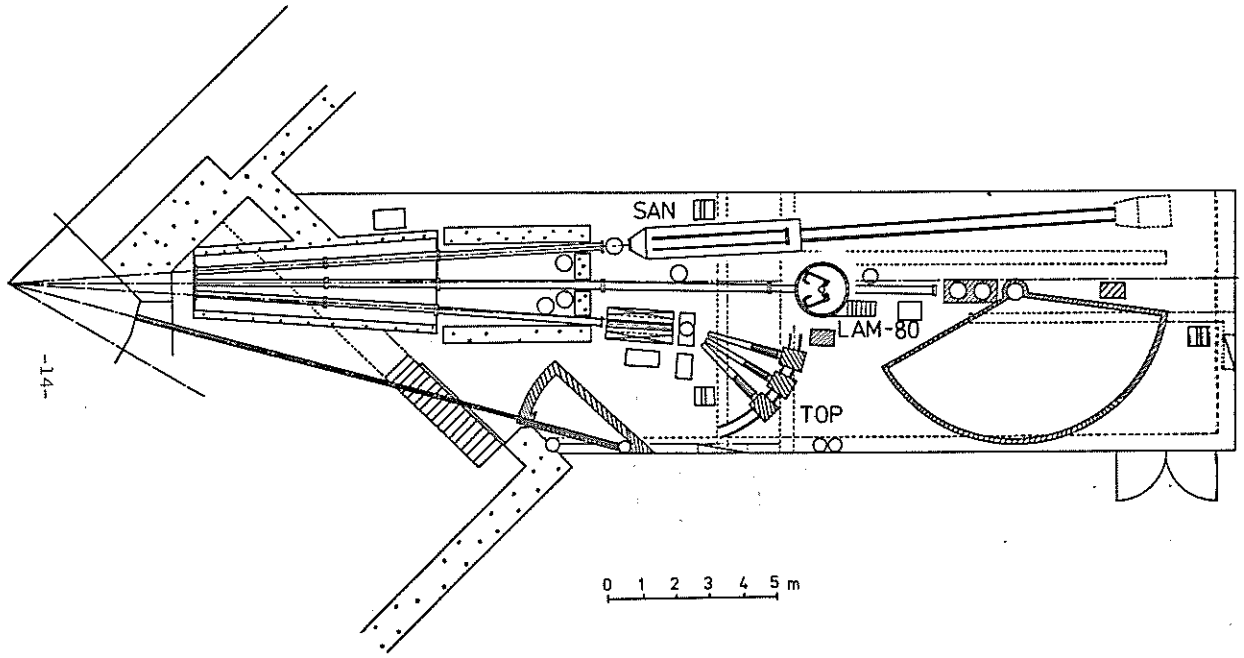
SAN
LAM-80
TOP
0 1 2 3 4 5m

Fig. 5

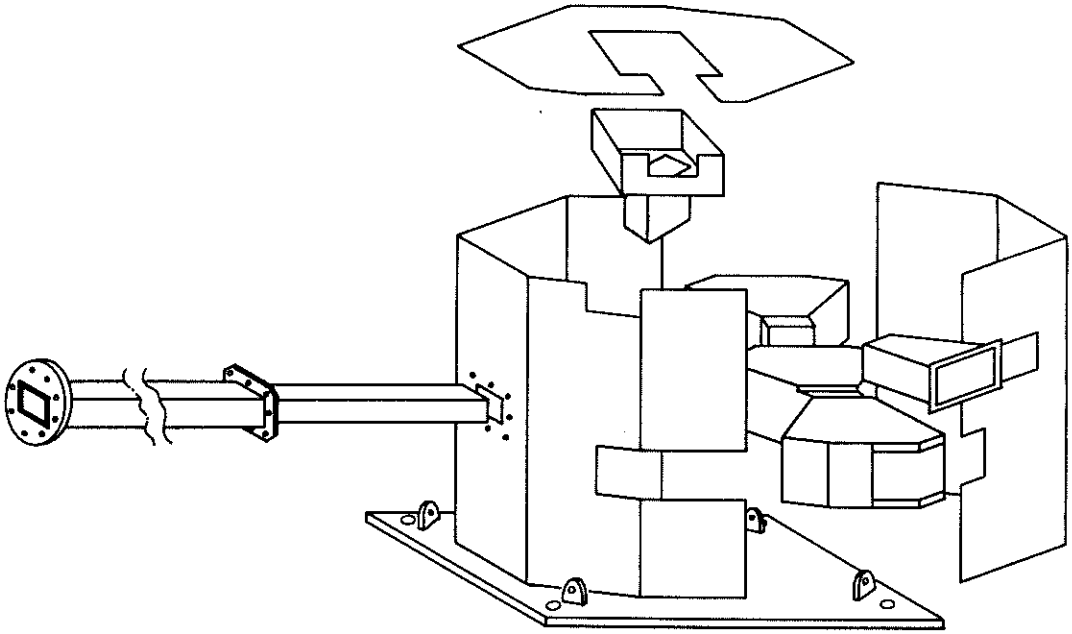

Fig. 6

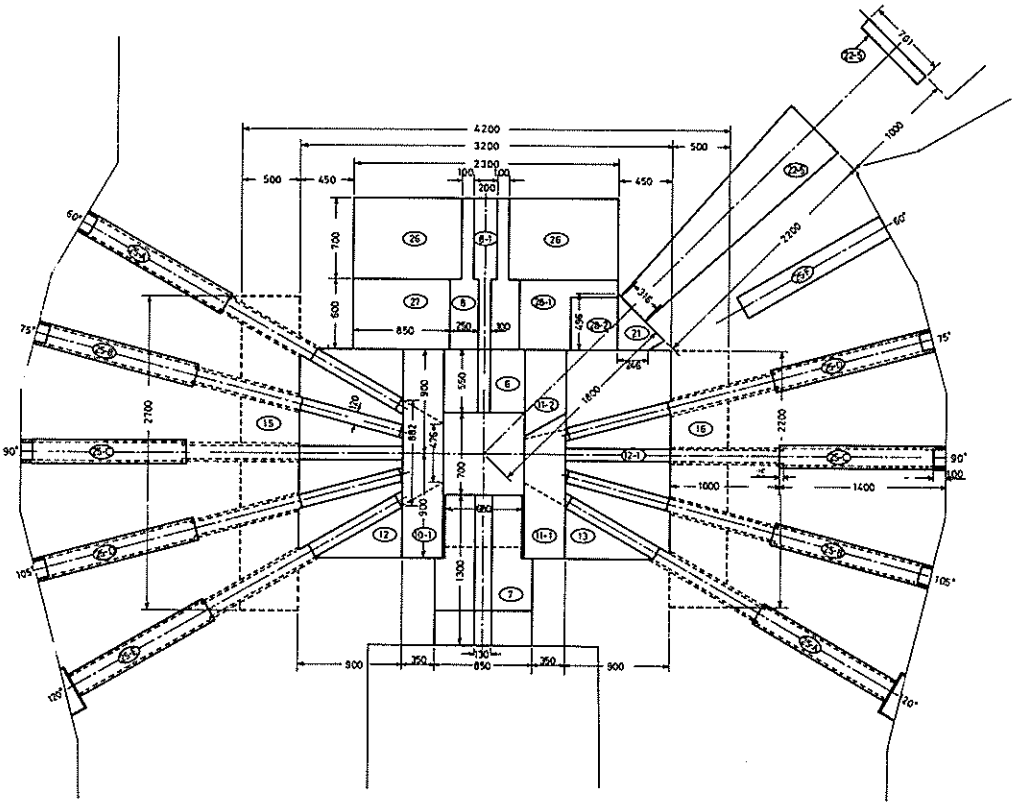
4200
3200
2300
500
450
100
200
700
600
850
750
300
2700
2200
1000
1400
900
350
650
130
60°
75°
90°
105°
120°

Fig. 7(a)

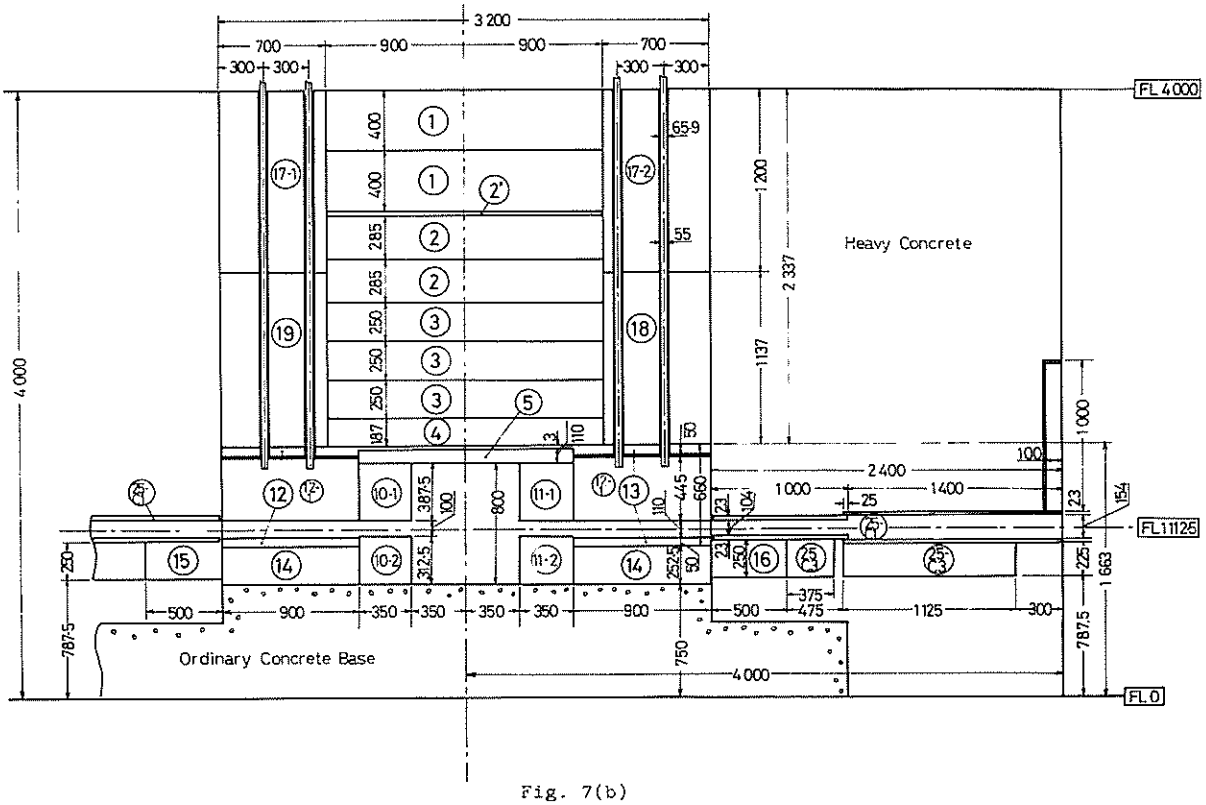
3 200
700
900
900
700
300
300
300
300
FL 4000
FL 11125
FL 0
Heavy Concrete
Ordinary Concrete Base
4 000
2 337
1200
1137
1000
2400
1400
1000
100
25
154
1663
787.5
750
500
900
350
350
350
350
900
500
475
1125
300
375

Fig. 7(b)

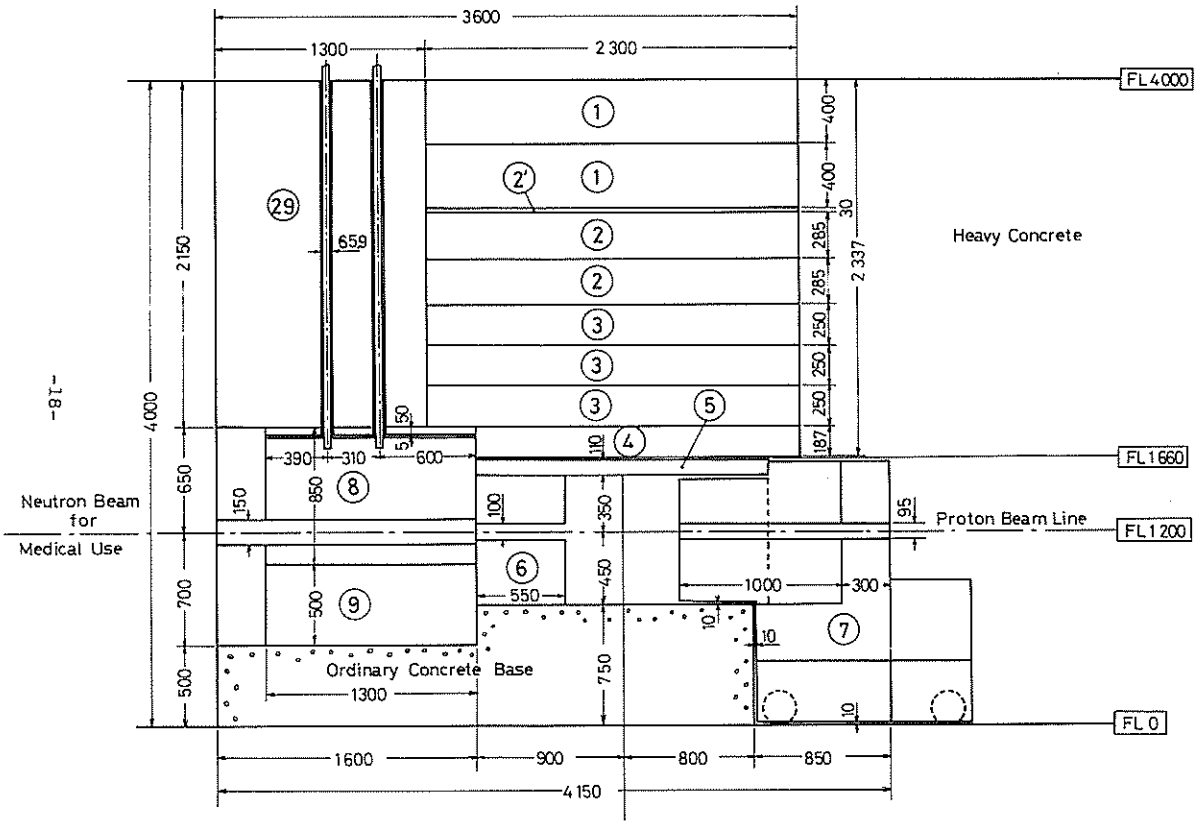
3600
1300
2 300
FL 4000
FL 1660
FL 1200
FL 0
Heavy Concrete
Proton Beam Line
Neutron Beam
for
Medical Use
Ordinary Concrete Base
4000
2150
650
700
500
2 337
1300
1600
900
800
850
4 150
750
550
1000
300
390
310
600

Fig. 7(c)

2. Cold neutron source

2.1 Cold Neutron Source

Mock-up experiment and final design

Y. Ishikawa and S. Ikeda*

Physics Department, Tohoku University, Sendai

§1. Introduction

This report describes the outline of the mock-up experiment of the cold neutron source performed in the beam dump room of KEK using 500MeV protons from the KEK booster synchrotron and that of the final design of the cold neutron source system of the KEK neutron source facility. The mock-up experiment was aimed to evaluate the radiation heating by spallation neutrons in the cold moderator (solid methane at 20K) and to test the cooling ability of the designed cryostat for the cold moderator. This kind of information is quite important because we need to place the cold moderator as close as possible to the target to increase the neutron yields which inevitably requires to minimize the cryostat size. Various other kinds of mock-up experiments have also been carried out to find the optimized size of the moderator as well as to establish the method for cooling to get a dense solid methane moderator. The results have been published in an interim technical report[1] (in Japanese)

* Present address: National Laboratory for High Energy Physics
Oho-machi, Tsukuba-gun, Ibaraki

§2. Mock-up experiment

The cold moderator cryostat used in the mock-up experiment is shown in Fig. 1. The cryostat was designed as a prototype of the KENS cold neutron source. The moderator case with an outersize of $100^{W} \times 110^{H} \times 50^{D}$ mm^3 made of pure Al metal was cooled through a heat exchanger (copper block) attached to the top of the box. The cryostat was placed on a tungsten target with a dimension of $78^{W} \times 57^{H} \times 120^{L}$ mm^3. In this configuration the minimum distance between the cold moderator and the target is 12mm. The heat exchanger block was cooled by circulation of liquid helium through a 10m long transfer tube. In the experiment mesitylene ($C_6H_4(CH_3)_3$) which has a similar characteristic as methane for the cold moderator[2] was used for simplicity of handling and safety, because it keeps the liquid state even at room temperature. The target was cooled by air blowing using a hair drier.

The experimental results obtained were summarized in Fig. 2. The temperature of the bottom of the cold moderator T_1 was attained to 12 K which was found to rise up to 13.5K, when the 500 MeV proton beams (4.9×10^{11}p.p.p, $4H_Z$) were sent to the target and the spallation neutrons were created. Since the temperature increase occurred almost instantaneously, the moderator was expected to be heated up homogenously by the radiation. Otherwise it should take a time before the moderator arrives at an equilibrium state. The figure also shows that the temperature increase of the wall of the

moderator case was quite few, suggesting the heating is due to the spallation neutrons entered inside the moderator. From this experiment, we could evaluate i) the cooling power of the cold transfer system necessary for the cold neutron source and ii) the value of radiation heating by spallation neutrons which is described below.

2.1. Cooling power of the cold transfer system

In a process of the mock-up experiment, it was found that a flow of 6ℓ/hr of liquid He was necessary to keep the moderator at the lowest temperature. We also found that the moderator temperature rose up to 40K, if the flow rate was decreased to be 2ℓ/hr. If we assume that the temperature of helium gas arises to 10K at the exit of the heat exchanger, the circulation of 6ℓ/hr of liquid He has an effective cooling power Q(watt) given by

$$\begin{aligned} Q &= (25\text{cal/mol}+30\text{cal/mol})\times 6\ell/\text{hr}\times 31.25\text{mol}/\ell \\ &= 10308\text{cal/h} \\ &= 12\text{watt}. \end{aligned} \tag{1}$$

On the other hand the heat loss of this cold moderator system was evaluated to be 5watt, in consistent with the experimental observation that the flow rate of 2ℓ/hr(Q=4watt) is not enough to keep the lowest temperature. Therefore the cold transfer system should have a cooling power of more than 12watt. In Fig. 3 is shown the cooling power of PGH105; a small cold transfer system (fabricated by N.V. Philips' Gloeilamphenfabricken) plotted against the operating

temperature, which indicates that this system is sufficient enough to keep the cold neutron source similar to the prototype less than 20K.

2.2. The value of radiation heating

In order to estimate the heat produced by the spallation neutrons, we made an assumption that the heat uniformly produced in the moderator is removed through the nearest neighboring wall of the case. Then the equation of the heat flow is given by

$$q = \frac{d}{dx}\left(\kappa(T(x))\frac{dT(x)}{dx}\right), \tag{2}$$

where q is the heat produced in a unit volume, $\kappa(T(x))$ and $\frac{dT(x)}{dx}$ are the thermal conductivity and temperature gradient of the moderator at a distance x from the wall respectively. Since $\kappa(T)=K_1T$ near 20K, Eq(2) gives rise to a relation

$$q = K_1(T_1^2 - T_2^2)/\ell^2, \tag{3}$$

with T_2 and T_1 the temperature of the wall and that of the moderator at the farthest distance ℓ from the wall respectively. The thermal conductivity of solid mesithylen has been determined at 80K to be $\kappa(80)=1.2\times10^{-3}$ watt/cmdeg[3] and $\kappa(20)$ would be $(1/4)\kappa(80)\lesssim\kappa(20)\lesssim(1/2)\kappa(80)$. Therefore, K_1 was estimated by assuming $\kappa(20) \leq 0.6\times10^{-3}$ watt/cmdeg or $K_1 < 3\times10^{-2}$m watt/cmdeg^2. By putting ℓ=2.2cm, T_1=13.5K and T_2=12.0, we finally get

$$q \leq 0.24\text{m watt/cc}. \tag{4}$$

This estimate suggests that the maximum heat produced in the moderator by spallation neutrons of 19.6×10^{11}p/s is order of 0.2m watt. Since the cold moderator of KENS has a volume of 900cc and the proton beam intensity will be 4.9 times higher than that used in the mock-up experiment, the total heat Q_t produced in the cold moderator can be estimated to be

$$Q_t = 0.24 \times 900 \times 4.9 = 1.058 \text{ watt}, \qquad (5)$$

for the tungsten target. Therefore, in case of KENS cold moderator, the radiation heating by spallation neutrons is almost negligible compared with other kinds of heat losses and the cooling power of cold transfer system PGH 105 would be sufficient to keep the moderator below 20K even with uranium target. This radiation heating becomes significant if the intensity of spallation neutrons increases by 200 times, which is the case for SNS at Rutherford Laboratory. In this case the radiation heating would be order of 400watt and a big refrigerator is required.

§3. Final design of KENS cold neutron source

3.1 Cryostat for cold moderator

Based on the results of the mock-up experiments described in the technical report[1], the moderator size was determined to be $120^W \times 50^D \times 150^H$ mm^3. The moderator case was made of pure aluminium metal 4mm thick except one wall behind the surface from where the cold neutrons are emitted. This wall has a

thickness of 7mm to increase the thermal conduction. The heat exchanger has nearly the same structure as that of the test cryostat. Actual size of the cryostat as well as the configuration of the cold neutron source-target-Be reflector system is displayed in Fig. 4. The distance between the top surface of target and bottom of moderator is now 19mm and that between the cryostat wall and moderator is 5mm. The total height of the cryostat is 290mm and the most part of the cryostat is covered with Be reflector.

3.2. Cold neutron source assembly

The block diagram of the cold neutron source assembly is shown in Fig. 5. The assembly consists of the cooling system, the methane gas circulating system, the vacuum pump system and the safety control system. The cooling system is composed of the PGH 105, the cold helium gas transfer unit and the low temperature cryostat. The He gas cooled by the cryogenerator is transferred to the heat exchanger of the cryostat by the ventilator (6) in the figure through the 7m long transfer tube. The temperature of the cold moderator can be controlled at any temperature by heating He gas by a heater (9) at the entrance of the cryostat.

The methane gas circulating system is composed of a gas reservoir tank,530ℓ in volume, a 900cc cold moderator case and a methane high pressure vessel. The gas in the reservoir tank at atmospheric pressure is liquidized in the cold moderator and is solidified slowly by using the heater (9).

In order to prevent the entrance to the cold moderator case from freezing, its temperature is automatically controlled to be above 90K(10). The pressures gauges (4) and (5) in the system serve as an indicator to normal operation; the gauges should indicate zero pressure when the entrance to the cold moderator is not frozen and the condensation is complete.

The vacuum pump system provides with two vacuum pumps; one diffusion pump system for high vacuum (YH-350) and a rotary pump (PVD (80)) for low vacuum. Both of cryogenerator and cryostat are evacuated at the same time by these pumps, through three electric vacuum valves (1), (2) and (3) which are automatically controlled by vacuum pressure detected by a Penny type vacuum gauge (8). In normal operation all of these valves are closed.

In order to guarantee the safety in operation, the safety control system controls the assembly in following ways.

(i) When the vacuum pressure increases more than 1×10^{-4}mmHg, the electric vacuum valves (1) and (3) are opened automatically to evaculate the whole system by the diffusion pump.

(ii) If the pressure exceeds 1×10^{-2}mmHg, the valve (3) is closed and the valve (2) is opened The system produces an alarm signal to stop the opperation of the accelerator.

The same kind of the signal is produced in three following cases.

(iii) The temperature of the bottom of the cold moderator detected either by a hydrogen pressure gauge (13) or by a thermo-junction (12) exceeds a defined value.

(iv) The temperature of the cryogenerator (7) exceeds a defined value.

(v) An anomalous strain is introduced into the wall of the moderator case, which will be detected by a strain gauge (11) (future plane).

The layout of the cold neutron source assembly is displayed in Fig. 6. As is seen in the figure, the cryogenerator (refrigerator) which was originally planned to be placed inside the biological shield was finally decided to be installed outside of it in order to make easy the maintenance of the cryogenerator.

The cold neutron source assembly has been constructed by Osaka-Oxgen Industries Ltd. and a test experiment was performed to examine the cooling power. The results are shown in Fig. 7. which indicates that the moderator attained to the lowest temperature of 17K in an hour. Therefore the assembly was found to satisfy our requirement.

References

1). The construction of KENS and the neutron scattering with it Technical Report I.II edited by Y. Ishikawa (1978) 74

2). M. Utsuro, M. Sugimoto and Y. Fujita; Annu. Rep. Reactor Inst. Kyoto Univ. 8 (1975) 17

3). H. Takahashi; Experimental report for Bachelor thesis (1978)

Figure Caption

Fig.1. Prototype cryostat for cold neutron moderator used for mock-up experiments.

Fig.2. Results of mock-up experiment. The absolute values of T_2 and T_3; temperatures of aluminum case are not accurate compared with T_1 because of lack of accurate calibration for these thermo-junctions.

Fig.3. Cooling power of cold transfer system PGH 105.

Fig.4. Target-cold moderator-Be reflector assembly for the KEK neutron source.

Fig.5. Block diagram of KENS cold neutron source assembly.

Fig.6. Layout of cold neutron source assembly.

Fig.7. Result of test operation of cooling system of KENS cold neutron source. The minimum temperature of moderator attained is 17K.

Cold Neutron Moderator for Mock up Experiment

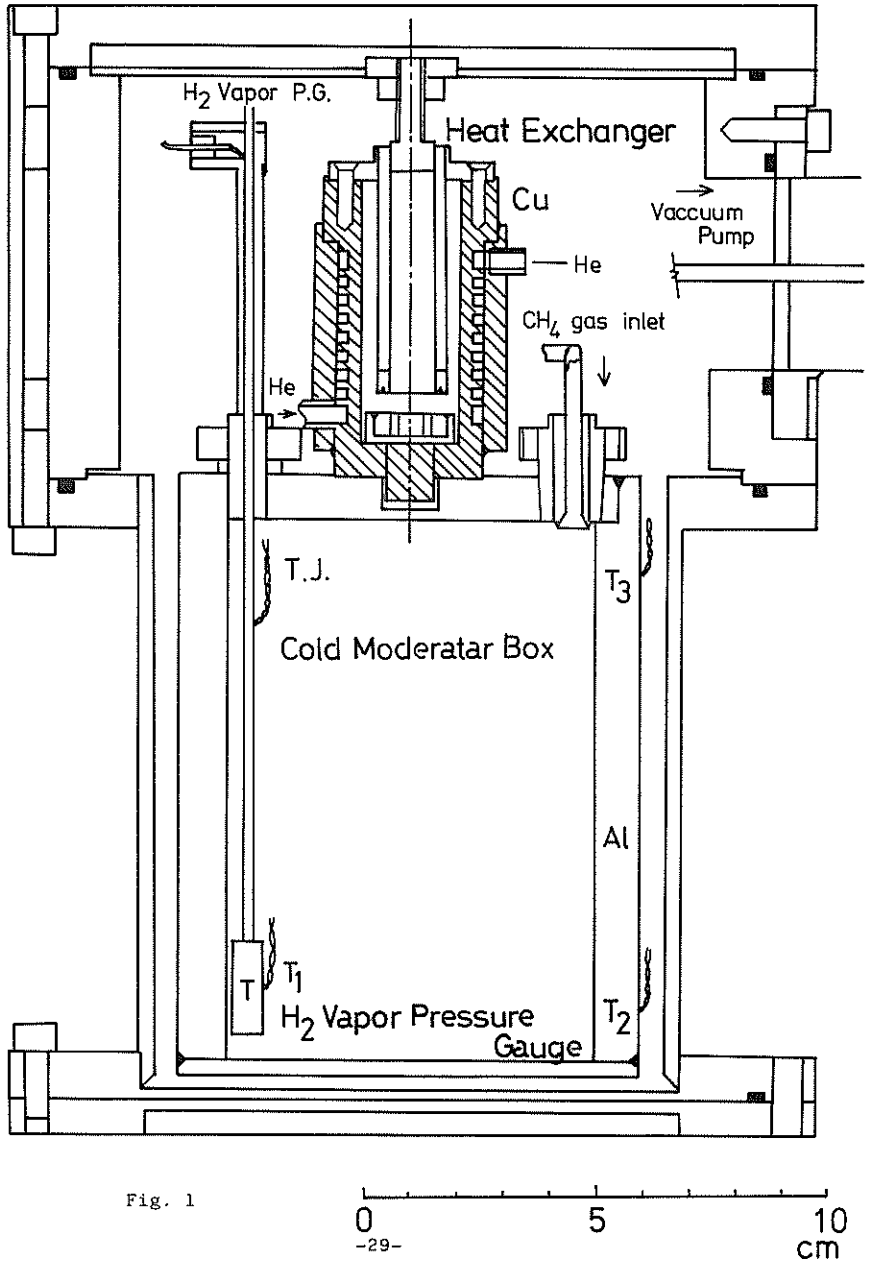

Fig. 1

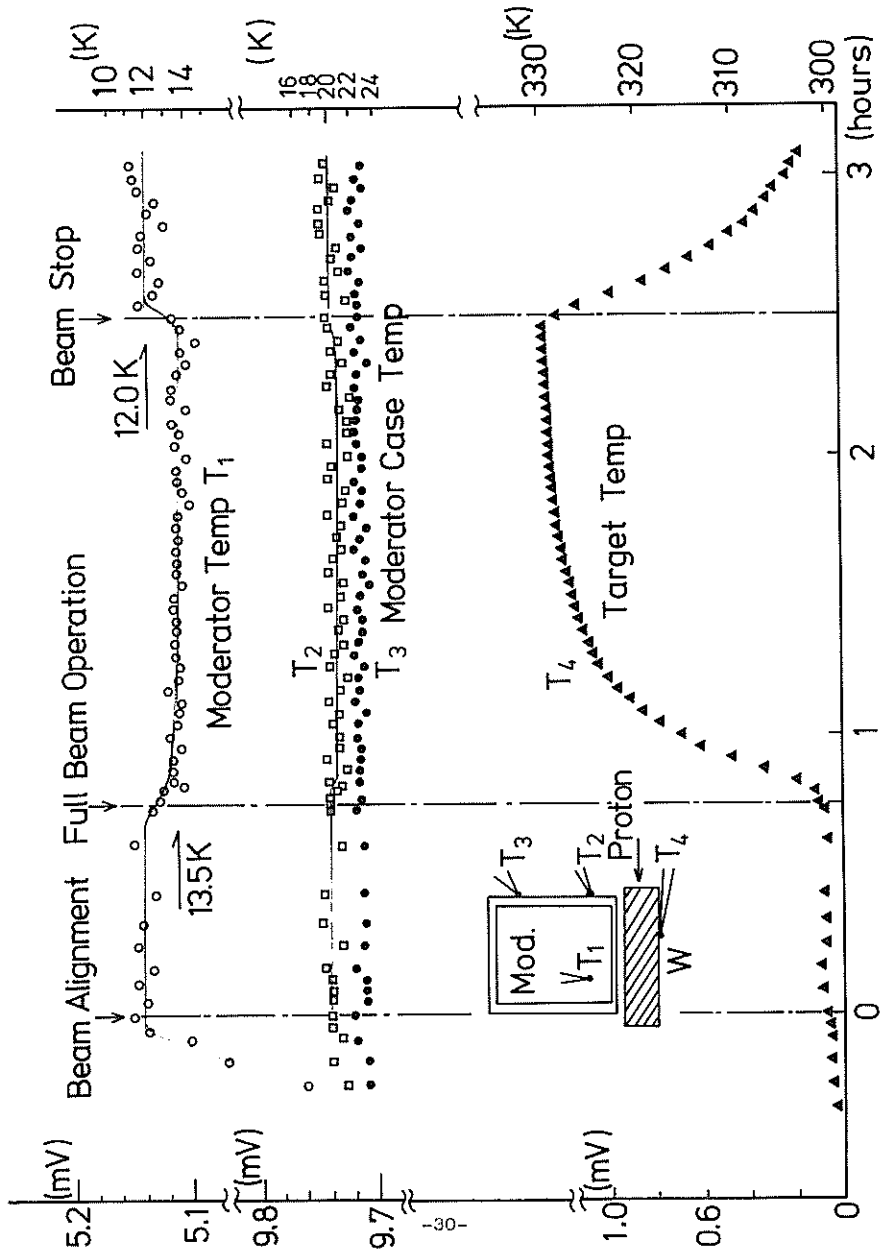

Fig. 2

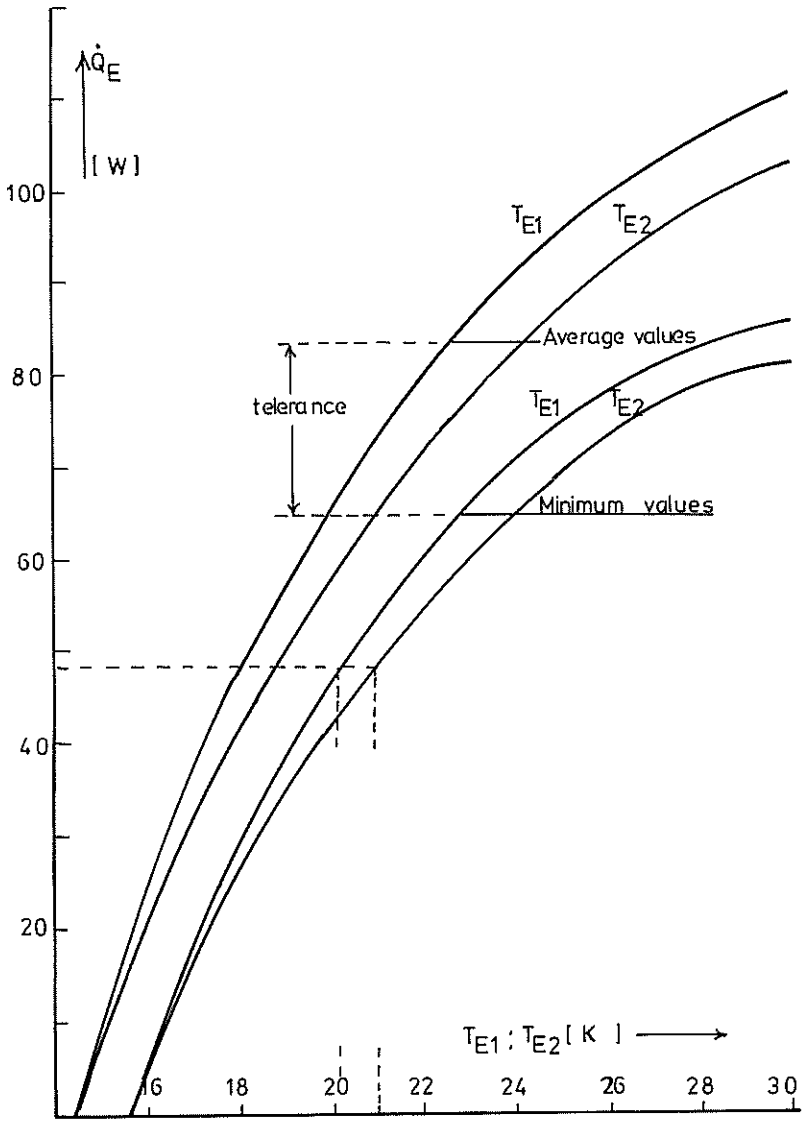
$\dot{Q}_E$
[W]
100
80
60
40
20
T_{E1}
T_{E2}
Average values
tolerance
T_{E1}
T_{E2}
Minimum values
T_{E1} ; T_{E2} [K]
16
18
20
22
24
26
28
30

Fig. 3

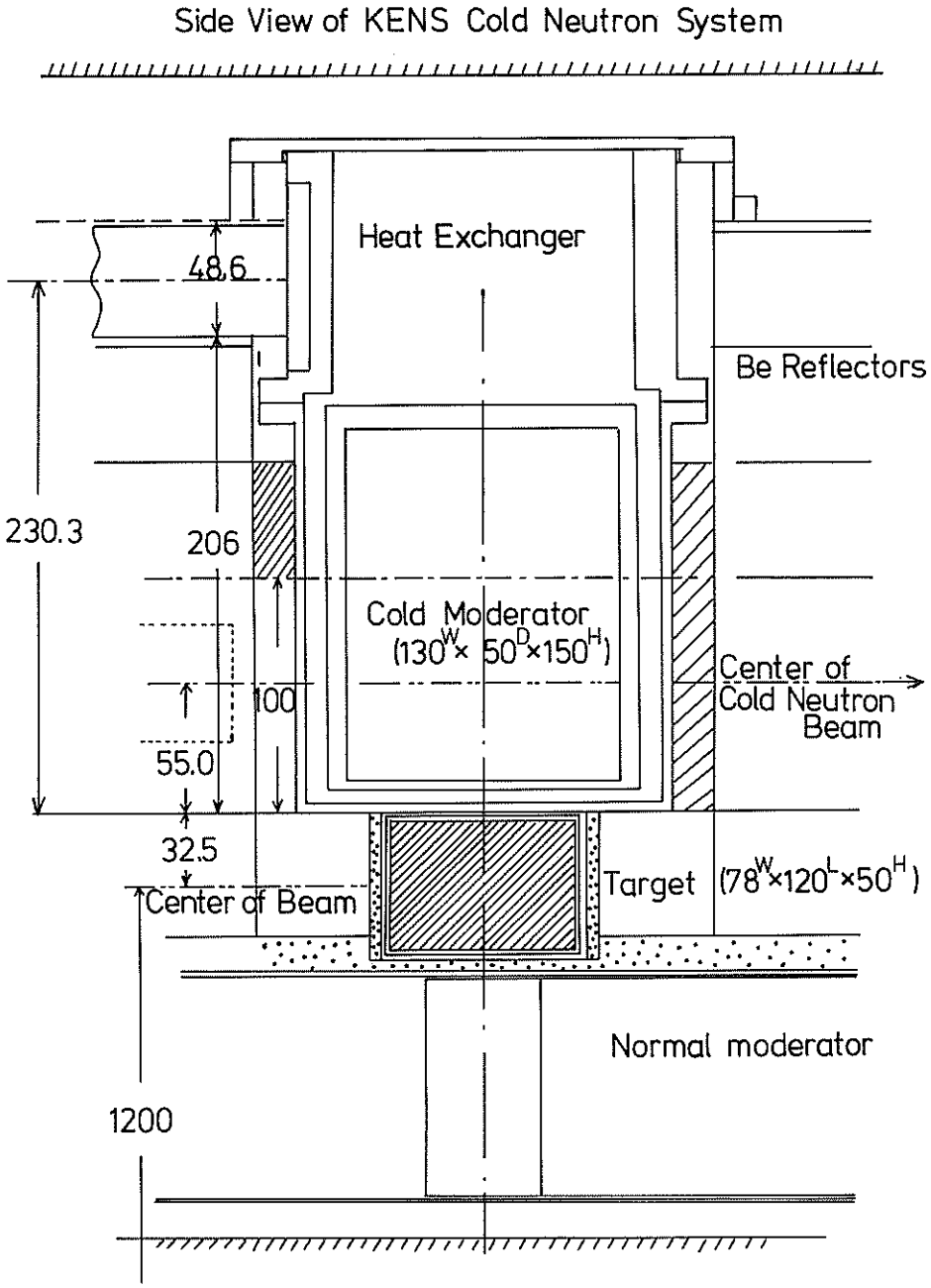
Side View of KENS Cold Neutron System
Heat Exchanger
48.6
Be Reflectors
230.3
206
Cold Moderator
(130W× 50D×150H)
Center of
Cold Neutron
Beam
100
55.0
32.5
Center of Beam
Target (78W×120L×50H)
Normal moderator
1200

Fig. 4

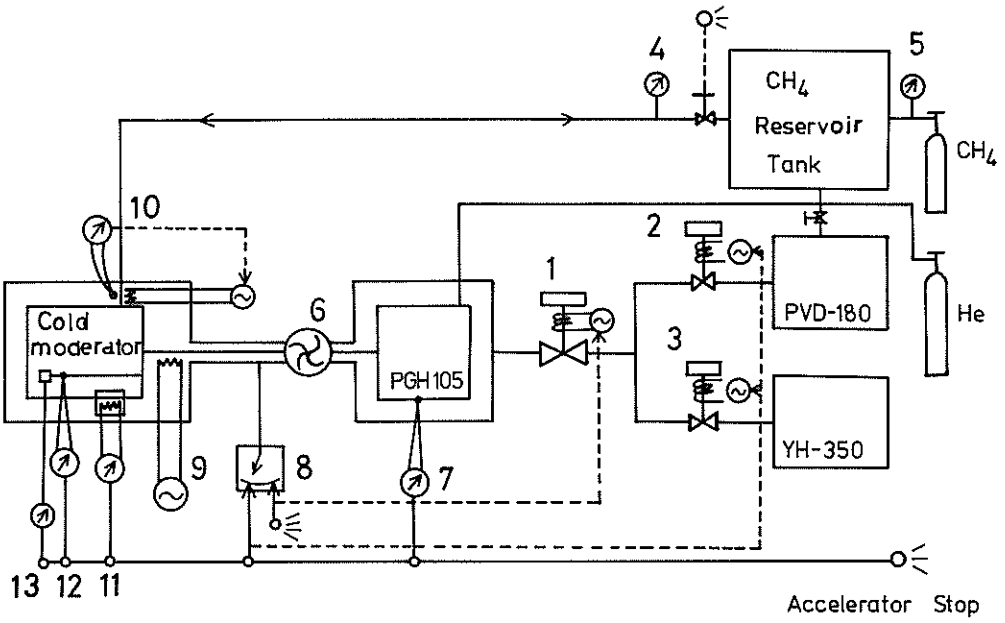
4
5
CH_4
Reservoir
Tank
CH_4
10
2
1
Cold
moderator
6
PGH105
PVD-180
He
3
YH-350
9
8
7
13 12 11
Accelerator Stop

Fig. 5

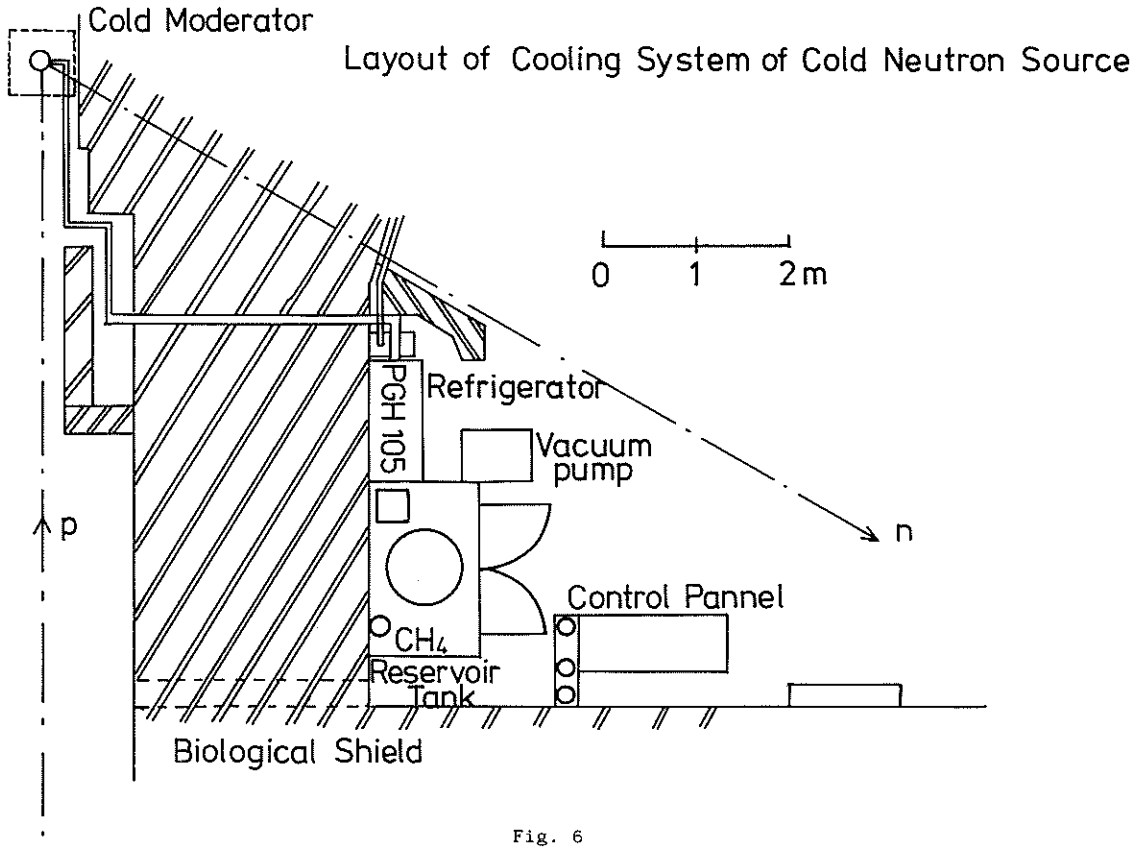
Cold Moderator
Layout of Cooling System of Cold Neutron Source
0 1 2m
PGH 105
Refrigerator
Vacuum
pump
p
n
Control Pannel
CH_4
Reservoir
Tank
Biological Shield

Fig. 6

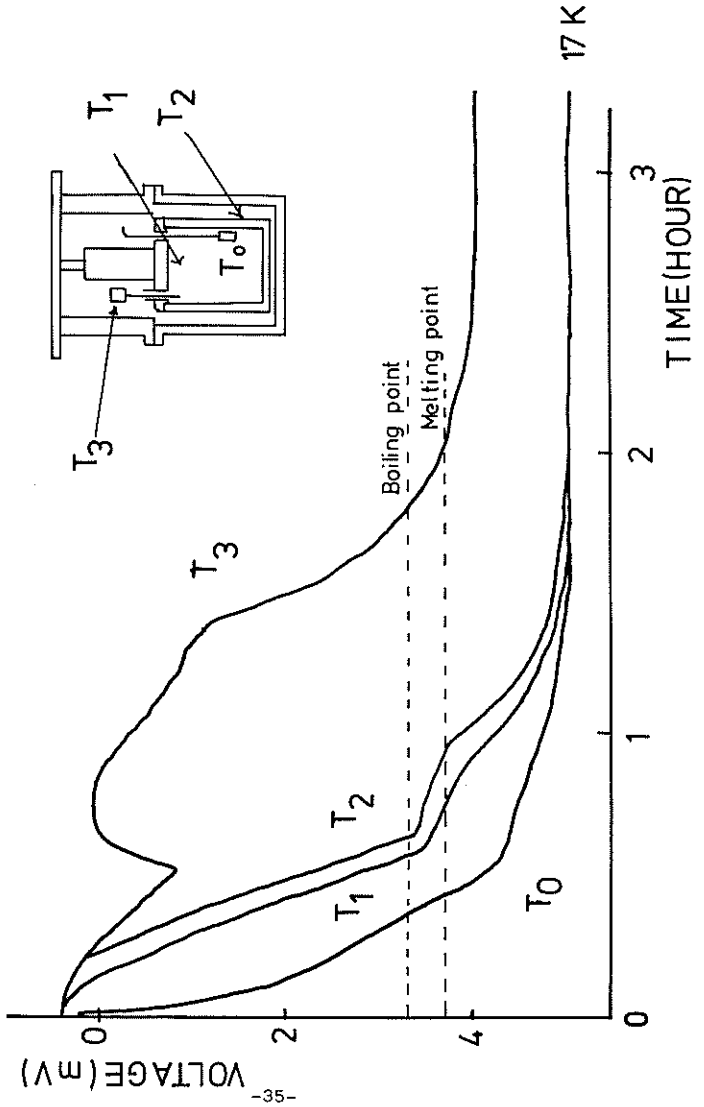

Fig. 7

2.2 On the Neutronic Behavior of the Cold Moderator

Y. Kiyanagi, K. Inoue and H. Iwasa

Department of Nuclear Engineering, Faculty of Engineering,
Hokkaido University, Sapporo

1. Introduction

There have been few systematic works concerning the optimal shape and dimensions of the cold moderator from both the experimental and theoretical points of view. We have been interested in making measurements under conditions similar to an actual case, and, therefor, we have devised several mock-up experiments using an electron linac at Hokkaido University to decide the optimal shape and dimension for the KENS cold neutron source. The neutron flux distribution has been measured for three cold moderator dimensions.

The neutron intensity as well as the emission time have been measured using a thermal moderator with and without a fast neutron reflector.

2. Cold Neutron Flux Distribution

Although solid methane is used for the KENS cold neutron source, we employed solid mesitylene as the cold moderator for

experimental convenience. The moderator characteristics of mesitylene at 20 K are similar to those of methane at 20 K. The moderator was placed 5 cm above the center of the Pb target of 5×5×5 cm^3. The neutron flux distribution was measured as a function of the vertical distance h from the bottom of the chamber. For the precise normalization of intensities in a series of measurements, the dimensions and shapes of the moderator assembly in a cryostat were changed by remote control without interrupting the linac operation. The results taking for three different moderator dimensions are shown in Fig. 1, which indicates that the peak intensity was not so sensitive to the height and width of the moderator when their dimensions exceeded 10 cm. The peak position of spatial distribution was around h=4cm for all cold neutron energies. The integrated neutron intensity emitted from the moderator was proportional to the emission area. The results obtained for mesitylene at 20°K are applicable for methane at 20 K.

3. Fast Neutron Reflector

For the pulsed neutron source both neutron intensity and emission time are important, and with a fast neutron reflector the neutron intensity is increased. Three reflector materials, paraffin, graphite and beryllium oxide, were investigated. An ambient temperature water moderator was placed beside a Pb target; the moderator dimension was 10×10×5 cm^3. The reflector thicknesses were 5 cm for the paraffin and beryllium oxide, and 14 cm for the graphite. A decoupler of Cd sheets was placed between

the moderator and the reflector. Fig. 2 shows the neutron TOF spectra, all of which have the same shapes below the Cd cut-off energy. In this energy region, however, the intensity for the paraffin reflector was 1.5 times higher than that for the bare moderator. In cases using the graphite and beryllium oxide reflector, the multiplication factors were 2 and 3, respectively. It was concluded that beryllium oxide was one of the most efficient reflectors.

To measure the time dependence of neutron pulses, we used mica sheets to diffract the neutron beam into the ^3He counter in the geometry of backscattering at 85° Bragg angle. The measurements were done for three assemblies designated A, B and C. Assembly A was a bare moderator, B contained a beryllium oxide reflector of 5 cm thickness with a Cd decoupler, and C was similar to B but without the Cd decoupler. The moderator was an ambient temperature water and its size was 10×10×5 cm^3. Fig. 3 is an illustration of diffraction patterns. Fig. 4 demonstrates the rise time (Tr), the full width at half maximum (Th) and the decay time (Td). These values were nearly the same in assemblies A and B in the measured energy range, but in assembly C they were longer than those of other assemblies. The rise time of thermal pulses in assemblies A and B was mainly determined by neutron slowing down times in the water moderator, which did not differ very much with each other, and the decay time was mainly determined by absorption and leakage of the neutrons from the moderator. Thus, the time constants for assembly B were almost the same as those for A. In the case of C, the beryllium oxide reflector also worked as a moderator, hence all values of the time constants were elongated.

Finally by using the fast neutron reflector appropriately, we were able to increase the neutron intensity and not affect the neutron emission time.

Figure Captions

Fig. 1 Neutron flux distribution on a mesitylene cold moderator at 20 K for three different moderator dimensions.

Fig. 2 Neutron time-of-flight spectra from a moderator with and without fast neutron reflector.

Fig. 3 A series of diffraction peaks measured for a bare moderator.

Fig. 4 Time constants of neutron pulses for three assemblies.

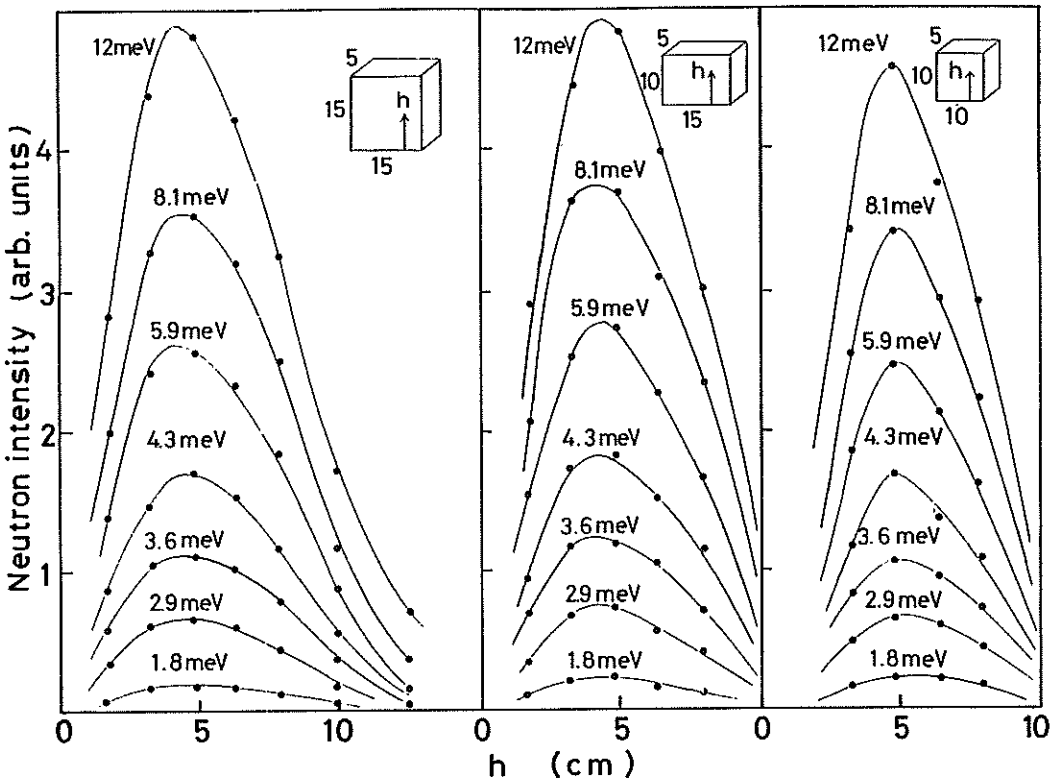
12meV
8.1meV
5.9meV
4.3meV
3.6meV
2.9meV
1.8meV
Neutron intensity (arb. units)
h (cm)
5
15
h
15
10
10

Fig. 1

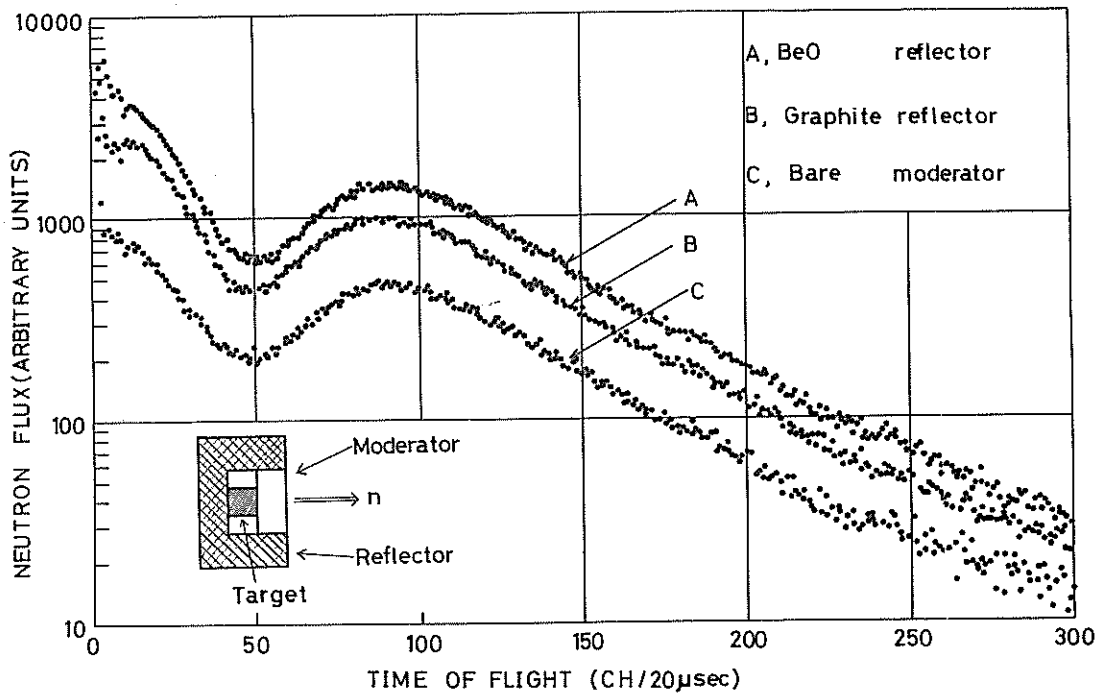
A, BeO reflector
B, Graphite reflector
C, Bare moderator
A
B
C
Moderator
n
Reflector
Target
NEUTRON FLUX(ARBITRARY UNITS)
TIME OF FLIGHT (CH/20μsec)

Fig. 2

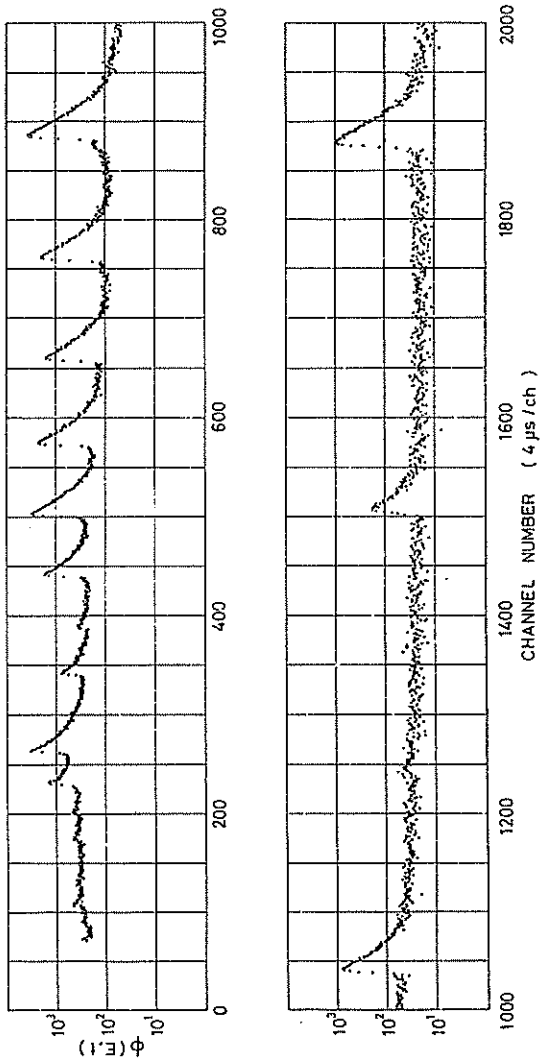
CHANNEL NUMBER (4 μs / ch)
φ(E,t)

Fig. 3

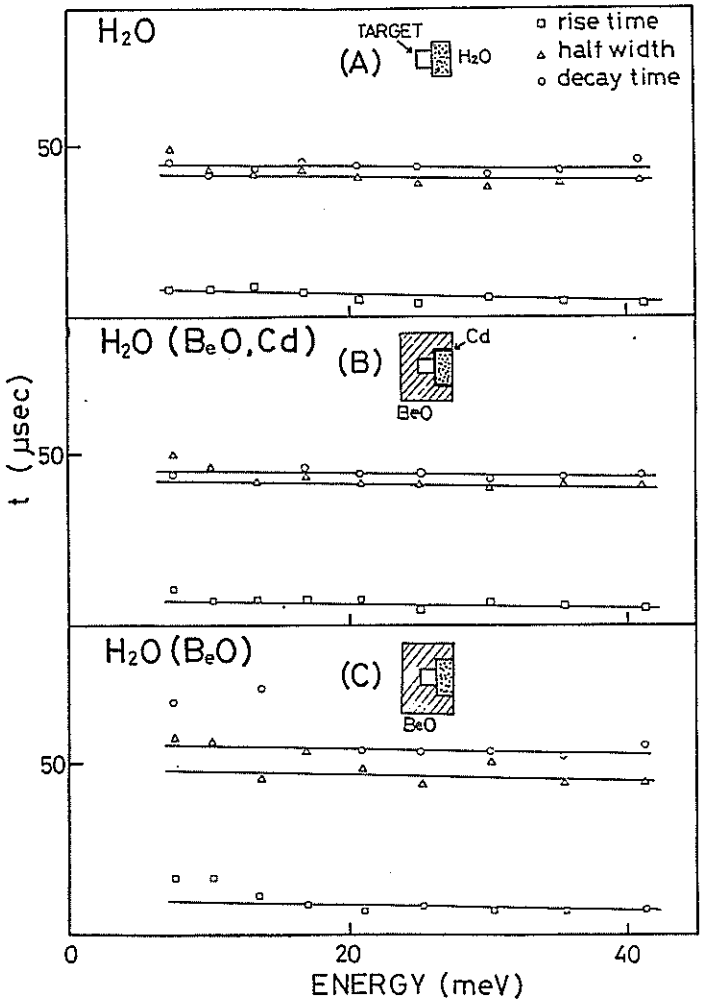
H2O
TARGET
(A)
H2O
rise time
half width
decay time
H2O (BeO,Cd)
(B)
Cd
BeO
H2O (BeO)
(C)
BeO
t (μsec)
50
50
50
0
20
40
ENERGY (meV)

Fig. 4

3. A Design of Neutron Guide Tube

S. Ikeda, Y. Ishikawa* and Y. Endoh*

National Laboratory for High Energy Physics
Tsukuba, Japan

* Tohoku University
Sendai, Japan

§1. Introduction

A cold neutron moderator is installed at the pulsed neutron source at National Laboratory for High Energy Physics (KEK), where high energy spallation neutrons are moderated by solid methane cooled at 20 K.

The peak value of the 4π-equivalent cold neutron flux at the moderator surface is expected to be 10^{16} n/cm^2-sec-eV.[1)]

Cold neutrons are efficiently extracted by three guide tubes from the cold moderator and are transported to a cold neutron experimental area where such spectrometers, as small angle spectrometer, μ-eV spectrometer and polarized cold neutron spectrometer are installed. As shown in Fig.1, each guide tube consists of two parts, a 3.5 m long straight section inbedded inside the biological shield and a curved section with a radius of curvature of 820 m placed outside of it.

Ni coated float glass was used for the neutron reflector. The present report describes the results of the design studies and the final characteristics of the guide tubes calculated by a Monte-Carlo simulation code.

§2. Calculation Method

Firstly we calculate the neutron transportation by one dimensional approximation in the straight section as drawn in Fig.2. Assume that a cold neutron of wavelength λ is emitted from the moderator surface at a position x_M with an angle θ_M. Then the position x_f as well as the angle θ_f of this neutron at the exit is given by following relations.

$$
\begin{aligned}
& x_f = (-1)^N (x'_f - 2Na\ \mathrm{sign}(x'_f)), \\
& \theta_f = (-1)^N \theta_M , \\
& x'_f = x_M + (\ell_0 + \ell_1)\tan\theta_M , \\
& N = \mathrm{Integer}\ ((\mathrm{Integer}(x'_f/a) + 1)/2), \\
& |x_M + \ell_0 \tan\theta_M| \leq a , \\
\text{and} \quad & |\theta_M| \leq \theta_c(\lambda).
\end{aligned}
\tag{1}
$$

Here $\theta_c(\lambda)$ is a critical angle for λ. Next we discuss the neutron trajectory in the bent section. If a neutron at an entrance with a cordinate (x_1, θ_1) moves to (x'_1, θ'_1) at an exit (See Fig. 3), the relation between (x'_1, θ'_1) and (x_1, θ_1) are expressed as follows

$$
\begin{aligned}
& x'_1 \cos\theta'_1 = x_1 \cos\theta_1 , \\
\text{and} \quad & \theta'_1 = \omega + \theta_1 .
\end{aligned}
\tag{2}
$$

By using these relations, a final position at the exit of the guide (x_2, θ_2) is given as follows (See Fig.4)

$$
\begin{aligned}
& \theta_2 = \theta_r + \Delta\theta_2 , \\
\text{and} \quad & x_2 = x_1 \cos\theta_1 / \cos\theta_2 .
\end{aligned}
\tag{3}
$$

If the neutrons are transported without reflection, θ_r and $\Delta\theta_2$ are expressed as

$$\theta_r = \theta_1 ,$$
$$\Delta\theta_2 = \theta_{max} . \tag{4}$$

If the neutrons are reflected by the wall of the guide, θ_r and $\Delta\theta_2$ are given as follows (See Fig.5).

$$\theta_r = \frac{1}{2}(\theta_b - \theta_a - (\theta_a + \theta_b)f) ,$$

$$\Delta\theta_2 = \mathrm{Mod}\ ((\theta_{max} - \Delta\theta_1)/\Delta\theta) ,$$

$$f = \begin{cases} \mathrm{sign}(\theta_1 - \theta_t)\cdot(-1)^{N-1} & (\theta_a \geq \theta_p) , \\ 1 & (\theta_a < \theta_p) , \end{cases}$$

$$N = \mathrm{Integer}\ (\theta_{max} - \Delta\theta_1/\Delta\theta) + 1 ,$$

$$\theta_a = \left|\cos^{-1}\ (\frac{1}{\ell+2d}\cos\theta_1)\right| ,$$

$$\theta_b = \left|\cos^{-1}\ (\frac{\ell_1}{\ell}\cos\theta_1)\right| ,$$

$$\theta_p = \left|\cos^{-1}\ \frac{\ell}{\ell+2d}\right| ,$$

$$\Delta\theta = \begin{cases} 2\theta_a & (\theta_a \leq \theta_p) , \\ \theta_a - \theta_b & (\theta_a > \theta_p) , \end{cases}$$

$$\Delta\theta_1 = \begin{cases} \theta_a - \theta_1 & (\theta_1 \geq \theta_t) , \\ |\theta_b - |\theta_1|| & (\theta_1 < \theta_t) , \end{cases}$$

$$\theta_t = \begin{cases} -\cos^{-1}(\ell/x_1) & (|\theta_t| \leq \theta_{max}) , \\ -\cos^{-1}(\frac{\ell}{Q}\sin\theta_{max}) & (|\theta_t| > \theta_{max}) , \end{cases}$$

and $$Q = (x_1^2 + \ell^2 - 2\ell x_1\cos\theta_{max})^{1/2} . \tag{5}$$

Finally we discuss the case of a polygonal guide tube made of combination of the short straight sections with the length ℓ_2 and the width 2d (See Fig.6).

Since the transportation of the neutrons in the short straight section is calculated by Eq.(1), it is enough to calculate the transportation between two sections (see Fig.8), which is expressed as following relations.

$$X'\cos\delta = p\sin\theta_2 + X ,$$
$$X'\sin\delta = p\cos\theta_2 , \tag{6}$$
$$\theta_1 = \theta_2 + \delta ,$$
and $$\delta = \ell_2/\ell .$$

By using these relations, numbers of neutrons with λ and θ coming out from the exit of the guide tube can be calculated by the Monte-Carlo simulation technique.

§3. Requirements of KENS guide tube and determination of parameters

The parameters of the neutron guide tubes at KENS should be determined so as to satisfy following requirement.

1. The cold moderator has an effective area of $12^W \times 15^H$ cm^2.
2. The distance ℓ_0 between the moderator and the entrance of the straight section must be greater than 150 cm, mainly because of the requirement of the geometry of the bilogical shield.

3. The distance between the cold moderator and the end of the straight section ($\ell_1 + \ell_0$) is fixed to be 5 m corresponding to the thickenss of the biological shield (Fig.8(A)). The height D of the straight section with respect to the moderator (Fig.8(A)) is an important parameter to be determined.
4. The bent section is put at a distance E from the straight section with an inclination angle ε as seen in Fig.8(B). E was fixed to be 30 cm, which is the minimum distance required to install a tail cutter, while ε should be determined to get the optimal characteristics.
5. The width of the guide in the bent section 2d was fixed to be 2 cm, in order to make the distance of the direct view less than 11 m. The width of the straight section 2a should be determined by present calculation.
6. The curvature of the bent tube was automatically determined to be 820 m from the cut off wave length λ_c = 4 Å and 2d.
7. The length ℓ_2 of the straight section composing the polygonal guide tube (cf. Fig.8(B)) should be chosen either 0.9 m or 1 m.

Thus a Monte-Carlo simulation calculation was practiced in order to determine the optimal values for 2a, D, ℓ_0, ε and ℓ_2. The calculation was first performed only for a combination of the moderator and the straight section in order to determine 2a, D and ℓ_0. Then additional calculation was made in order to determine ε and ℓ_2 in the bent sections. The results of calculations are displayed in successive figures.

i) Determination of 2a, ℓ_0 and D

The dependence of the total intensity, $I_{\ell}(\lambda)$, of neutrons at the exit of the straight section on ℓ_0 was calculated by one dimensional model. Fig.9 illustrates the case where the flux distribution along the horizontal line

on the moderator is uniform, while the result for the non uniform distribution (cosine distribution) is displayed in Fig.10. In the former case, the intensity starts to decrease for ℓ_0 longer than (A-a)/θ_c, while in the second case, the corresponding value is (2/3 A-a)/$\theta_0(\lambda)$. These values are calculated for different wave lengths and are listed in Table 1. A similar one dimensional calculation was also carried out for the vertical direction by using the flux distribution experimentally obtained[2] (see Fig.11). These three figures as well as the table indicate that ℓ_0 is nearly optimal at ℓ_0 = 150 cm for the wavelength shorter than 9 Å, but it is not the case for the longer wave length. In Fig.12 is shown the D dependence of the intensity. The results suggest that the most favorable value of D is 4.7 cm independent on the wave length. The calculation was also practiced by varying 2a and it was found that the density of neutrons at the central region of the cross section of the guide tube increases only by 2 % for 2a = 2 cm compared with the case for 2a = 3 cm. Therefore we adopted 2a = 3 cm, for making setting easy.

ii) Determination of ℓ_2 and ε

Total intensity of cold neutrons at the exit of the bent guide tube I(E) was calculated as a function of ε. Note that the neutrons from the cold moderator are assumed to have the energy spectrum of the Maxwellian distribution at 20 K. The results of calculation are displayed in Fig.13. It indicates that, by choosing ε = 15', the cut off wave length is shifted to the shorter wave length side, but that the total intensity is reduced almost by 20 %, compared with the case for ε = 0. Therefore we appreciate the intensity increase and decided to adopt ε = 0. The transmittance of the polygonal guide tube $I_\lambda(18)/p(\lambda)\ _c(\lambda)$ was calculated as a function of λ for two cases of ℓ_2 = 0.9 m and 1 m. The results are illustrated in Fig.14, where $I_\lambda(18)$ and $p(\lambda)$ are the intensity of neutrons at the

exit of the guide tubes with a total length of 18 m and the intensity of neutrons with λ on the source surface respectively. The figure indicates that the transmittance shows almost no difference between these two cases and, therefore, ℓ_2 was determined to be 1 m inorder to reduce the manufacturing cost as well as the loss of neutrons due to the inaccuracy of the setting.

§4. Characteristic of the KENS guide tube

Thus five parameters a, ℓ_0, D, ε and ℓ_2 were finally determined to be a = 1.5 cm, ℓ_0 = 150 cm, D = 4.7 cm, ε = 0 and ℓ_2 = 100 cm. Finally the characteristics of the guide tube calculated using these parameters. The spacial variations of the intensity of neutrons at different cross sections α, β, γ and δ are shown in Fig.15-a, b and c for three different neutron energies. It is noted that the beam profile becomes in homogeneous for the energy higher than the cut off energy (E = 5 meV), but the inhomogeneity disappears for E = 0.5 meV (λ = 12.7 Å). It does not depend upon the position in the bent tube.

The wave length dependence of the intensity of neutrons at the exit of the polygonal guide tube of 18 m long was finally calculated by integrating all the neutrons arrived at the exit and the result is shown in Fig.16. The cold neutron source was assumed to have an energy spectrum of the Maxwellian at 20 K as mentioned previously. The energy spectrum at the exit is found to be well described by a function $1/\lambda^4 \cdot e^{-(\lambda_t/\lambda)^2}$ with λ_T = 7.6 Å. This relation was employed to estimate the intensity of small angle scattering as described in §4. 3.

Reference

1) Y. Ishikawa and N. Watanabe: KEK Report 78-19.

2) Y. Kiyanagi, K. Inoue and H. Iwasa: §2.2 of this report.

Figure Captions

Fig.1 Cold neutron experimental area in KENS.

Fig.2 Neutron trajectory in a straight guide tube.

Fig.3 Cordinates (x_1, θ_1) of neutron beam in a bent guide tube.

Fig.4 Final cordinate (x_2, θ_2) at the exit of a bent guide tube.

Fig.5 Neutron trajectory in a bent guide tube.

Fig.6 Polygonal guide tube.

Fig.7 Propagation of a cold neutron in a connecting part.

Fig.8 System of neutron guide tubes in KENS.
(A) part; a straight tube section.
(B) part; a bent tube section.

Fig.9 Variation of neutron intensity at the exit of a straight guide tube with respect to distance between source and guide tube ℓ_0 for a uniform neutron source.

Fig.10 Distance ℓ_0 dependence of neutron intensity at an exit of a straight guide tube for a non uniform neutron source.

Fig.11 Distance ℓ_0 dependence of neutron intensity at the exit of a straight guide tube for a source with spacial distribution of intensity experimentally determined.

Fig.12 Variation of neutron intensity at the exit of a straight guide tube with respect to the height of the guide tube D.

Fig.13 Inclination angle ε dependence of intensity of neutrons at the exit of a bent guide plotted against the wave length.

Fig.14 Transmittance of a polygonal neutron guide tube plotted against wave length λ.

Fig.15 The neutron beam profile at the cross sections α, β, γ and δ of the different positions in a bent guide tube. Results are shown in cases of neutrons with E = 1 meV(a), 4 meV(b), and 0.5 meV(c).

Fig.16 Wave length dependence of neutron intensity at the exit of a 18 m long polygonal guide tube.

Table 1

λ(Å)	4	6	8	12
$\frac{A-a}{\theta_c(\lambda)}$	652 cm	435 cm	326 cm	218 cm
$\frac{(2/3 \cdot A-a)}{\theta_c(\lambda)}$	362 cm	242 cm	181 cm	121 cm

Values of $(A-a)/\theta_c$ and $(2/3 \cdot A-a)/\theta_c$
(A = 6.0 cm, a = 1.5 cm)

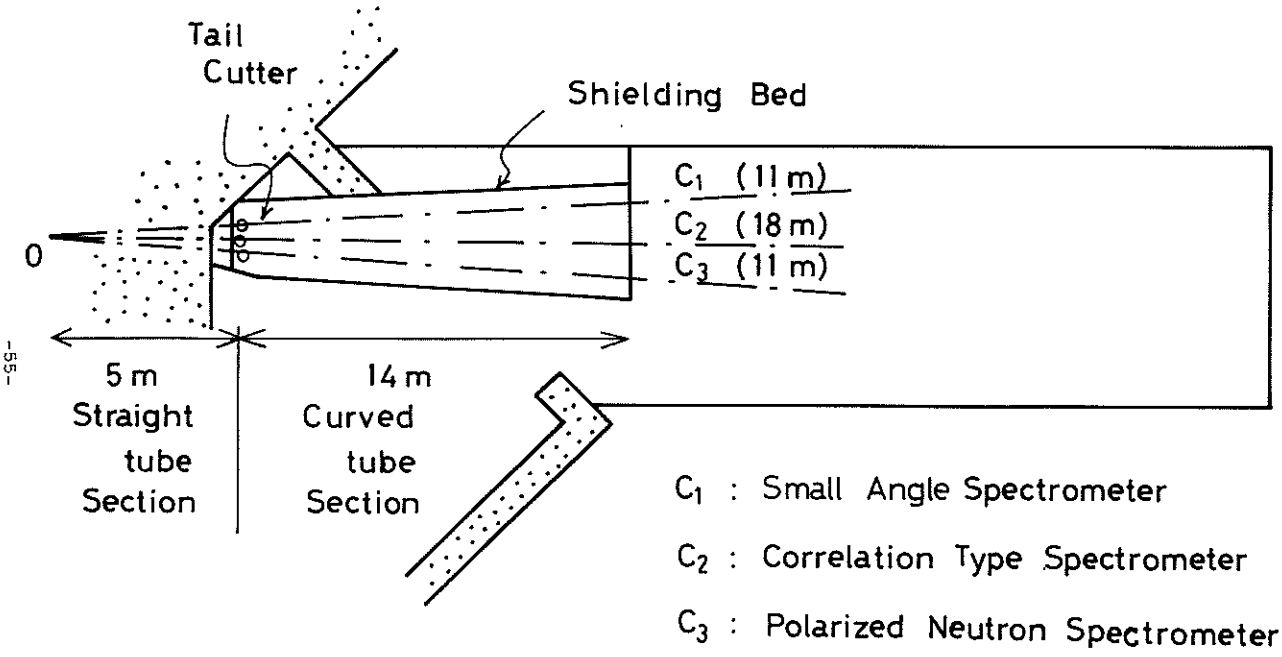
Tail
Cutter
Shielding Bed
C1 (11 m)
C2 (18 m)
C3 (11 m)
0
5 m
Straight
tube
Section
14 m
Curved
tube
Section
C1 : Small Angle Spectrometer
C2 : Correlation Type Spectrometer
C3 : Polarized Neutron Spectrometer

Fig. 1

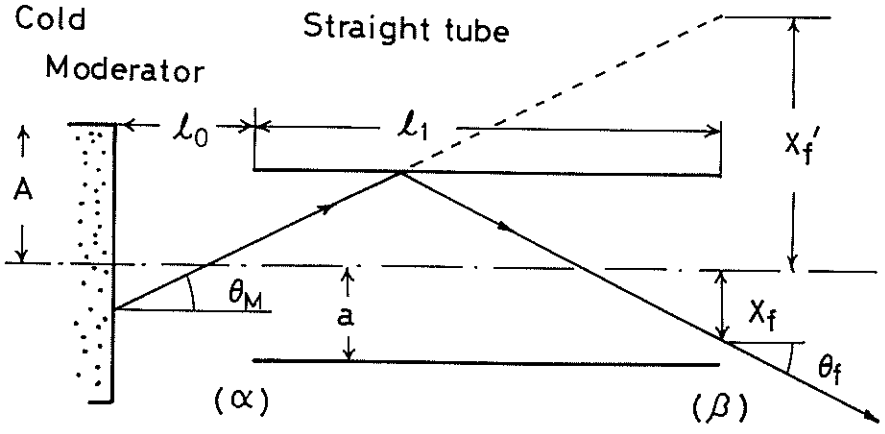
Cold
Moderator
Straight tube
ℓ_0
ℓ_1
X_f'
A
θ_M
a
X_f
θ_f
(α)
(β)

Fig. 2

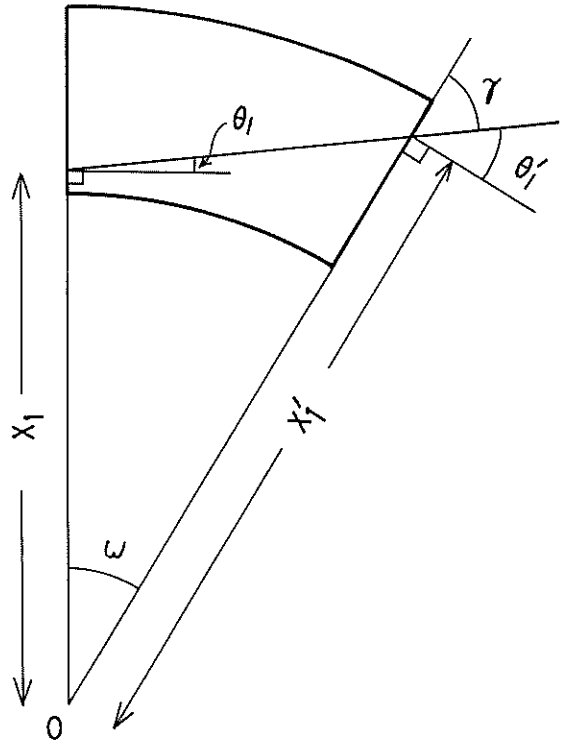

Fig. 3

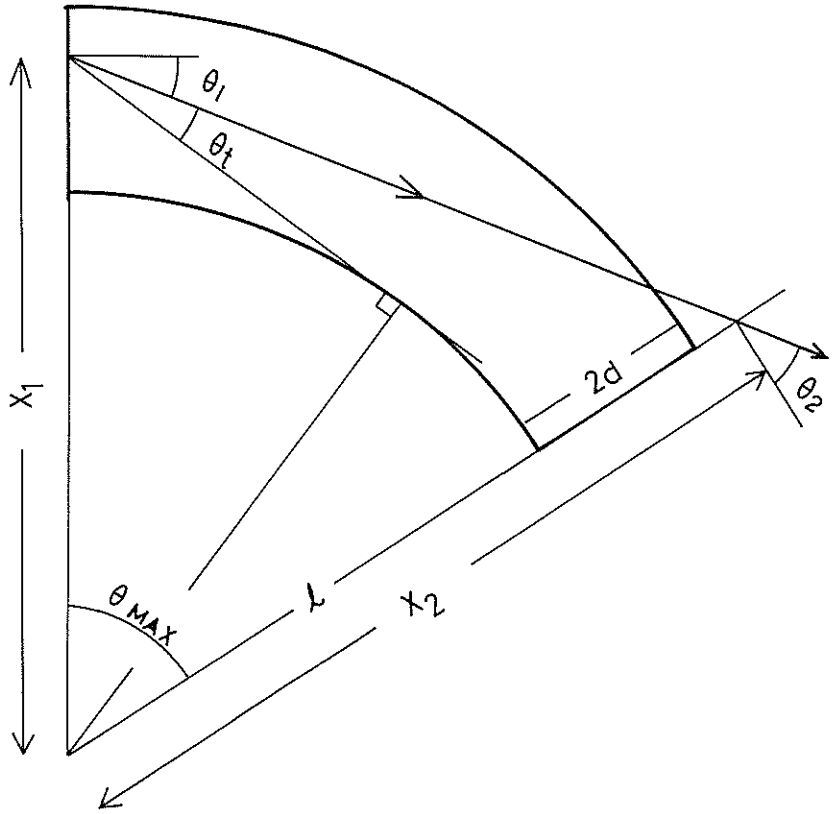

Fig. 4

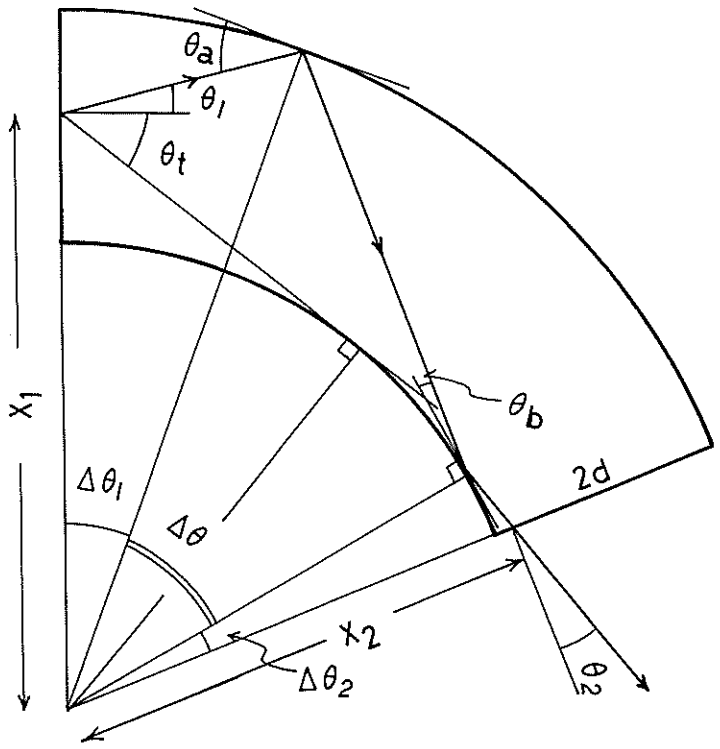
θ_a
θ_1
θ_t
θ_b
x_1
$\Delta\theta_1$
$\Delta\theta$
2d
x_2
$\Delta\theta_2$
θ_2

Fig. 5

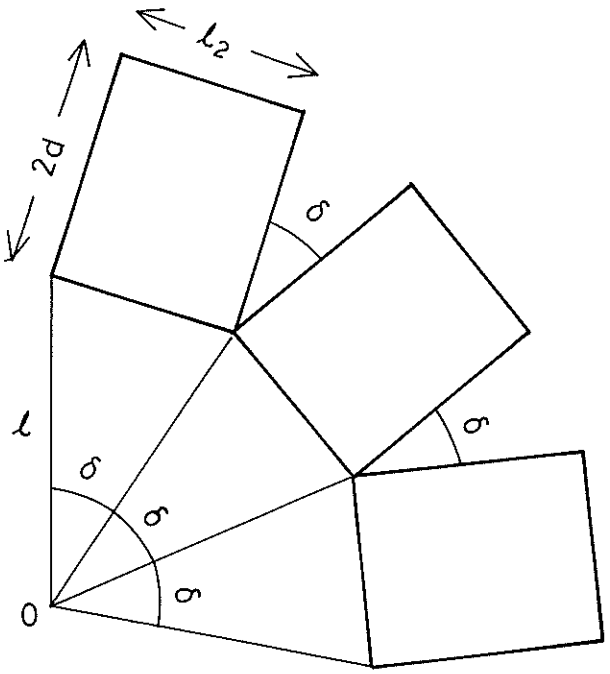
l_2
2d
δ
δ
l
δ
δ
δ
0

Fig. 6

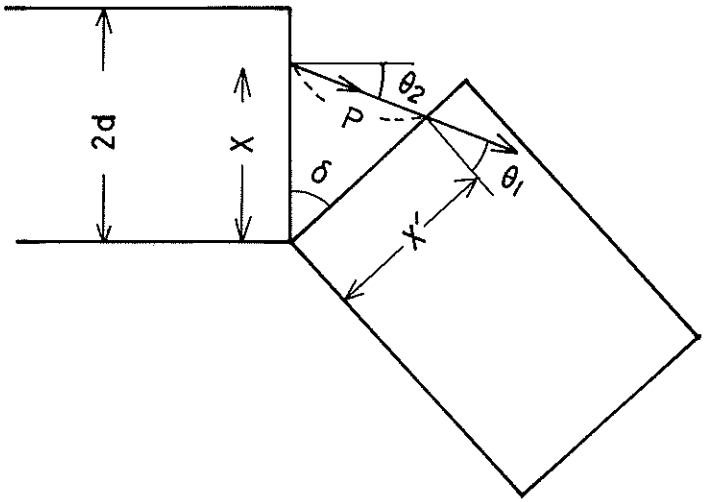
2d
X
P
θ2
δ
θ1
X'

Fig. 7

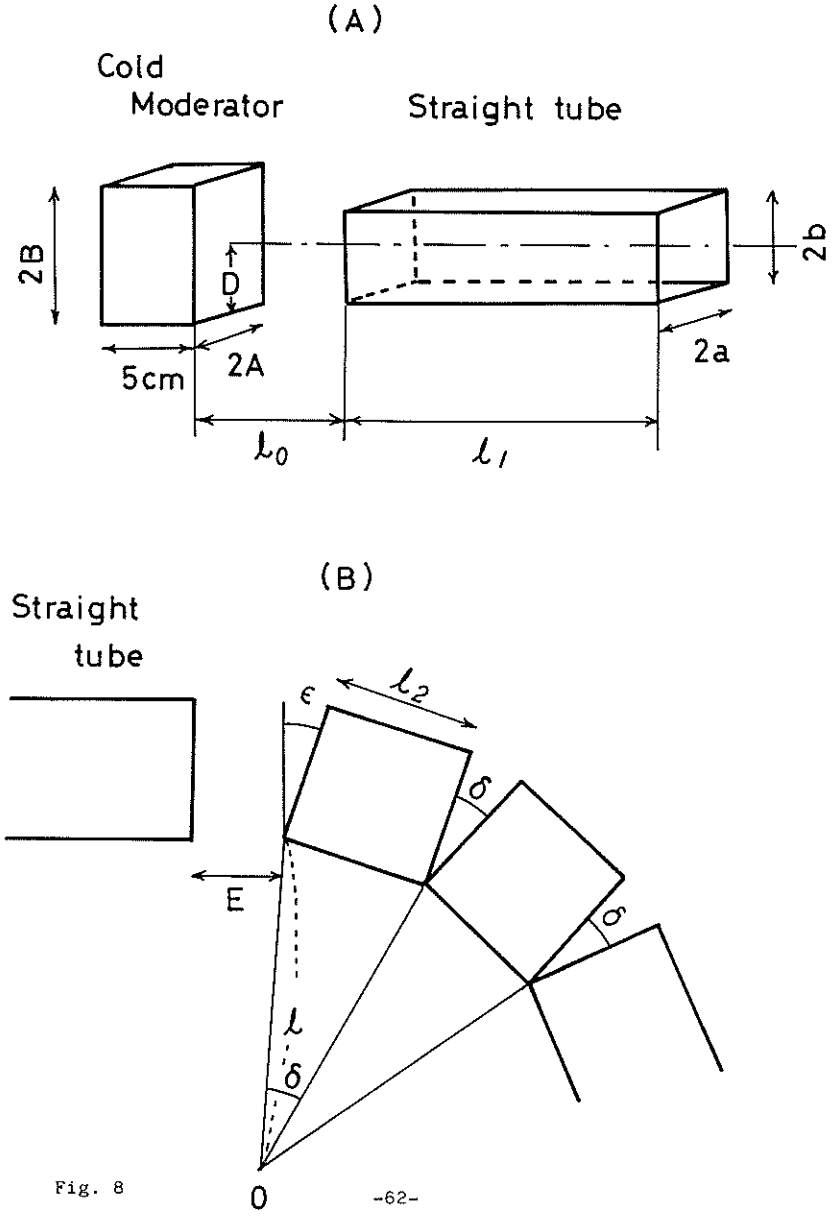
(A)
Cold
Moderator
Straight tube
2B
D
2b
5cm
2A
2a
l_0
l_1
(B)
Straight
tube
ε
l_2
δ
δ
E
l
δ
0

Fig. 8

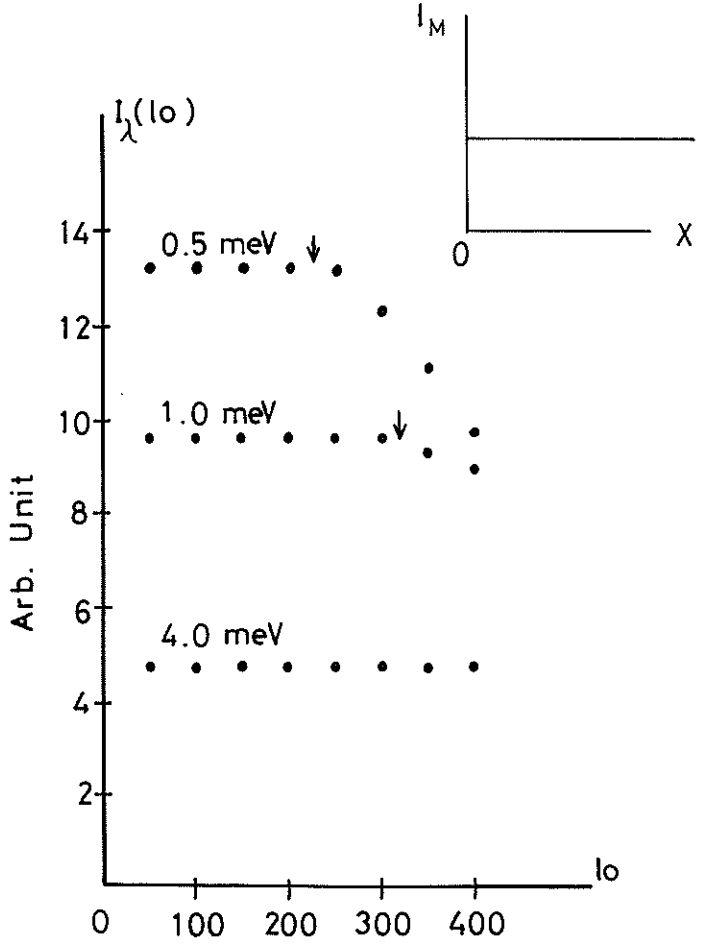
I_M
$I_\lambda(lo)$
0
X
14
12
10
8
6
4
2
0.5 meV
1.0 meV
4.0 meV
Arb. Unit
0
100
200
300
400
lo

Fig. 9

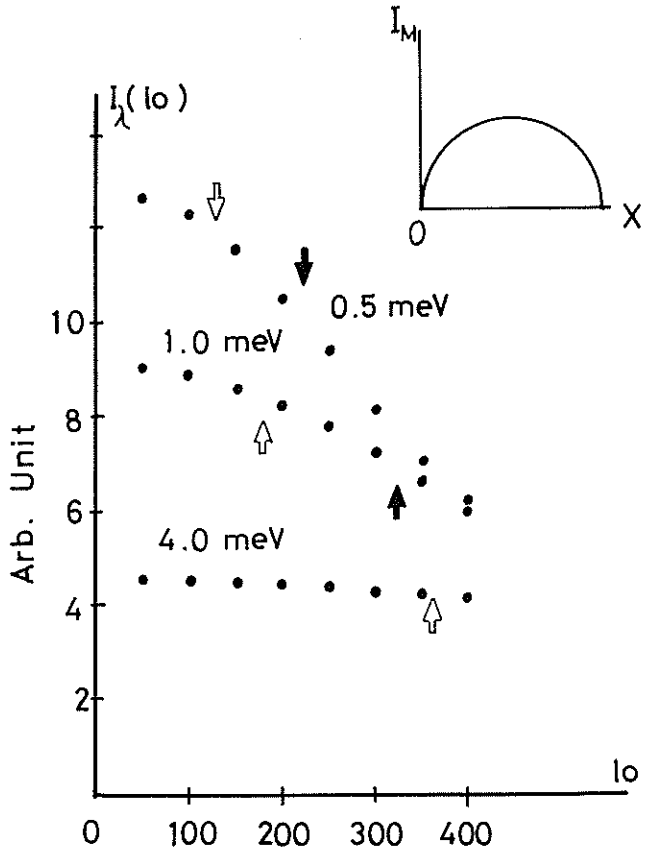
I_M
$I_\lambda(lo)$
0
X
10
8
6
4
2
0.5 meV
1.0 meV
4.0 meV
Arb. Unit
0
100
200
300
400
lo

Fig. 10

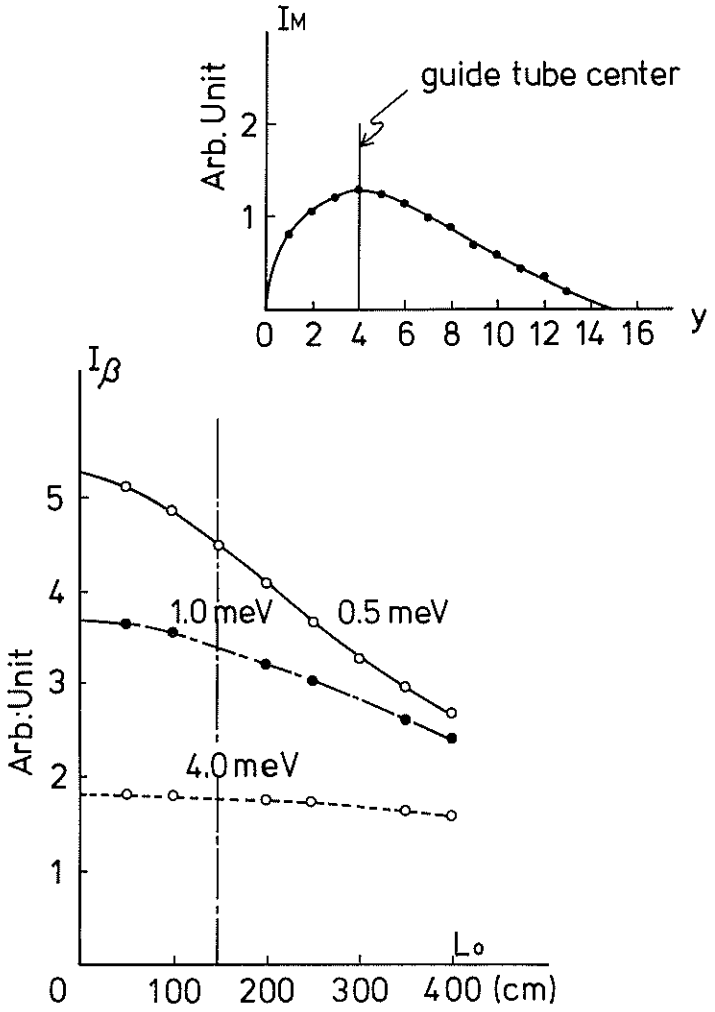
IM
guide tube center
Arb. Unit
2
1
0 2 4 6 8 10 12 14 16
y
Iβ
5
4
3
2
1
Arb:Unit
1.0 meV
0.5 meV
4.0 meV
Lo
0 100 200 300 400 (cm)

Fig. 11

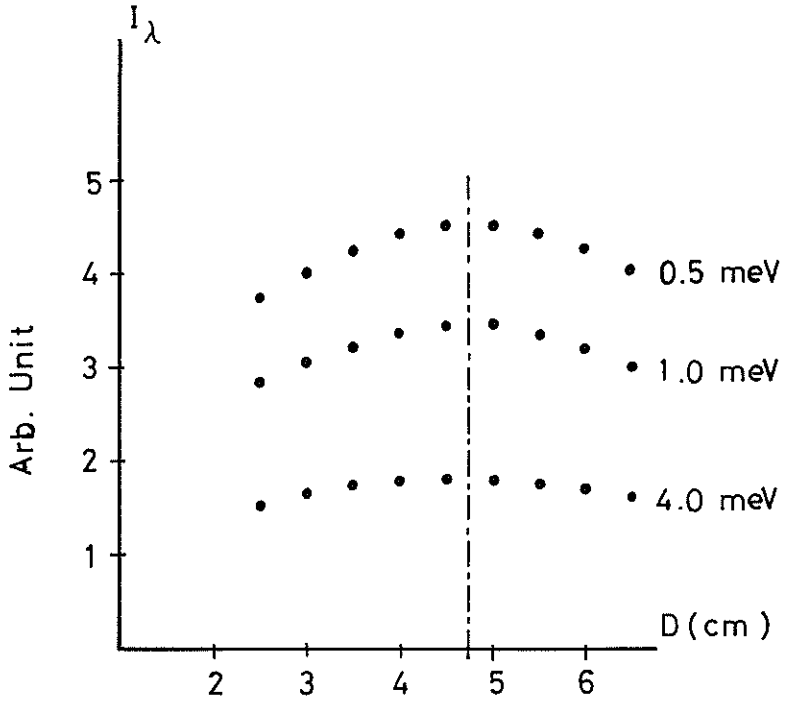
Iλ
5
4
3
2
1
Arb. Unit
0.5 meV
1.0 meV
4.0 meV
D (cm)
2 3 4 5 6

Fig. 12

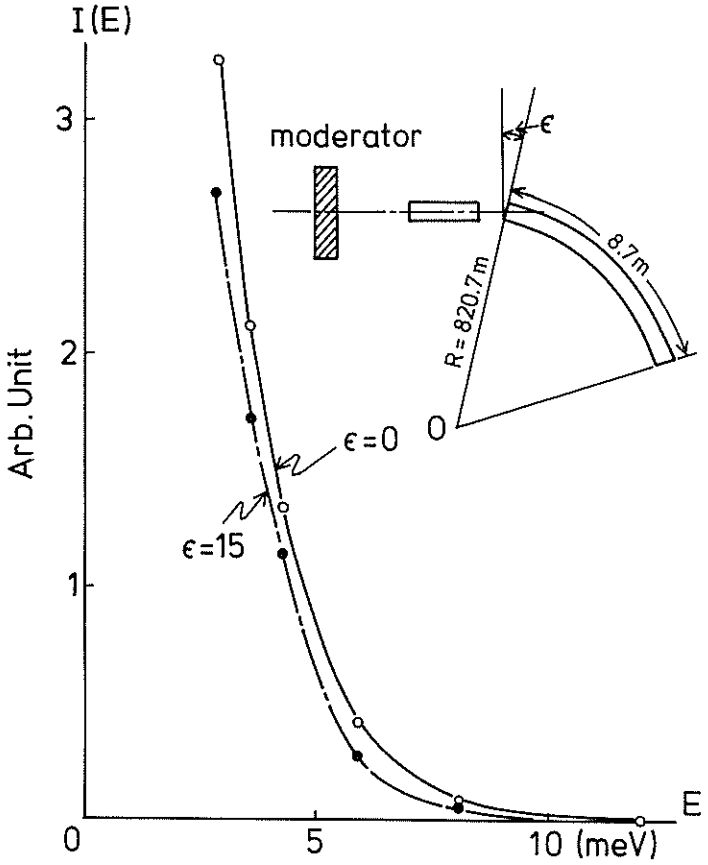
I(E)
Arb. Unit
3
2
1
0
5
10 (meV)
E
moderator
ϵ
8.7m
R = 820.7m
0
ϵ=0
ϵ=15

Fig. 13

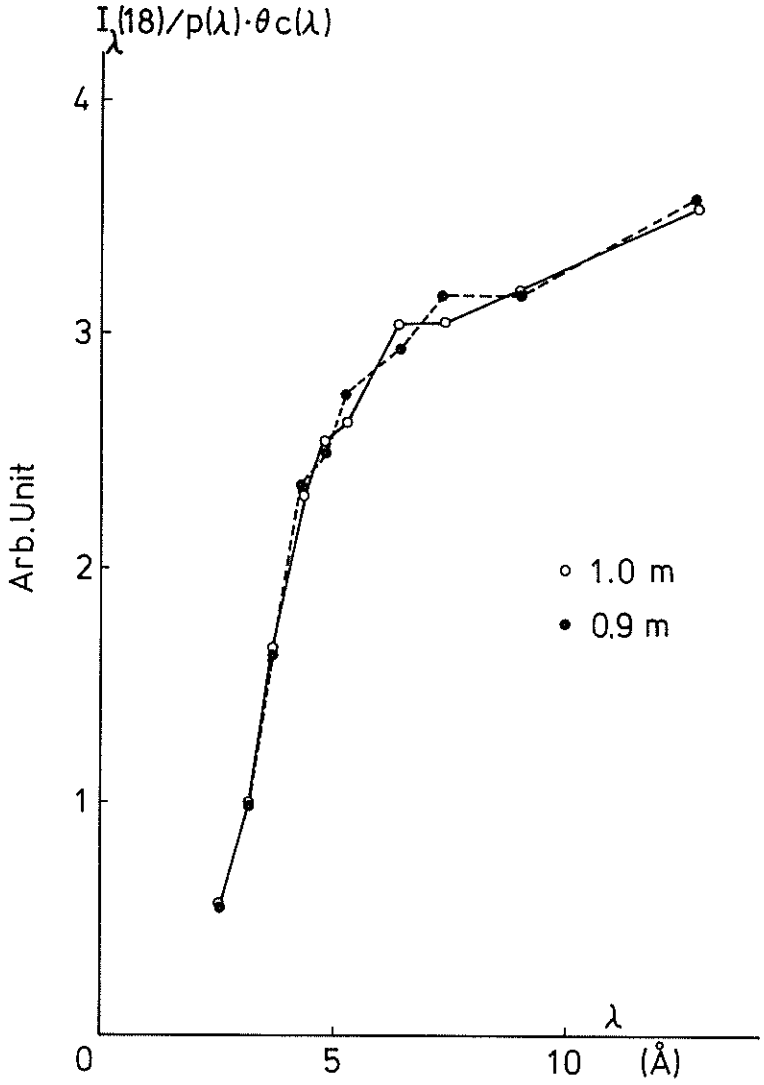
I_λ(18)/p(λ)·θc(λ)
Arb. Unit
4
3
2
1
0
5
10
(Å)
λ
λ
○ 1.0 m
● 0.9 m

Fig. 14

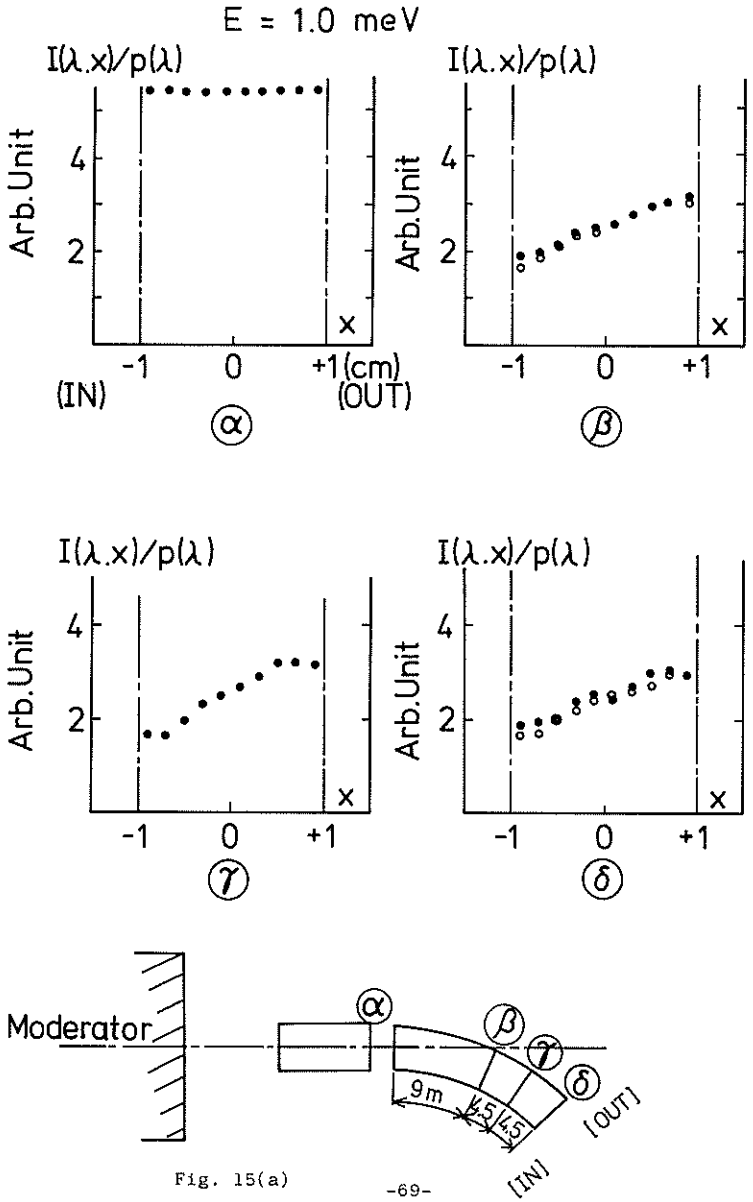

Fig. 15(a)

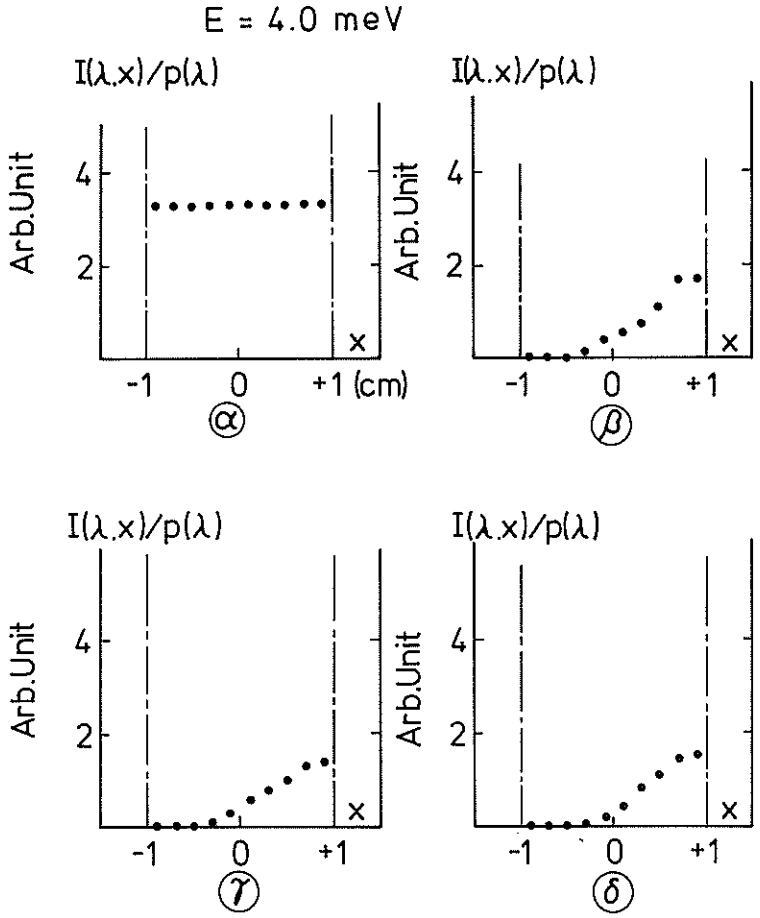

Fig. 15(b)

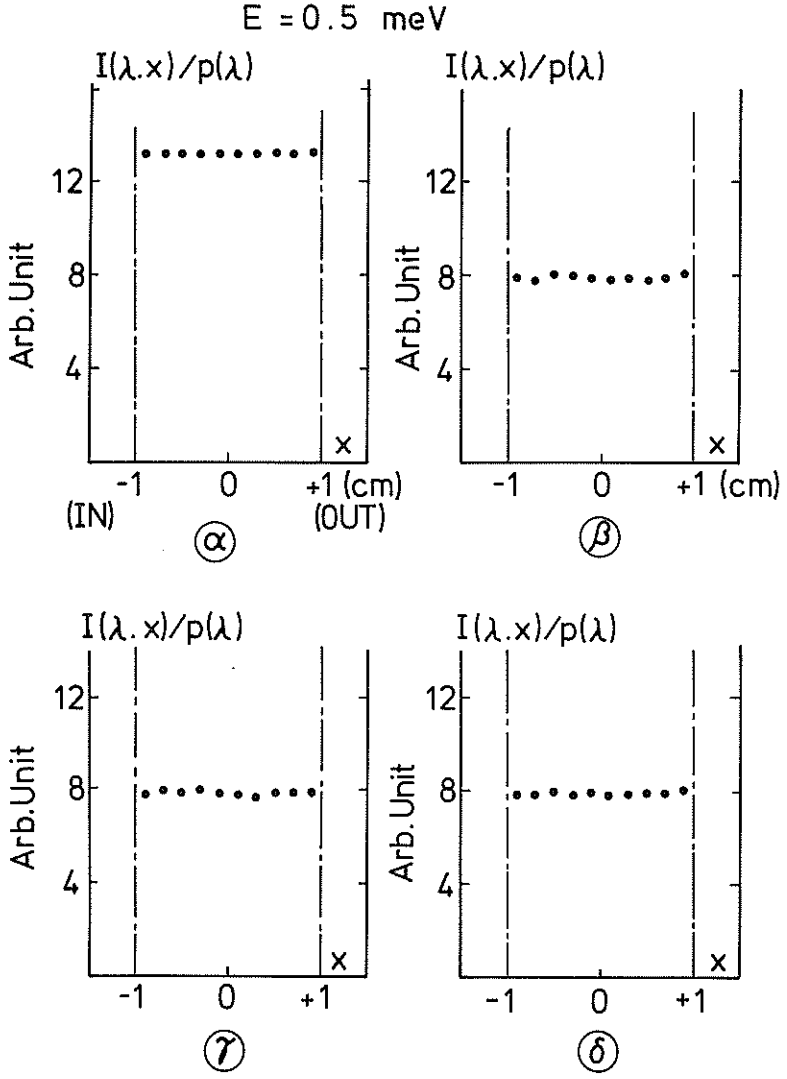

Fig. 15(c)

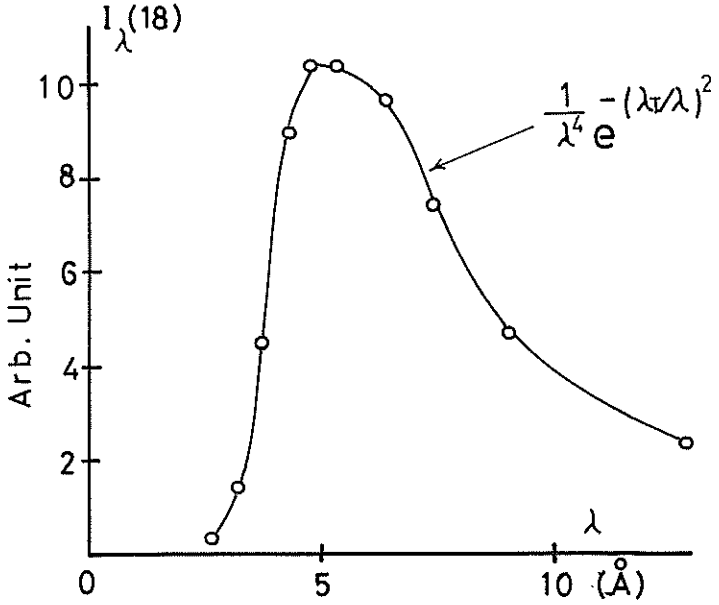

Fig. 16

4. Spectrometers

4.1 High Intensity Total Scattering Spectrometer (HIT)

Noboru Watanabe†, Kazuyoshi Yamada*, Masakatsu Misawa**
Laboratory of Nuclear Science, Physics Department*
Research Institute for Iron, Steel and Other Metals**
Tohoku University, Sendai, Japan

and

Tadashi Mizoguchi
Physics Department, Faculty of Science, Gakushuin University,
Tokyo 171 Japan

Abstract

This instrument is a total scattering spectrometer for KEK pulsed neutron source designed to measure the structure factor S(Q) of liquids and amorphous solids as a function of Q from 0.5 to about 100 A^{-1} at higher rate of data collection.

Scientific applications of the spectrometer are as follows.

(i) Structural studies in non-equilibrium states: measurements of time-dependent structure factor S(Q,t) as a function of time t from several tens of μ sec to hours after a quick change of the sample conditions. (Solidification of liquids, crystalization of amorphous solids, anisotropic response of the atomic arrangements in polymers to the external uniaxial force etc. will be studied.)

Presented at ICANS Meeting, Rutherford Lab., 10-12 Sept. (1979)
† Present address: National Laboratory for High Energy Physics
Oho-machi, Tsukuba-gun, Ibaraki

(ii) Studies on the short range order in liquids and amorphous solids, especially precise determination of the partial structure factors of two-or multi-component systems with the isotope substitution method.

(iii) Studies on magnetic structure of the ferromagnetic or antiferromagnetic amorphous solids.

(iv) Structural studies on a small sample of strong neutron absorbing materials.

(v) (Structural studies under extreme conditions.)

Outline of the Spectrometer

Figures 1 and 2 show the spectrometer which is scheduled to be installed at H3 beam hole, viewing a polyethylene moderator at room temperature, of the KEK pulsed neutron source. The instrument is constructed with a 4.5 meter incident flight path and has five counter banks at angles of 150°, 90°, 50°, 25° and 10∿5°. Each counter bank consists of Helium-3 proportional counters 1/2" diam. and 12" in active length filled to 1520 mm Hg of enriched ^3He (Reuter stokes RSP4-0412-202). Fifty counters are installed initially and aligned, in usual case, in near focussing planes to improve counting efficiency (solid angle) except 10∿5° bank which adopts so called electronic focussing. Another counter bank at 10 ∿ 5° is allowed to be set vertically for anisotropic transient studies.

The instrument has a scattering chamber, 50 cm in diam. and 150 cm in height, made of aluminum with thin windows for the scattered neutrons. The chamber as well as the incident

flight path and a beam duct to a beam stopper are evacuated together to improve signal to background ratio, while the scattered neutron paths outside of the chamber are not evacuated to make the handling of the counters convenient. A sample changer will be installed to the chamber which has five or six sample positions including samples in an image furnace or a cryostat. Incident slits are constructed by sintered $^{10}B_4C$ plates.

Annuluses of enriched ^{6}Li glass scintillator at smaller angles less than 5° will be installed inside the beam duct in near future to make Placzek correction more reliable.

Time Focussing Counter Bank

Extensive optimization studies on the momentum resolution and the counting efficiency have been performed to determine the parameters of the instrument as functions of counter diameter and active length, incident and scattered flight path, scattering angle, defocussing angle from focussing plane, and sample size, using a Monte Carlo computer code. In table 1 are summarized the main parameters of the instrument. One or two counters close to the sample in the forward banks at angles less than 50° may be used with proper masks which limit the active length when higher resolution is required.

Angular contribution to the momentum resolution for a counter bank will be expressed in terms of two components due to single counter and due to a plane of the bank, and matching of these two components is practically important to

increase the solid angle. Counters in a bank are, therefore, aligned to a plane slightly deviated from the ideal time focussing plane as shown in the table. It may be important to test whether the counter bank is realy useful even at forward angles. A computer simulation was performed to examine the accuracy of the static approximation for the counter bank in case of liquid Argon sample, $S(Q,\omega)$ of which is well known. In the simulation, integration of $S(Q,\omega)$ was performed along the instrumental integration path in Q-ω space, with a weighting function including energy spectrum and energy-dependent pulse width of neutrons emanating from the KENS moderator, energy-dependent counter efficiency, assuming actual counter configuration. Results are shown in Fig. 3 where the measured S(Q) for the counter banks at angles less than 25° lie on the ideal S(Q) in the Q-range of the figure. It is concluded that the near focussing configuration in the counter arrangement is still useful even for the forward counters.

§ Counter Configurations for Transient Studies

Structural studies in non-equilibrium states are considered to be one of the most important application of this instrument. Measurements of time-dependent structure factor $S(Q,t)$ will be classified instrumentally in the following three cases, according to the relaxation time τ.

(i) Transient phenomena with $\tau \gtrsim 1$ min

will be measured within an event in the sample, using

the time focussing configuration, with a minimum time spacing from about 0.5 to 1 min.

(ii) That with $\sim$ 1 min > τ > 50 m sec will be measured repetitively, using the time focussing configuration, with time spacing not less than the repetition period of the source (50 m sec).

(iii) That with 50 m sec > τ > several tens of μ sec will be measured repetitively by a multi-detector configuration mentioned below.

In case (iii), counters are aligned to such a plane that ΔQ of every counters take nearly the same value at given t, instead of the time focussing one, as shown in Fig. 4 where twenty-eight counters are installed at angles from 6° to 60° with a 2° step. The TOF locus of each counter in the Q-t space is also depicted in the figure, where t is defined as a time at the sample after the neutron burst. S(Q,t) at any time t will be obtained simultaneously from 28 independent S(Q) with an accuracy in time of the order of $(\Delta Q/Q)t$, say several tens of μ sec, at a region of t from about 0.5 to 1.5 m sec, in the Q space ranging from 0.5 to 5 A^{-1} which is considered to be most important in this kind of study.

§ Electronics and Data Acquisition System

In Fig.5 is shown a block diagram of the electronics and the interface circuit for the data acquisition with the pulse sequences. Special care was devoted to handle high speed signals, the counting rate of which is expected to be 4 counts/μ sec for

the backward counter bank. Number of counters connected to a pre-amplifier is limited to one or two due to the pile-up of the pulses, and consequently 25 $\sim$ 35 pre-amplifiers are necessary followed by the same number of the main amplifiers and the discriminators. The output signals from each discriminator (about 150 n sec in pulse width) are summed in 8 signals corresponding to the 8 angles and are fed to the interface. The pre-amplifier will be constructed by a hybrid circuit TRA 510 supplied by LeCroy for saving cost. To accept the signals with higher counting rate than the computer cycle time, a special interface circuit was designed which is able to perform add N instead of add one within a shortest time channel (1 μ sec). Input pulses from each fast trigger circuit are synchronized to the clock pulse and are counted by a 4 bit counter (COU) for an interval corresponds to the channel width, and are then transferred to a register (REG). Within next 1 μ sec, the memory content of the corresponding channel in the CAMAC RAM is read into ALU and added to the content of the REG, then stored in the same memory, as shown in the pulse sequence, under the control of a common control unit. Interface circuit consists of CAMAC module with 8 k words RAM (16 bit base) which is allocated into 8 independent input. Data I/O and processing are served by a computer OKITAC-system 50/model 60. In case of the multi-counter configuration for the short time transient study, extra time analysers of conventional type for 28 independent input are necessary.

Table 1 Main Parameters of HIT

angle	Q_{min}-Q_{max}/A^{-1} (λ_{max}) (λ_{min})	ΔQ at Q_{min} ~ ΔQ at Q_{max}/A^{-1}	defocussing* angle	maximum. no. of counters	solid angle/str.	L_2 min - L_2 max/cm	count. rate** (cts/sec/A^{-1})
150°	15∿100 (0.8) (0.12)	0.18∿1	15.0°	10×2	0.67	28∿44	1.9×10^3
90°	11∿89 (0.8) (0.1)	0.14∿1	6.8°	5×2	0.33	27∿54	1.3×10^3
50°	6.6∿53 (0.8) (0.1)	0.15∿1.2	7.6°	6×2	0.27	30∿65	1.7×10^3
25°	2.7∿27 (1.0) (0.1)	0.14∿1.4	3.0°	5×2	0.12	34∿118	1.5×10^3
5∿10°	0.5∿11 (1.0) (0.1)	0.13∿1.4	—	4×2 (3)	0.048	80	2.0×10^3

* deviation angle from the ideal focussing plane for improving solid angle.

** for standard V sample (10 mm ϕ × 50 mm high) obtained by scaling the Tohoku linac data.

Figure Captions

Fig. 1 Schematic drawing of HIT. Regions enclosed by broken lines on both wings are replaced by a multi-detector system aligned on dot-dashed curves in case of the short time transient study.

Fig. 2 Conceptual picture of HIT.

Fig. 3 Measured S(Q) for counter banks at various angles obtained by computer simulation. Thick solid curve shows ideal S(Q). $S^{exp}(Q)$ for the counter bank $2\theta = 25°$ are coincide with the ideal.

Fig. 4 An example of the counter arrangement for short time transient study at time range of several tens of μ sec, and TOF locus of each detector at various angles. Ellipses show resolution elements in FWHM in Q-t space and Δt represents the time resolution in this configuration.

Fig. 5 Block diagrams of electronics and interface circuit (time analyser) for HIT. Pulse sequence is for instruction.

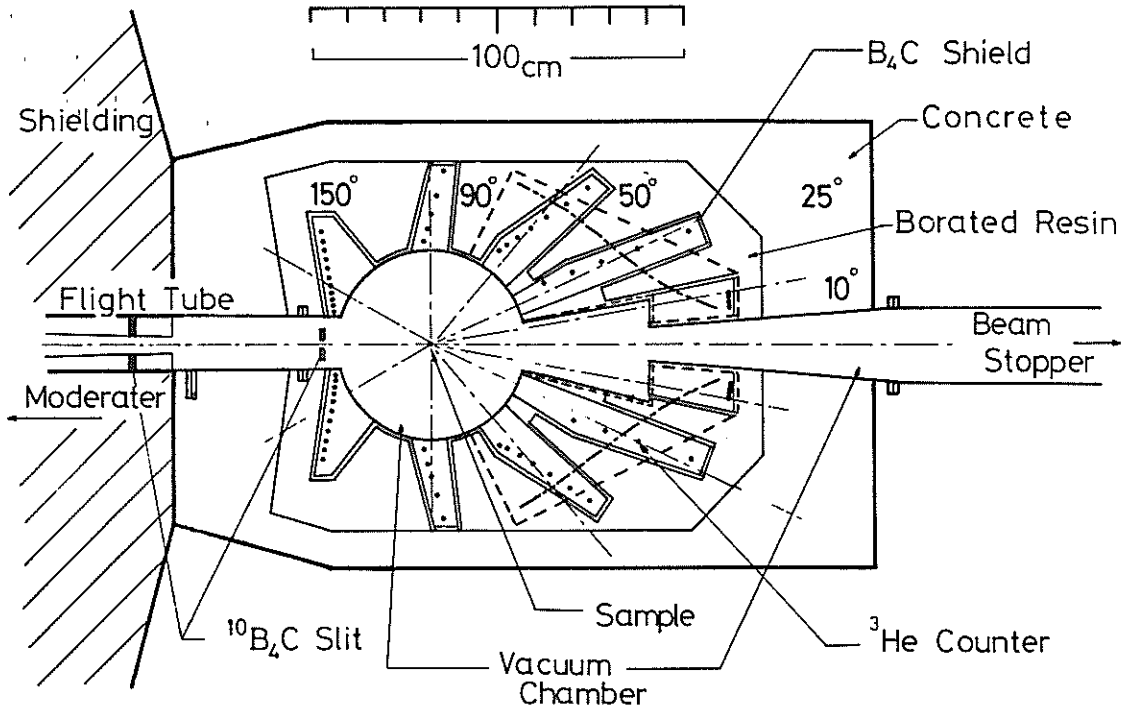
100cm
B4C Shield
Concrete
Shielding
150°
90°
50°
25°
Borated Resin
10°
Flight Tube
Beam
Stopper
Moderater
10B4C Slit
Sample
3He Counter
Vacuum
Chamber

Fig. 1

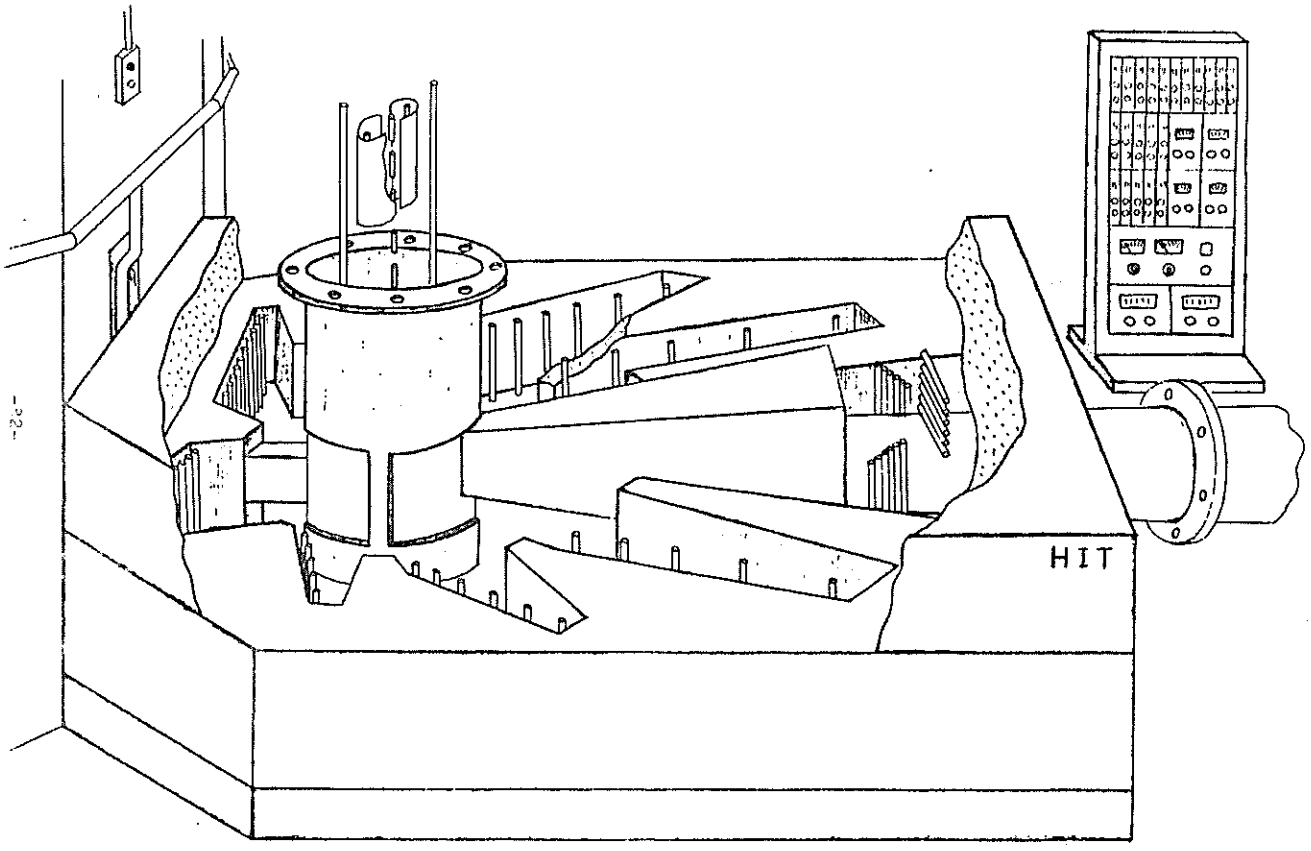
HIT

Fig. 2

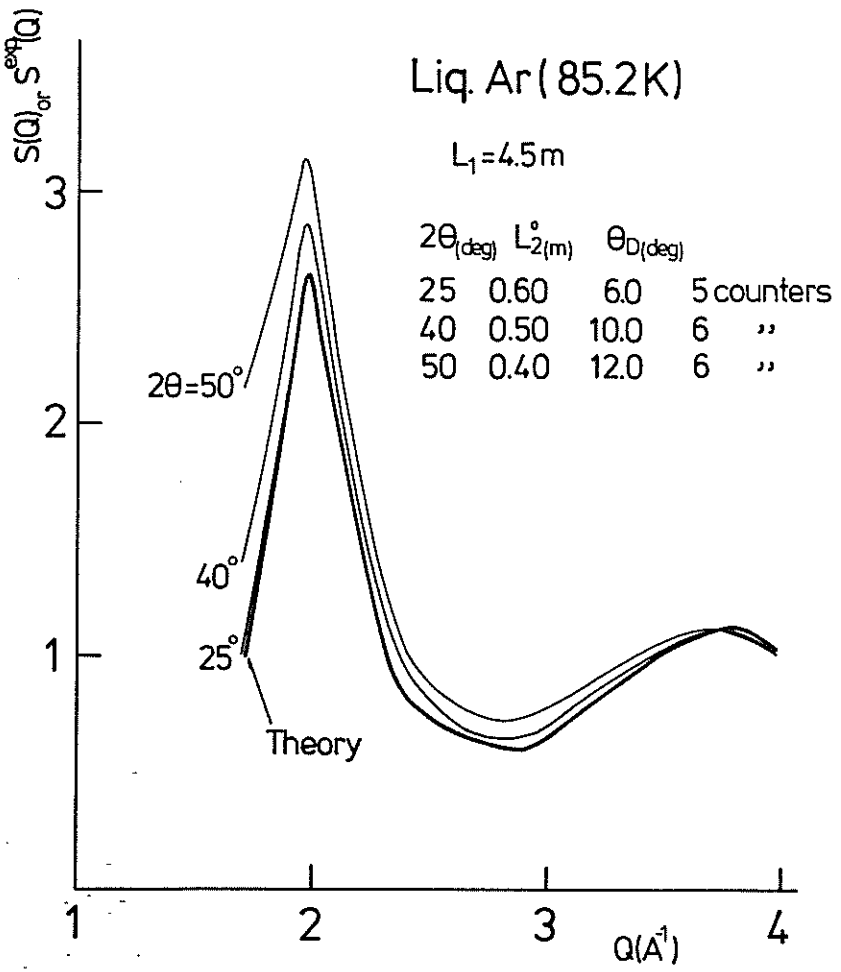
Liq. Ar (85.2K)
L_1=4.5m
$2\theta_{(deg)}$ $L^{\circ}_{2(m)}$ $\theta_{D(deg)}$
25 0.60 6.0 5 counters
40 0.50 10.0 6 ,,
50 0.40 12.0 6 ,,
2θ=50°
40°
25°
Theory
$S(Q)_{or}$ $S^{exp}(Q)$
Q(Å^{-1})

Fig. 3

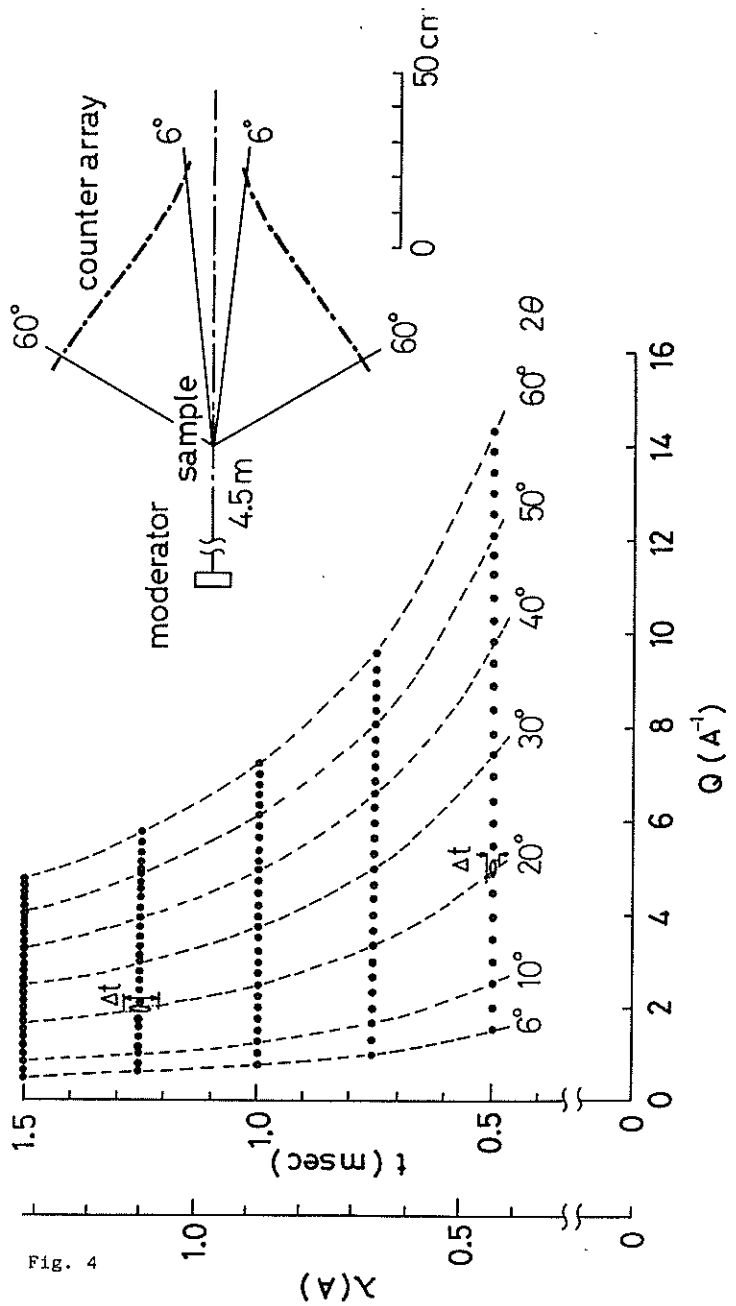
counter array
6°
6°
50 cm
0
60°
60°
sample
moderator
4.5m
2θ
60°
50°
40°
30°
20°
10°
6°
Δt
Δt
t (msec)
λ(Å)
Q (Å^{-1})

Fig. 4

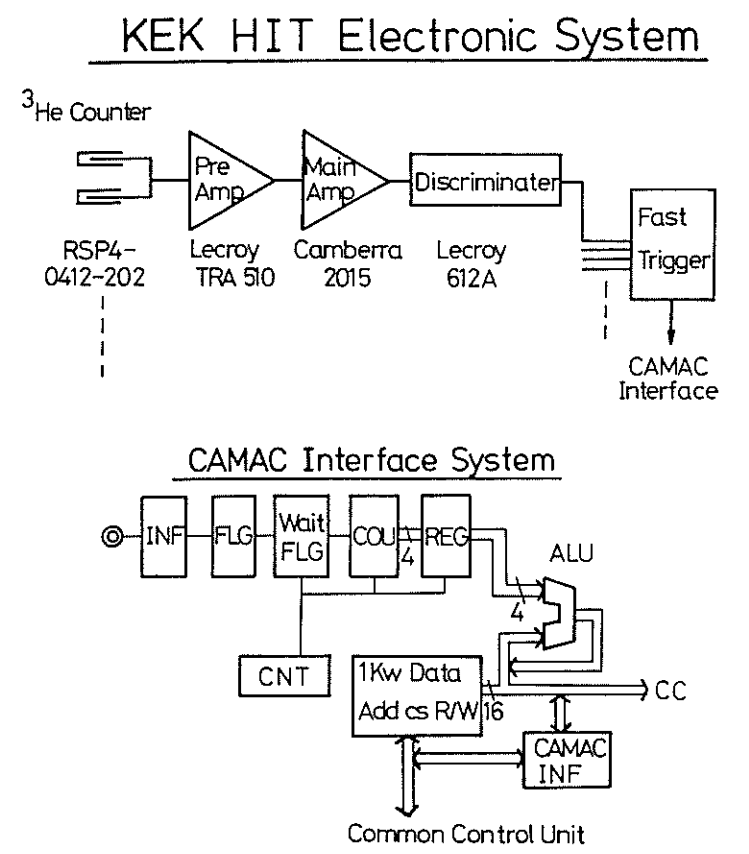

Fig. 5

4.2 Multi-Analyzer Crystal Spectrometer at KENS (MAX)

K. Tajima, Y. Ishikawa and S. Tomiyoshi†

Department of Physics, Tohoku University, Sendai, 980

† Research Institute for Iron, Steel and Other Metals, Tohoku University, Sendai, 980

1. Introduction

Neutron inelastic scattering experiments are, at present, mostly performed by the triple axis spectrometer installed at the steady thermal reactor. This type of spectrometer is particularly powerful for studying the collective excitaions as magnons or phonons, because it enables us to detect the excitations with constant Q or E mode of operation. The method, however, has the disadvantages such that the counting efficiency is rather low because of the difficulty of combining the multi-detector system to this spectrometer. The measurement of the high energy excitations (> 0.1 eV) is another weak point of this spectrometer. This is mainly because the neutron flux in the reactor is low in the epithermal neutron region and, moreover, the reflectivity of the monochromator and the analyzer is significantly reduced with increasing neutron energy. As far as these difficulties are concerned, the TOF type spectrometer incorporated with the pulsed neutron source is more suitable than the triple axis spectrometer, but it has a definite disadvantage that the measurement with constant Q or E mode cannot be realized in a conventional way.

In order to resolve the difficulty, Windsor et al. designed a new type of the TOF spectrometer,[1] which made it possible to measure the

excitations with constant Q mode of operation. The spectrometer consists of multi-analyzer crystals and detectors and the measurement of the whole dispersion curve along a crystallographic axis can be made at once. Therefore this type of machine incorporated with the pulsed neutron source is quite promissing for the determination of the dispersion up to the high energy. Their method, however, also has a disadvantage that the scans along any desired direction cannot necessarily be made.

We have improved this difficulty and designed a multi-analyzer crystals spectrometer which has wider application than theirs.[2] This machine is going to be installed at KEK spallation neutron source and this paper describes the outline of the spectrometer. The details will be soon published elsewhere.

2. Principle of the spectrometer

The principle of the TOF crystal analyzer spectrometer is displayed in Fig.1. The scattered neutron wave vector k_F is fixed by the Bragg angle θ_A of the analyzer, while the incident neutron energy k_I is determined from the neutron total flight time from the moderator to detector. The scattering diagram in the reciprocal lattice space of this configuration is displayed in Fig.2. Since k_I changes continuously, the measurement along a line parallel to k_I can be done at once by a single counter as shown by a broken line in the figure. The excitation energy $\hbar\omega$ (neutron energy loss) can be calculated as

$$\hbar\omega = \frac{\hbar^2}{2m}\left(Q_x^2 + 2\beta\,\tau_d\,Q_x\cot 2\theta_s - \beta^2\tau_d^2\right), \qquad (1)$$

where Q_x is the momentum transfer parallel to the incident neutron, $2\theta_s$ is the scattering angle at the sample, τ_d is a half of the reciprocal

lattice vector of the analyzer (π/d) and β is defined as

$$\beta = \sin 2\theta_s / \sin\theta_A \,. \qquad (2)$$

The momentum transfer Q_y perpendicular to k_I is given by

$$Q_y = \beta\tau_d \,. \qquad (3)$$

If we align many analyzer crystals with different scattering angles $\theta_A(i)$ under the condition β = constant, all scans by many detectors fall on the same line in the reciprocal lattice space. This line can be chosen to make coincide with the principal crystallographic axis as [110] of the sample. A typical example of the [110] scans with eighteen analyzer crystals is shown in Fig.3. The sample has a lattice constant a = 3.5 Å and the pyrolytic graphite (PG) crystals are used as the analyzers. The value of β = 1.91 makes the line of scan pass the reciprocal lattice point (111). The figure indicates that the scans covering the whole Brillouin zone along [110] can be made up to an energy transfer of 180 meV, if the lowest scattering angle can be reduced to 10 degrees. The scans provide at once the information which can be obtained by both of constant Q and E modes. The example almost corresponds to the case of the measurement of the excitations along [110] around (111) in a f.c.c. 3d transition metal. If we change β, the scan along other crystallographic direction starting from (111) can also be made. Note that, in case of amorphous materials or liquids where there is no defined crystallographic direction, each analyzer needs not take a common value of β.

3. Spectrometer MAX

The spectrometer which is going to be installed in KENS is equipped with fifteen analyzers which are set on a analyzer table as shown in

Fig.5. The scattering angles $2\theta_s^\circ(i)$ relative to the table are fixed, but those relative to the crystal $2\theta_s(i)$ can be changed continuously by rotating the table around the sample table. Each analyzer and detector is coupled mechanically by θ-2θ relation. Both of $\theta_s(i)$ and $\theta_A(i)$ of each analyzer can be set by a remote control so as to satisfy a relation $\sin 2\theta_s(i)/\sin\theta_A(i) = \beta$. For the analyzers we adopt the 002 reflection of the pyrolytic graphite crystal. In order to employ the PG in the transmission mode, several pieces of the PG plate ($12 \times 50 \times 2$ mm^3) are stacked with an appropriate distance as shown in Fig.6. This configuration is quite effective to economize the PG plate particularly in case of the low scattering angle. The detectors are the He^3 counters 25 mm in diameter filled with 10 at. He^3 (RS-0806-203). In case of low angle scattering the Soller collimators are inserted before and after the analyzer crystals. The collimator will be made by thin myler sheets coated with Gd_2O_3 powder.

4. Resolution of the spectrometer

The resolution of the spectrometer was estimated by calculating the resolution function by a similar method as developed by Cooper and Nathans[3] and Komura and Cooper.[4] The resolution function at $(\hbar\omega_0 + \Delta\hbar\omega, \vec{Q}_0 + \Delta\vec{Q})$ can be expressed by

$$R(\hbar\omega_0 \pm \Delta\hbar\omega\ ,\ Q_0 \pm \Delta Q) = R(\hbar\omega_0, Q_0)\ \exp\left(-\frac{1}{2}\sum_{k,\ell}^{4} M_{k\ell} X_k X_\ell\right),$$

with $\vec{X} = (\Delta Q_x,\ \Delta Q_y,\ \Delta Q_z,\ \Delta\hbar\omega)$, which is displayed by resolution ellipsoid. A typical example of the ellipsoids in the ΔQ_x - ΔQ_y and ΔQ_x - $\Delta\hbar\omega$ planes are illustrated in Fig.6, which indicate that the energy resolution $\Delta\hbar\omega/\hbar\omega$ is about 8 % for the $\hbar\omega$ = 92 meV, other examples are listed in Table 1.

5. Computer simulation experiment

In order to see the effect of the resolution more clearly, the scattering spectra $I(\hbar\omega_0\ Q_0)$ are calculated by convoluting the resolution function to the cross section for the magnon excitation;

$$I(\hbar\omega_0\ Q_o) = \int R(\hbar\omega_0 + \Delta\hbar\omega,\ Q_0 + \Delta Q)\ \sigma(\hbar\omega_0 + \Delta\hbar\omega,\ Q_0 + \Delta Q)\ \Delta\hbar\omega\ \Delta Q.$$

The magnon dispersion given in Fig.7 was assumed. In Fig.8 are shown the calculated magnon groups which would be observed by three detectors of MAX with the scattering angles $2\theta_s$ = 12°, 16° and 22° respectively, which collect the data along three scanning lines indicated in Fig.7. In the calculation the magnons were assumed to have an infinite life time. The results of the calculation suggest that the magnon groups would be significantly broaden if the magnon energy exceeds 100 meV. Note that the broadening is reduced if we replot the data in the constant E mode.

6. Intensity consideration

The total counting rate n of the neutron groups observed by MAX was also evaluated by using a formula

$$n = \frac{1}{4\pi}\,\phi(E_0)\ A\ \Delta\tau p\ \Delta E_0 \Delta\Omega_0\ \frac{d^2\sigma}{d\Omega dE}\ \Delta\Omega_1 \Delta E_1\ \pi_1\pi_2\ (\ /\text{sec}),$$

where

$\phi(E_0)$ = peak flux per unit energy per unit solid angle of the source (/cm^{2}sec eV)

A = Area of source glance by sample

$\Delta\tau$ = neutron pulse width at source

p = repetition rate

$\Delta E_0(\Delta E_1)$ = energy spread of the incident (scattered) neutron

$\Delta\Omega_0(\Delta\Omega_1)$ = solid angle spread of the incident (scattered) neutron

π_1 = efficiency of reflection of pyrolytic graphite

π_2 = efficiency of detection of neutrons by He^3 counter.

By assuming typical values for these parameters as listed in Table 2, the total counting rate is calculated to be

$$n = 8 \times 10^{-3}/\text{sec} = 690/\text{day},$$

which is satisfactory if we consider that the whole dispersion are measured at once.

In conclusion, we may say that MAX is a quite powerful spectrometer to study not only spin waves but also phonons, paramagentic scattering and incoherent scattering in amorphous or liquid. The most important point of design of the spectrometer is to reduce the back ground noise because the counting rate is rather low.

References

1) C.G. Windsor et al.; Nuc. Inst. Methods 1978.

2) Windsor has also proposed independently the same improvement which is described below (private communications).

3) M. Cooper and R. Nathans; Act. Cryst. 23 (1967) 357.

4) S. Komura and M. Cooper; Japan J. appl. Phys. 9 (1970) 866.

Figure Captions

Fig.1 The configuration of a crystal analyzer spectrometer in pulse neutron source.

Fig.2 The scattering diagram in crystal analyser spectrometer.

Fig.3 The possible scan range along the [110] around (111) in a f.c.c. crystal. The lattice parameter is assumed to be 3.5 Å. The pyrolytic graphite (002) is assumed as analysers.

Fig.4 The design of MAX which is going to be installed at KENS.

Fug.5 The design of pyrolytic graphite analyser which will be used in MAX.

Fig.6 A typical section of ellipsoid of the calculated resolution function.

Fig.7 A ferromagnetic spin wave dispersion curve with D = 100 meV $Å^2$. Three lines crossing the dispersion curve represent the scans for each $2\theta_s$.

Fig.8 The calculated intensity distributions. The life time of the spin wave is assumed to be infinity.

Table 1. Some typical energy resolutions in MAX.

β	direction	$2\theta_s$	$Q_x(\text{Å}^{-1})$	$\hbar\omega$(meV)	$\Delta\hbar\omega/\hbar\omega$
1.91	[110]	12°	3.9	158	0.19
		16°	3.7	115	0.14
		22°	3.5	81	0.09
2.71	[110]	15°	3.3	133	0.28
		20°	2.7	83	0.20
		25°	2.6	59	0.15
3.13	[111]	22°	1.9	45	0.39

Parameters:

Incident (Scattered) flight path: 6 m (1.5 m)
Collimation: 30' (all)
Analyzer: Pyrolytic graphite (002)

Table 2 Parameters for estimation of counting rate

$4\pi\phi(E_0) = 2 \times 10^{15}/\text{cm}^2 \cdot \text{sec} \cdot \text{eV}$

$A = 10 \times 10\ \text{cm}^2$

sample size $= 1 \times 3\ \text{cm}^2$

$\Delta\Omega_0 = 8 \times 10^{-6}$ (sterad.)

$\Delta\tau = 4 \times 10^{-6}$ sec

$p = 15/\text{sec}$

$\Delta E_0 = 0.01$ eV

$\Delta\Omega_1 = 2.8 \times 10^{-4}$ (sterad.)

$\Delta E_1 = 0.01$ eV

$\pi_1 = \pi_2 = 0.6$

$d^2\sigma/dE_1 d\Omega_1 = 0.1\ (\text{cm}^2/\text{sterad eV})$

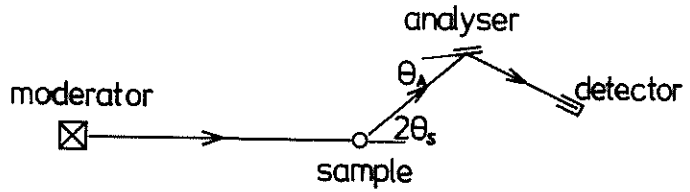

Fig. 1

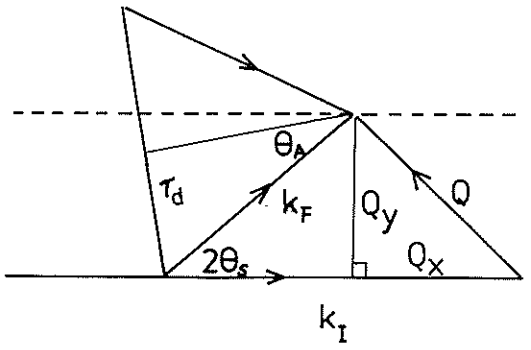

Fig. 2

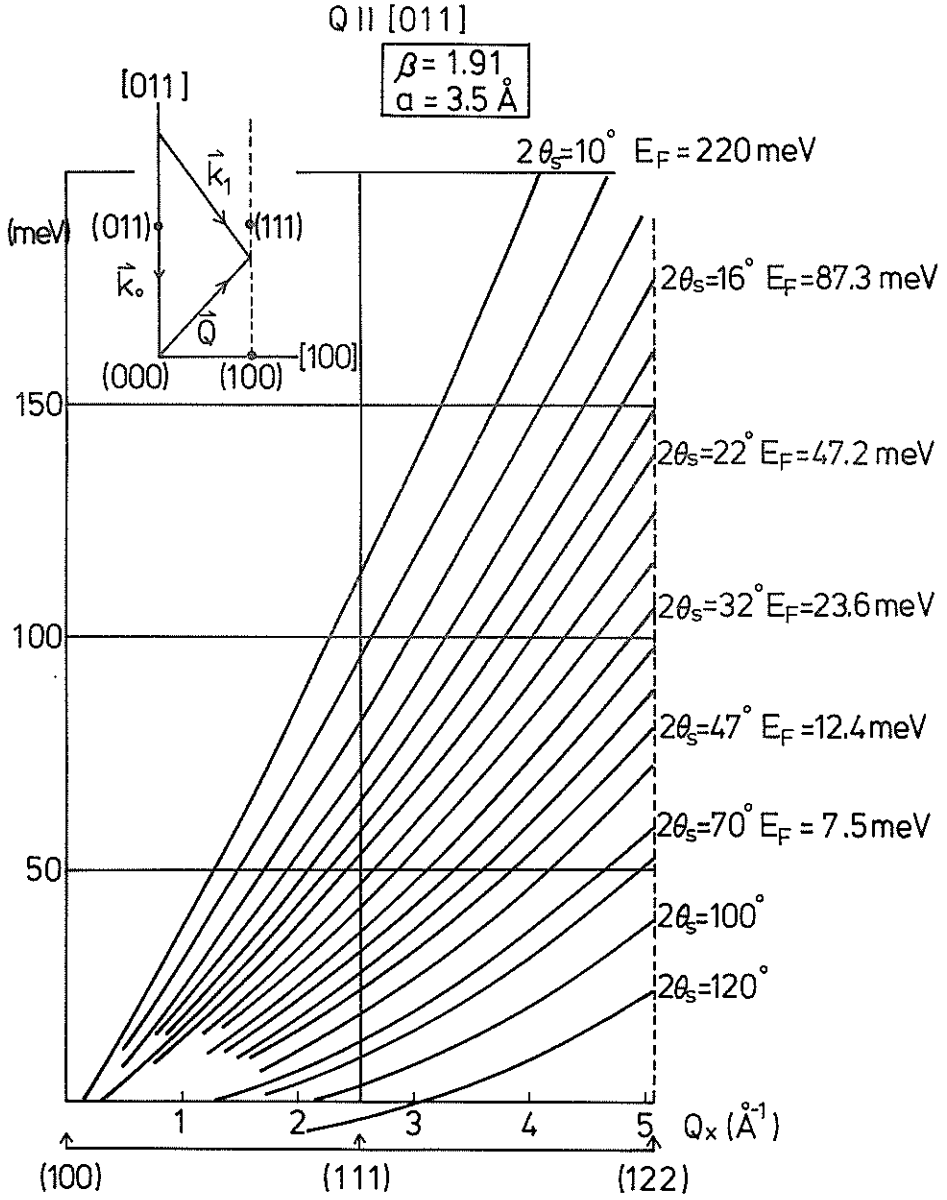
Q II [011]
β = 1.91
a = 3.5 Å
[011]
(meV)
(011)
(111)
(000)
(100)
[100]
$\vec{k}_1$
$\vec{k}_0$
$\vec{Q}$
$2\theta_s=10^\circ$ $E_F=220$ meV
$2\theta_s=16^\circ$ $E_F=87.3$ meV
$2\theta_s=22^\circ$ $E_F=47.2$ meV
$2\theta_s=32^\circ$ $E_F=23.6$ meV
$2\theta_s=47^\circ$ $E_F=12.4$ meV
$2\theta_s=70^\circ$ $E_F=7.5$ meV
$2\theta_s=100^\circ$
$2\theta_s=120^\circ$
150
100
50
1
2
3
4
5
Q_x (Å^{-1})
(100)
(111)
(122)

Fig. 3

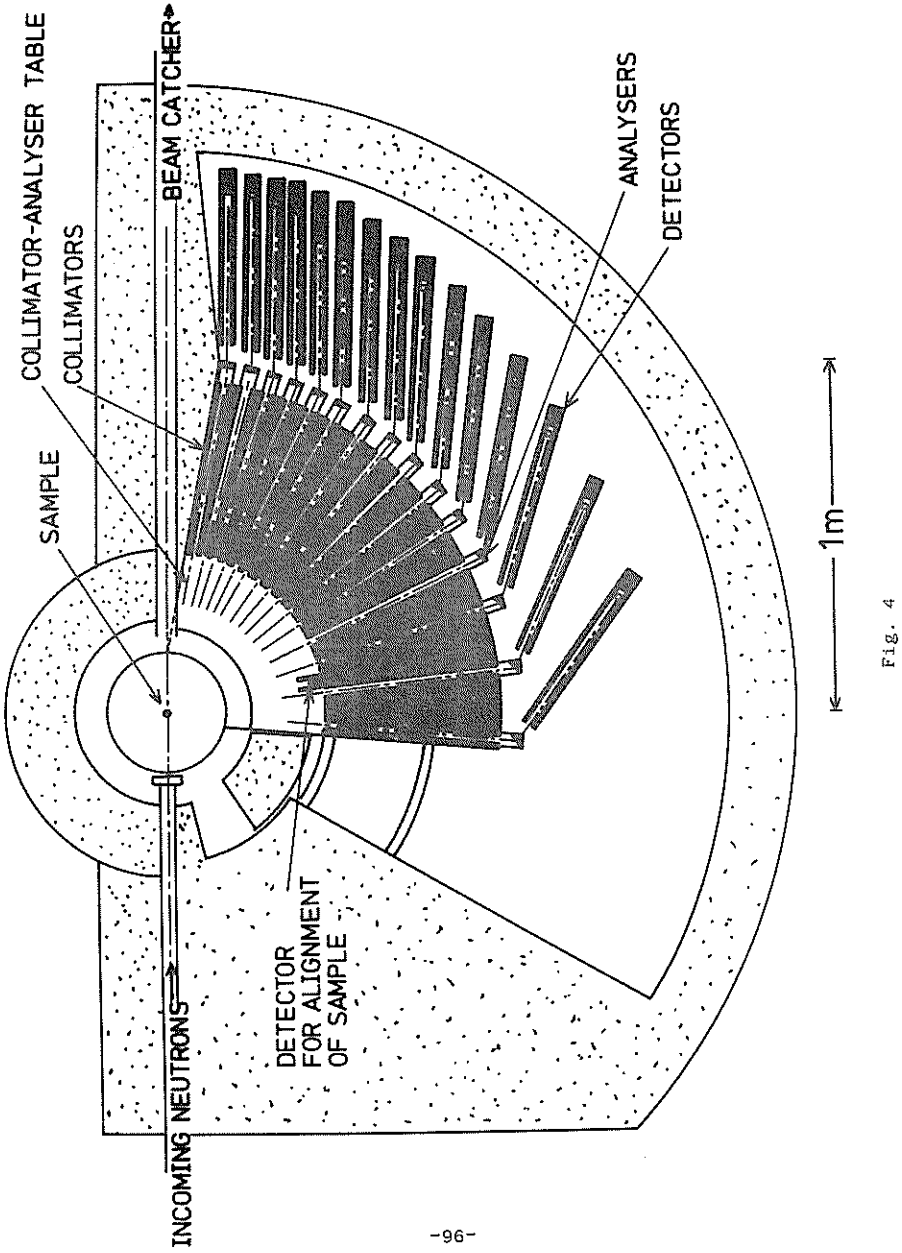
COLLIMATOR-ANALYSER TABLE
COLLIMATORS
SAMPLE
BEAM CATCHER
ANALYSERS
DETECTORS
DETECTOR FOR ALIGNMENT OF SAMPLE
INCOMING NEUTRONS
1m

Fig. 4

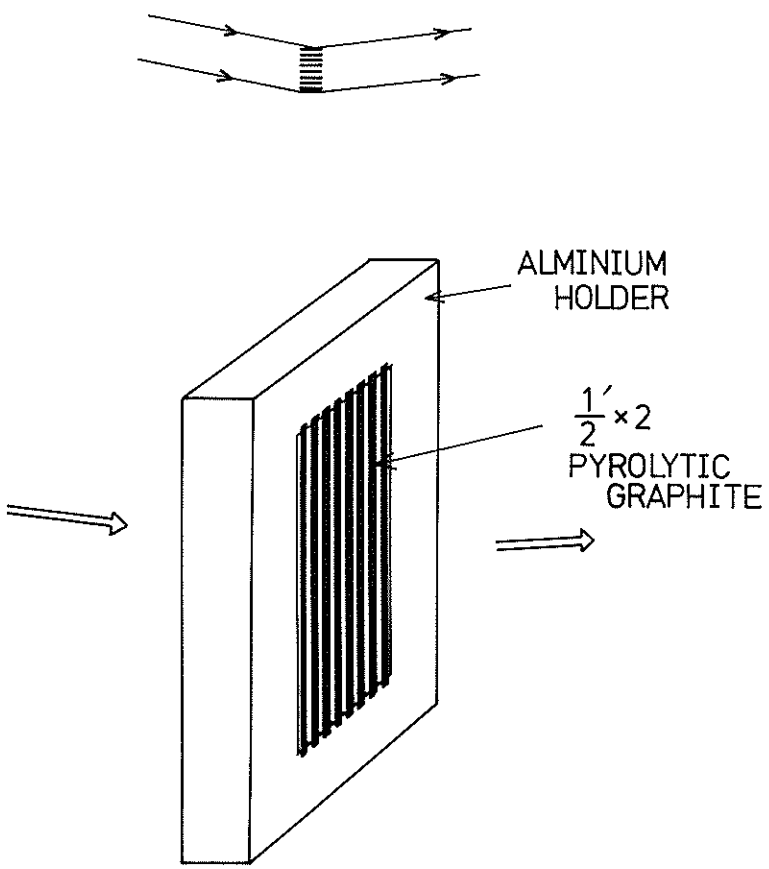

Fig. 5

RESOLUTION ELLIPSOID

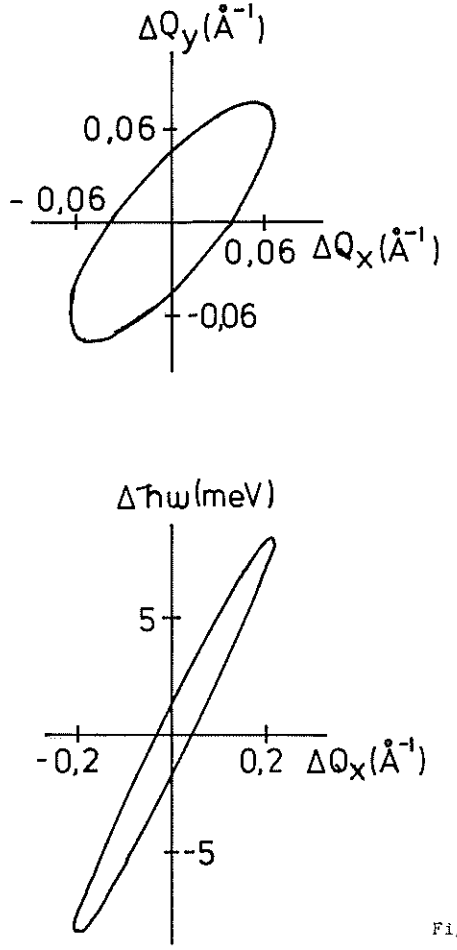

$2\theta_s = 20^\circ$

$\theta_A = 7,25^\circ$

$(E_F = 114\,meV)$

$\hbar\omega = 9\,2\,meV$

$\alpha_i = \eta = 30'$

$\Delta t_o = \Delta t_c = 10\,\mu sec$

Fig. 6

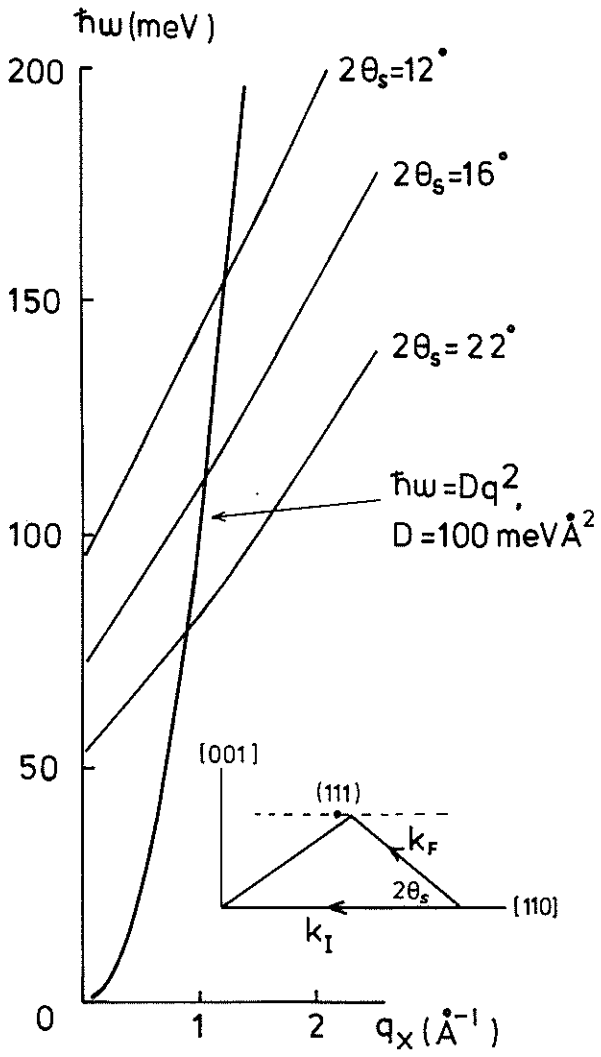
ħω (meV)
200
150
100
50
0
1
2
q_X (Å^{-1})
$2\theta_s$=12°
$2\theta_s$=16°
$2\theta_s$= 22°
ħω =Dq^2,
D =100 meVÅ^2
[001]
(111)
k_F
$2\theta_s$
[110]
k_I

Fig. 7

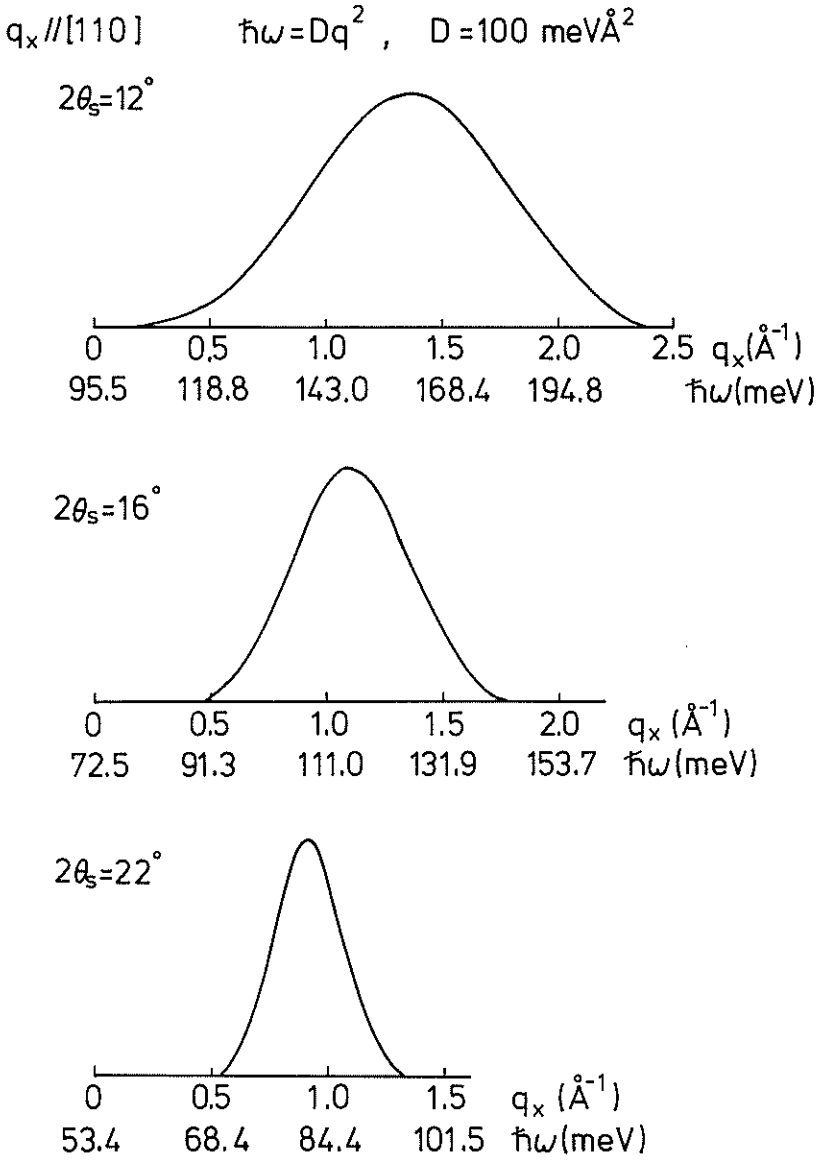
q_x//[110]
ħω=Dq^2 , D =100 meVÅ^2
$2\theta_s$=12°
0 0.5 1.0 1.5 2.0 2.5 q_x(Å^{-1})
95.5 118.8 143.0 168.4 194.8 ħω(meV)
$2\theta_s$=16°
0 0.5 1.0 1.5 2.0 q_x (Å^{-1})
72.5 91.3 111.0 131.9 153.7 ħω(meV)
$2\theta_s$=22°
0 0.5 1.0 1.5 q_x (Å^{-1})
53.4 68.4 84.4 101.5 ħω(meV)

Fig. 8

4.3 Small Angle Scattering Instrument (KENS-SAN)

Y. Ishikawa, S. Ikeda, M. Furusaka and N. Niimura*
Physics Department, Laboratory of Nuclear Science*, Tohoku University. Sendai

1. Introduction

The small angle scattering instrument incorporated with the cold neutron source is used to study the phenomena with low momentum transfers, i.e. to study the structures with long periods or long distance disturbance as well as their dynamical properties. The demand of the use of this kind of instruments has rapidly been increasing since the installation of the D11 neutron camera at ILL and similar instruments have been or are going to be installed in several different neutron sources in the world.

The problems to be studied with this machine extend over many fields of research as

(i) Metallurgy and Material Physics
(ii) Magnetism
(iii) Superconductor
(iv) Polymer
(v) Biology

The details of research programs in each field proposed for KENS-SAN will be reported separately. Here we summarize in Table 1, as an example, the periods found in the biological materials.

Table 1 Periods in Biological Materials

Materials	Period	Q ($\mathring{A}^{-1}$)
Chromatin	300∿500 Å	0.02 - 0.01
Plant virus	386 Å	0.016
Insect flight muscle	145 Å	0.043
Histone	80 Å	0.08
Ribosome	60 - 80 Å	0.1 0.08
Immunoglobin	75.8 Å	0.08
Membrane	20 Å	3.31

2. Principle of design of KENS-SAN

By considering the present requirements of research with this machine as well as the special situation that the instrument is installed on a pulsed cold neutron source, the machine was designed to satisfy following requirements.

(i) The instrument should make possible the measurement of wide ranges of momentum transfers Q without changing the machine configuration. The range of Q which should be covered is

$$10^{-3}\mathring{A}^{-1} \leq Q \leq 3\ \mathring{A}^{-1}$$

(ii) In order to increase the counting efficiency as much as possible, all wave lengths between 4Å and 12Å should be used at the same time for the measurements.

(iii) In order to improve the S/N ratio, the instrument should be installed at an exit of the neutron guide incorporated with the tail cutter to take off completely unnecessary wave lengths.

(iv) By taking an advantage of the pulsed neutron source, the machine should make possible the separation of the inelastic part as well as the measurement of inelastic scattering.

(v) The complexity arising from the situation that many wave lengths are employed at the same time should be at least partly improved by the way of data acquisition and display. Following three types of data display are considered

a) One dimensional display of the raw data against Q by summing all data with the same Q value

b) Two dimensional display of the results by adding all data with the same Q value along the same direction

c) Complete display of the scattering profile after making the resolution correction

3. Configuration of KENS-SAN

3-1. Direct view distance of neutron guide

The arrangement of the KENS-SAN instrument is displayed in Fig.1. This is designed to be installed at a distance farther than the direct view distance L_{DV} of the neutron guide to minimize the background. The guide is composed of a straight section L_o=3.5m long with a rectangular cross section a × h = 3 × 5 cm^2 and a bended section L_1=11 m long with a cross section b × h = 2 × 5 cm^2 and a curvature ρ = 820 m. The cut off wave length of the guide is 4Å. The direct view distance is then calculated by

$$L_{DV} = \sqrt{L_o^2+(a+b+4\delta)\rho} + \sqrt{(2b+4\delta)\rho} \quad , \qquad (1)$$

with δ=3mm, the thickness of the glass plate for the mirror. L_{DV} is given to be 14.47 m.

3.2. Range of wave lengths

Since the pulsed neutron source is operated with a frequency of 20Hz, and the distance from source to the detector L_t = 25 m, the range of wave length [λ] which can be employed in the measurement is given by

$$\Delta t(\text{m sec}) = \frac{mL_t}{h}[\lambda_{max} - \lambda_{min}] = \frac{L_t(m)[\lambda(\text{Å})]}{3.956} \quad , \qquad (2)$$

where Δt is a period of the pulsed source and is 50 m sec. [λ] = 7.9Å was then obtained. We selected as λ_{min}=4Å and λ_{max}=12Å, because the effective intensity of the neutron decreases by a factor 5 with respect to the highest value (λ=5Å), if λ exceeds 12Å.

3.3. Tail cutter

In order to cut the neutrons with the wave length other than [λ], a tail cutter is set at the position C_1 in Fig.1. The tail cutter is a circular disk covered with a thin Cd plate (Fig.2(b)), which rotates with a frequency of 20 Hz synchronizing with the proton beams. Fig.2(a) shows the operation diagram of the cutter. The actual size of the cutter is displayed in Fig.2(b). The cutter has a window of 72 deg. and the cut-off rise time $\Delta\tau_c$ is evaluated by

$$\Delta\tau_c = \frac{b}{\bar{r}\omega} = \frac{2}{16.5 \times 125.6} = 0.97 \text{ m sec} \qquad (3)$$

Although this value gives rise to an error of Δλ/λ=0.2 for λ_{min} = 4Å, this does not produce a significant error in the measurement, because the wave length shorter than 4Å is, in principle, cut by the guide tube. Note that the higher order wave length λ_h which can pass the tail cutter is calculated to be

$$\lambda_h = \frac{3.956(T_1+t_c)}{L_c} = 43.5\text{Å} \quad , \qquad (4)$$

the intensity of which can be practically neglected.

The syncronization of the rotation of the tail cutter with the proton beams has been realized by using a step motor PM5 - 60 C (250p/rev) fabricated by Toyo Plat Motor Co. The motor is operated with $5KH_z$ pulses obtained from a $1MH_z$

clock pulse which controls the booster synchrotron. The phase control is achieved by operating first the cutter with pulses of 4999H_z and then by adding the last one pulse at a retardation time T_r after the coincidence between the pulse generated by the cutter and the triggered pulse from the accelerator was obtained. By changing continuously T_r, we can select the start of passing wave length, λ_{min} from 0 to 10Å. The block diagram of operating the tail cutter is shown in Fig.3.

4. Detecting systems and measuring range of momentum transfers Q

Two types of counter systems are going to be used in the KENS-SAN. One is the single counter system fixed at the positions of A to G in Fig.1 and another is a two dimensional counter system which can move automatically in a large vacuum vessel. The fixed counter system is mainly used for the measurements of the range of relatively large Q values (3Å>Q>0.06Å). It will be used to supplement the small angle scattering data taken by the two dimensional counter or to extend the measurements taken by another machine HIT which covers higher momentum range. At the positions A,B and C, the He^3 counters RS-P4-0810-204 (ϕ=1",2ℓ=10" 4at. He^3) are set in two vertical positions, while at D,E and F which are inside the vacuum vessel, three counters are set along the circumference of a cone. (cf.Fig.6(a)). The two dimensional counter is a bank of 43 PSD counters developed by Missouri Univ, RS-P4-0810-204 (ϕ=1/2"2ℓ=24",6at. He^3). The distance between the bank and the sample can be changed from 1 m to 5 m without breaking vacuum. The ranges of Q which can be measured by this system is summarized in Table 2 and are also plotted in Fig.4.

Table 2 Ranges of Q measured by SAN

counters	N	L_2(cm)	D(cm)	ϕ(deg)	Qmax(A^{-1})	Qmin(A^{-1})
A	4	35	20	150	3.035	1.011
B	2	0	40	90	2.221	0.740
C	2	30	30	45	1.202	0.401
D	3	100	50	26.56	0.722	0.240
E	3	200	50	14.04	0.384	0.128
F	3	400	50	7.12	0.195	0.065
G_1	1	300	25	4.76	0.1305	0.044
G_2	1	300	10	1.91	0.053	0.017
G_3	1	300	2.5	0.48	0.013	0.004
G_1'	1	500	25	2.86	0.078	0.026
G_2'	1	500	10	1.15	0.031	0.010
G_3'	1	500	2.5	0.286	0.0078	0.0026

5. Intensity and resolution

5.1. Resolution matching

The resolution matching is the most important factor to be considered to increase the intensity in the small angle scattering instrument as is discussed in many papers. We adopt a converging slit collimator shown in Fig.5. This collimator enables to converge the beams on the center of the two dimensional counter. In this case, the neutrons arriving at R_d in a counter from any position of the sample have the same scattering angle, that is,

$$\phi = \phi_0 = R_d/\ell_2 \ . \qquad (5)$$

If we choose the widths of the collimator on the surfaces of the neutron source (the exit of the guide tube) and of the sample as well as that of the counter to be $2d_0$, $2d_1$ and $2d_2$ respectively, the error in the scattering angle $\Delta\phi$ is given by

$$\Delta\phi = \phi' - \phi = \pm[\frac{d_0}{\ell_1} + \frac{d_1}{\ell_2} + d_1(\frac{1}{\ell_1} + \frac{1}{\ell_2})] = \pm[\frac{2d_0}{\ell_1} + \frac{d_2}{\ell_2}] \ . \qquad (6)$$

Here we used the conditions for the converging slit collimator,

$$\frac{R_0}{\ell_1} = R_s(\frac{1}{\ell_1} + \frac{1}{\ell_2}), \qquad \frac{d_0}{\ell_1} = d_1(\frac{1}{\ell_1} + \frac{1}{\ell_2}) \ . \qquad (7)$$

The average error of the scattering angle $\overline{\delta\phi}^2$ is then given by

$$\overline{\delta\phi}^2 = \frac{1}{2}[2(\frac{d_0}{\ell_1})^2 + (\frac{d_2}{\ell_2})^2] \ . \qquad (8)$$

The resolution of the momentum transfers of the instrument $\delta Q/Q$ is then given by

$$(\frac{\delta Q}{Q})^2 = (\frac{\delta\lambda}{\lambda})^2 + \cot^2\phi\,\delta\phi^2 = R^2 \qquad (9)$$

By the consideration of maximizing the intensity of the scattered neutrons as will be discussed in the next paragraph, the contribution of $\delta\lambda/\lambda$ and $\delta\phi$ in Eq(9) should be given by

$$\frac{\delta\lambda}{\lambda} = \frac{1}{\sqrt{5}}R, \quad \cot\phi\,\delta\phi \sim \frac{\delta\phi}{\phi} = \frac{2}{\sqrt{5}}R \ . \qquad (10)$$

Since in the matching condition

$$(\frac{d_0}{\ell_1})^2 = (\frac{d_2}{\ell_2})^2 = d_1^2(\frac{1}{\ell_1} + \frac{1}{\ell_2})^2 \ , \qquad (11)$$

We finally get

$$\frac{d_0}{\ell_1} = \frac{d_2}{\ell_2} = \sqrt{\frac{2}{3}}\frac{2}{\sqrt{5}}\phi R = 0.73\frac{R_d}{\ell_2}R \ , \qquad (12)$$

which indicates that d_0 and d_1 are a function of R_d, ℓ_1 and ℓ_2 and they cannot be determined uniquely. On the other hand, the resolution matching of counters can be achieved by changing d_2 in proportion with R_d. If we put $R = 0.1$, then

$$\frac{\delta\lambda}{\lambda} = 0.045 \ , \quad \frac{\delta\phi}{\phi} = 0.089 \ , \qquad (13)$$

$$d_2 = 0.73\ R_d. \qquad (14)$$

In the vertical direction, by putting $d_2 = 0.625\ n$ and $R_d = 0.625(2m + 1)$ with m and n the integers representing the position and number of counters, we get

$$n = 0.73(2m + 1) \qquad (15)$$

or

m	1	2	7	10	13	16	19	21
n	1(0.22)	1(0.66)	1(1.10)	2(1.53)	2(1.97)	2(2.4)	3(2.85)	3(3.14)

The number in the parenthesis is the exact solution of Eq(15). This table indicates that it is best to employ one counter to the 9-th counter, to combine two counters up to the 18-th counter and to combine three counters for further counters.

As far as d_0 and d_1 are concerned, the resolution matching is designed to be satisfied at an average distance $\bar{R}_d = 10$ cm and we get from $d_0 = 0.073\ell_1/\ell_2\bar{R}_d$

(i) $\ell_1 = 2$m, $\ell_2 = 1$m, $d_0 = 1.46$, $d_1 = 0.48$cm,

(ii) $\ell_1 = 2$m, $\ell_2 = 3$m, $d_0 = 0.49$cm $d_1 = 0.29$cm,

(iii) $\ell_1 = 2$m, $\ell_2 = 5$m, $d_0 = 0.29$cm $d_1 = 0.21$cm.

Therefore in the tightest case of (iii), we need to devide the exit of the guide into 21 sections(3 x 7) by the collimator.

5.2. Intensity of scattered neutrons

The intensity of neutrons with wave lengths between λ and $\lambda + \Delta\lambda$ scattered in a direction between ϕ and $\phi + \Delta\phi$ is given by

$$I(\lambda,\phi) = \Phi_0(\lambda)\, d\Omega_1 \frac{d\sigma}{d\Omega}(\phi) S \Delta\Omega_2 \frac{\Delta\tau(\lambda)}{T}, \qquad (15)$$

with $\Phi_0(\lambda)$; the neutrons energy spectrum at the exit of the guide tube

$d\Omega_1, d\Omega_2$; solid angles from the sample to the source or the counter

S ; the cross section of the sample

$\Delta\tau$; the range of time channel coming from $\Delta\lambda$ and is given by $\Delta\tau = L_t \Delta\lambda / 3.956$

According to the Monte-Carlo simulation calculation,

$$\Phi_0(\lambda) = \Phi_0 \frac{\lambda_T^4}{\lambda^5} e^{-\lambda_T^2/\lambda^2}, \qquad (16)$$

with $\lambda_T = 7.6\text{Å}$. $d\sigma/d\Omega$ for the short range order is given by

$$\frac{d\sigma}{d\Omega}(Q) = \frac{4}{3}\pi R_q^3 b_N^2 e^{-\frac{1}{2}R_q^2 Q^2}. \qquad (17)$$

Therefore

$$I = A\, e^{-\frac{1}{2}R_q^2 Q^2 - \lambda_T^2/\lambda^2} \left(\frac{d_0}{\ell_1}\right)^2 \left(\frac{d_2}{\ell_2}\right)^2 S \frac{\lambda_T^4}{\lambda^5} \frac{\Delta\lambda}{\lambda} \frac{\alpha}{T}. \qquad (18)$$

By putting $\Delta\lambda/\lambda = C$, $\delta\phi/\phi = D$ and using Eqs(8) and (10),

$$\left(\frac{d_0}{\ell_1}\right)^2 = \left(\frac{d_2}{\ell_2}\right)^2 = \frac{2}{3} D^2 \phi^2, \qquad (19)$$

$$I(\phi,Q) = B\, e^{-\left(\frac{a}{\phi^2}+b\right)Q^2} Q^3 \phi D^4 C \frac{\alpha}{T}. \qquad (20)$$

From this relation the relations

$$C^2 = \frac{1}{5} R^2, \qquad D^2 = \frac{4}{5} R^2, \qquad (21)$$

are derived to maximize I under a restricted condition $R^2 = C^2 + D^2$ and we get finally

$$I(\phi,Q) = B\, e^{-\left(\frac{a}{\phi^2}+b\right)Q^2} Q^3 \phi R^5. \qquad (22)$$

If we do not employ the converging slit collimator, S should also be proportional to d_1^2 and I becomes proportional to R^7, indicating the intensity becomes 1/100 of the case with the converging slit collimator.

5.3. Resolution matching of $\Delta\lambda/\lambda$

The errors included in the wave length measurements, $\Delta\lambda/\lambda$ have two origins. The one is due to the pulse width ΔT_s of the cold neutron source and the other to the channel width Δt_c. Since ΔT_s is an order of 200μsec for the total flight time $t(\lambda)$>25m sec ,

$$\frac{\Delta\lambda_s}{\lambda} = \frac{\Delta T_s}{t} \sim 10^{-2}. \qquad (23)$$

Therefore the main part of $\Delta\lambda/\lambda$is due to the channel width which can be chosen to satisfy the resolution matching.

The data acquisition system has been designed to allocate in maximum 64 time channels which can be devided into four groups with different channel time. The devision given in Table 3 is an example where the every channel has approximately the same resolution $\Delta\lambda/\lambda$of 0.017. Therefore, the resolution matching can be achieved by combining two channels, or 32 channels are sufficient for the measurement with R = 0.1.

Table 3. Division of time channel

Division	wave length	channel width	channel No.	Total time	$\Delta\lambda/\lambda$
1	4 - 6(Å)	512(μs)	24	12288(μs)	0.016
2	6 - 8	768	16	12288	0.017
3	8 -10	1024	12	12288	0.018
4	10 -12	1024	12	12288	0.015
Total	4 -12(Å)		64	49152	

If the measurement of the Bragg peak is made with the G_2 counter (ϕ=1.9) for a crystal with mosaic spread $\Delta\theta_M$=10', one

Bragg peak has a width

$$\frac{\Delta\lambda}{\lambda} = \cot(\phi/2)\Delta\theta_M = 0.175. \qquad (25)$$

In this case the utilization of 64 channels makes it possible to have ten points for one Bragg peak.

5.4. Resolution mismatching

When the converging slit collimator is focussed at a position ℓ_2^0 and the counter is set at a different position ℓ_2 (Fig.5(b)), the resolution is inevitably decreased. It is important to evaluate it, because this is the situation which really occurs when the 2D counter is moved without changing the collimator. The scattering angles ϕ_0, ϕ and ϕ' in Fig.5(b) are then given by

$$\phi = \frac{R_0}{\ell_1} + \frac{R_d}{\ell_2} - R_S\left(\frac{1}{\ell_1} + \frac{1}{\ell_2}\right),$$

$$\phi = \phi \pm \left(\frac{d_0}{\ell_1} + \frac{d_2}{\ell_2} + d_1\left(\frac{1}{\ell_1} + \frac{1}{\ell_2}\right)\right), \qquad (26)$$

$$\phi_0 = R_d/\ell_2 ,$$

and the errors $\delta\phi$, and $\delta\bar{\phi}_2$ are calculated to be

$$\delta\phi_1 = \frac{1}{\sqrt{2}}(\phi-\phi_0) = \frac{R_S}{\sqrt{2}}\left(\frac{1}{\ell_{2_0}} - \frac{1}{\ell_2}\right) = \frac{R_S}{\sqrt{2}}\left(\frac{\pm\Delta\ell_2}{\ell_2^0\,\ell_2}\right), \qquad (27)$$

$$\delta\bar{\phi}_2 = \frac{1}{\sqrt{2}}\left[\left(\frac{d_0}{\ell_1}\right)^2 + \left(\frac{d_2}{\ell_2}\right)^2 + \left(\frac{d_0(\ell_1+\ell_2)\ell_2^0}{\ell_1\ell_2(\ell_1+\ell_2^0)}\right)^2\right], \qquad (28)$$

with $\Delta\ell_2 = \ell_2 - \ell_2^0$. $\delta\phi$ disappears when the converging condition is satisfied; $\Delta\ell_2 = 0$. Otherwise,

$$\frac{\delta\phi_1}{\phi_0} = \frac{R_S}{\sqrt{2}Rd}\,\frac{\Delta\ell_2}{\ell_2^0}. \qquad (29)$$

Therefore if R_S = 2 cm, Rd = 10 cm, $\Delta\ell_2$ = 2 m and ℓ_2^0 = 5 m, $\delta\phi_1/\phi_0 \simeq 0.056$, $\delta\phi_2/\phi_0 = 0.065$ and the total error

$$\frac{\delta\phi}{\phi_0} = \sqrt{\left(\frac{\delta\phi_1}{\phi_0}\right)^2 + \left(\frac{\delta\phi_2}{\phi_0}\right)^2} = 0.08, \qquad (30)$$

satisfies the resolution matching condition. If, on the other hand, we use the converging slit collimator focussing at ℓ_2^0=3, it becomes difficult to get the resolution matching for the counter at ℓ_2=5 m. For the counter at ℓ_1=1 m, $\delta\phi_1/\phi_0$ and $\delta\phi_2/\phi_0$ are calculated to be 0.112 and 0.063 respectively, which gives rise to $\delta\phi/\phi_0$ =0.129. In this case the resolution at R_d = 10cm is worse than 0.1, and we need to decrease either the sample size or to be satisfied with the data outside of R_d = 15 cm.

Above-mentioned considerations suggest that it is best to design the converging slit collimator so as to focuss at ℓ_2^0 = 5 m, so long that we keep the collimator unchanged during the measurements.

Note that the use of the fixed converging slit collimator makes possible to use larger sample than the case with a focussed converging slit collimator. Therefore the decrease of the intensity by a decrease of $(d_0/\ell_1)^2$ ($\propto(\frac{R_d}{\ell_2^0}R)^2 < (\frac{R_d}{\ell_2}R)^2$) (cf.Eqs(12) and (18)) is partly compensated by an increase of the sample size S ($\propto(\frac{\ell_2}{\ell_1+\ell_2^0})^2R_S^2$) ;

$$I \propto \left(\frac{R_d}{\ell_2^0}\right)^2\left(\frac{\ell_2^0}{\ell_1+\ell_2^0}\right)^2 R_S^2R^2 = \frac{R_d^2R_S^2R^2}{(\ell_1+\ell_2^0)^2}. \qquad (31)$$

Therefore the ratio of the intensity of non focussing converging slit to the maximum case is given by

$$I/Im = (\ell_1+\ell_2/\ell_1+\ell_2^0)^2. \qquad (32)$$

The intensity is then decreased by 0.5 for ℓ_2=3 m and ℓ_2^0 =5 m and by 0.18 for ℓ_2=1 m and ℓ_2^0=5 m.

5.5. Resolution matching of fixed counter systems

As mentioned in 4, SAN is equipped with the fixed counter systems at A to F.

The counter system in one position inside the vacuum chamber is composed of three straight counters with 2d in diameter and 2ℓ in length. The angular resolution $\Delta\theta$ of the counter is then determined by d and ℓ as

$$\Delta\theta_\ell = \frac{\Delta D\cos\phi}{R_o} = \frac{\Delta D}{2D}\sin 2\phi, \qquad (33)$$

$$\Delta D = \sqrt{D^2 + \ell^2} - D,$$

$$\Delta\theta_d = \frac{d}{R_o} = \frac{d}{D}\sin\phi, \qquad (34)$$

$$\Delta\theta = \sqrt{(\Delta\theta_\ell)^2 + (\Delta\theta_d)^2}, \qquad (35)$$

and the resolution R can be calculated as $R = \frac{1}{2}\cot(\phi/2)\Delta\theta$. The calculated resolutions R for different counter size are shown in Fig.6(b), which indicates that the counters at C,D, E and F should be with 2d = 2", 2ℓ = 10", while for B and A two and four sets of the counter are respectively necessary for the resolution matching.

6. Inelastic scattering

The inelastic scattering experiments as well as separation of the inelastic part can be achieved by setting another chopper at the exit of the guide tube (C_2 in Fig.1). The chopper is also a disk rotating with a frequency of 80 Hz by the same mechanism as the tail cutter described in 3.3.

6.1. Seperation of inelastic scattering

In order to seperate effectively the inelastic part, we use a gear type chopper shown in Fig.7(a), which produces a train of pulses at the chopper position as displayed in Fig.7(b). The rise time of one pulse $\Delta\tau_c$ is calculated to be $\Delta\tau_c$ = 0.24 msec from Eq(3) and the pulse is broaden by the inelastic part at the counter position after the 5 m

flight as shown in a lower part of Fig.7(b). The inelastic part can then be subtracted as shown in the figure. The energy resolution of this chopper $\Delta\lambda/\lambda$, which corresponds to $\Delta\tau_c/T(5m)$ is $\Delta\lambda/\lambda$=0.038 for λ=5Å (ΔE=0.24 meV) and $\Delta\lambda/\lambda$=0.019 for λ=10Å (ΔE=0.03/meV). The error due to the original neutron pulse width can be neglected as described in 5.3. The efficiency of the measurement is almost 1/3 of the case without energy analysis, which is quite high.

6.2. Inelastic scattering

For inelastic scattering, a chopper with one window (Fig.8(c)) will be used, which is also rotated with a frequency of 80Hz. We can choose the phase so as that the chopper opens at ①, ②, ③ and ④ on the line B in Fig.2(a) and two pulses with different wave lengths of λ_1=6.36Å and λ_2=9.27Å are obtained at the chopper position as shown in Fig.8(d). The rise time $\Delta\tau_c$=0.24 msec and the minimum detectable energy transfer is ΔE=0.14 meV for λ=6Å and ΔE=0.042 meV for λ=9Å. If we study the phenomenon with an energy transfer of ΔE=0.5 meV, the monochromatized beam pulse with a width $\Delta\tau$ can be used. $\Delta\tau$ is calculated by

$$\frac{\Delta\tau}{t(5m,6Å)} = \frac{1}{2}\frac{\Delta E}{E(6Å)} = 0.110, \qquad (36)$$

from which we get $\Delta\tau$= 0.834msec. The width of the window c to get this pulse width is determined by

$$\Delta\tau - \Delta\tau_c = \frac{c-b}{r\omega}, \qquad (37)$$

and we get c=6.77 cm. The transmission efficiency of the chopper is about 80%.

If the energy change is very small, we can put two windows in the chopper to increase the counting efficiency.

7. Calculation of neutron intensity

The total intensity of neutrons per unit area at the exit of the guide tube is evaluated by using an equation

$$\Phi_t = \int_{E_{min}}^{E_{max}} \Phi_s(n/cm^2 sec\ ev)\ \Omega_s(\lambda)\ \kappa(\lambda)\frac{\Delta\tau_s(\lambda)}{T}\ n\ dE\ , \qquad (38)$$

where

Ω_s: effective solid angle subtended by the source at the entrance of the guide.

κ : transmission efficiency of the guide tube.

$\Delta\tau_s$: pulse width of the source

T : periodical time (50msec)

n : number of pulses per sec (31/40).

All of Φ_s, Ω_s, κ and $\Delta\tau_s$ depend on λ. The energy spectrum of neutrons at the exit $\Phi_0(\lambda)$ which corresponds to $\Phi_s\Omega_s\kappa$ has been obtained by Monte-Carlo simulation calculation to be Eq(16) and $\Delta\tau_s$ is proportional to λ.($\Delta\tau_s=\alpha\lambda$) By integrating these λ dependent parts, Eq(38) is reduced to be

$$\Phi_t = 7.53\Phi_{0max}(n/cm^2 sec\ \mathring{A})\kappa_{max}\frac{\Delta\tau_s(\lambda_{max})}{T}\ n\ . \qquad (39)$$

Since $\Phi_{0max}(n/cm^2 sec\ \mathring{A}) = 0.439 \times 10^{13}$, $\kappa_{max} = 0.8$, $\Delta\tau_s(\lambda_{max})$ = 130 μsec. we get

$$\Phi_t = 4.9 \times 10^6 n/cm^2 sec \qquad (40)$$

This value can be compared with the reported values

Φ(Jülich, $\Delta\lambda/\lambda\sim 15\%$) = $2.8 \times 10^6 n/cm^2 sec$,

Φ(ILL , $\Delta\lambda/\lambda\sim 2\%$) = $2 \times 10^7 n/cm^2 sec$.

Therefore if we employ effectively all the wave lengths between 4Å and 12Å, our cold neutron source for SAN is higher than that of Jülich and about 1/4 of that of ILL. However if we try to separate or to measure the inelastic part, which is becoming the most important part of the current small angle scattering experiments, our instrument presumably have a higher counting rate even compared with that of ILL. Note that the wave length resolution of this machine $\Delta\lambda/\lambda$ is about 3%.

8. Monte-Carlo simulation calculation

Above calculations are based on a simple lnear approximation and the neutron source was assumed to emit homogeneously the neutrons in all directions. In order to examine the validity of the calculation, the Monte-Carlo simulation calculation was practiced as an extention of that made for the neutron guide tube and examples of the results of calculations are shown in Fig. 8(a) and (b), where we display a quarter of the two dimensional counter. The numerals attached to each counter line indicate resolution of this position expressed by %. The converging slit collimator focussing at ℓ_2=5m was used. The parameters of collimator are the same as those were used in previous calculations. The figure shows that the resolution R=0.1 is achieved nearly at R_d=10cm, indicating that the linear approximation is correct. In Fig. 9(a) and (b) are also plotted the values of Q_{min} (Q_{max}) obtained in these configuration.

Figure Captions

Fig. 1. Configuration of KENS-SAN

Fig. 2. Tail cutter (b) and its operation diagram (a)
A and B in Fig. 2(a) correspond to C_1 and C_2 positions in Fig. 1 respectively.

Fig. 3. Block diagram of operation of tail cutter

Fig. 4. Range of momentum transfers covered with KENS-SAN. A, B, C, D, E and F correspond to the data with fixed counters, which Gn represents the range with 2D counter set at n m from the sample.

Fig. 5. The principle of converging slit collimator

Fig. 6. Angular resolutions of fixed counters

Fig. 7. The second chopper at C_2 for KENS-SAN (a) a gear type chopper for separating inelastic part and (c) one window chopper for inelastic scattering (b) and (d) are the trains of pulses obtained by these choppers at C_1 and counters respectively.

Fig. 8. Monte-Carlo simulation calculations for momentum resolution on 2D counter placed at 3m (a) and 5m (b).

Fig. 9. Values of minimum (maximum) momenter transfers Q_{min} (Q_{max}) on 2D counter at 3m (a) and 5m (b).

KENS-SAN Arrangement

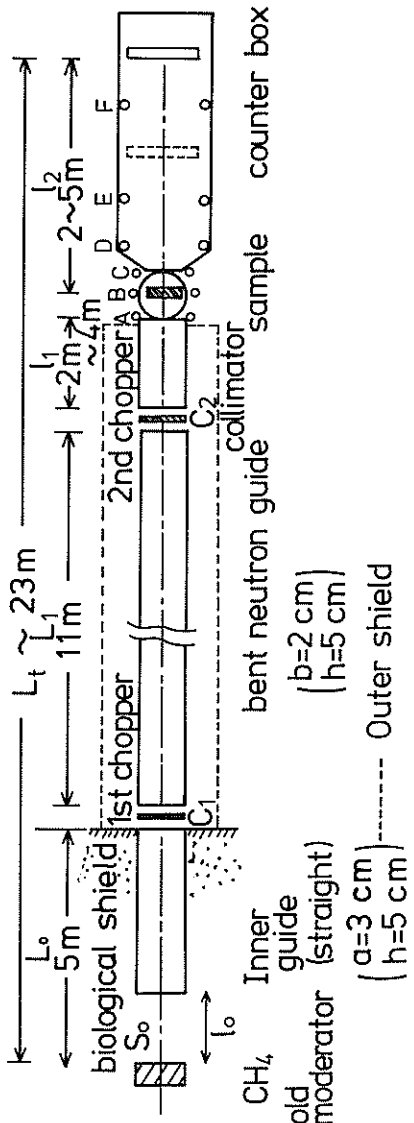

Fig. 1

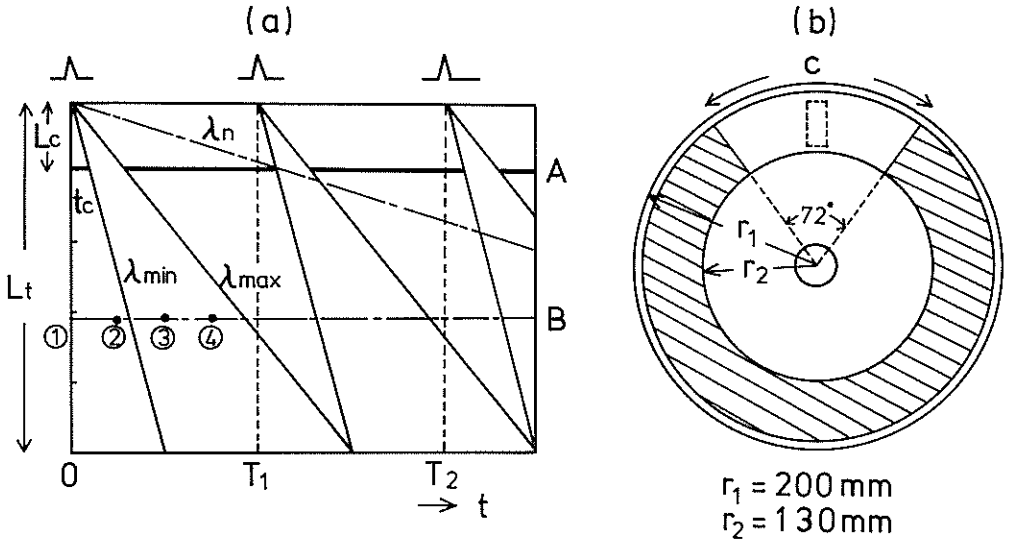
(a)
(b)
C
L_c
λ_n
A
t_c
λ_{min}
λ_{max}
L_t
①
②
③
④
B
0
T_1
T_2
t
72°
r_1
r_2
$r_1 = 200\,mm$
$r_2 = 130\,mm$

Fig. 2

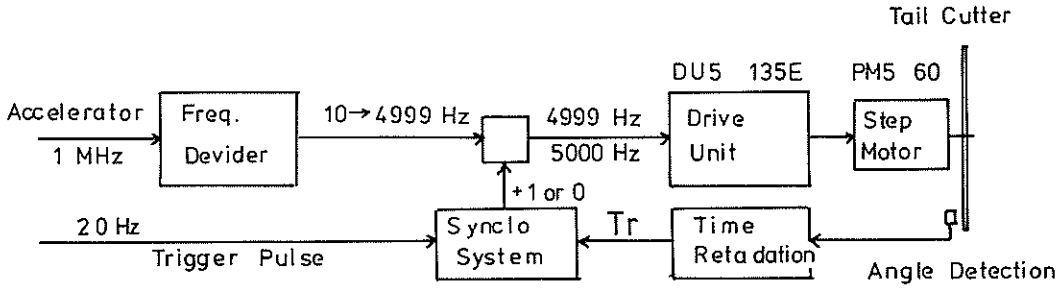
Tail Cutter
DU5 135E
PM5 60
Accelerator
1 MHz
Freq.
Devider
10→4999 Hz
4999 Hz
5000 Hz
Drive
Unit
Step
Motor
+1 or 0
20 Hz
Trigger Pulse
Synclo
System
Tr
Time
Retadation
Angle Detection

Fig. 3

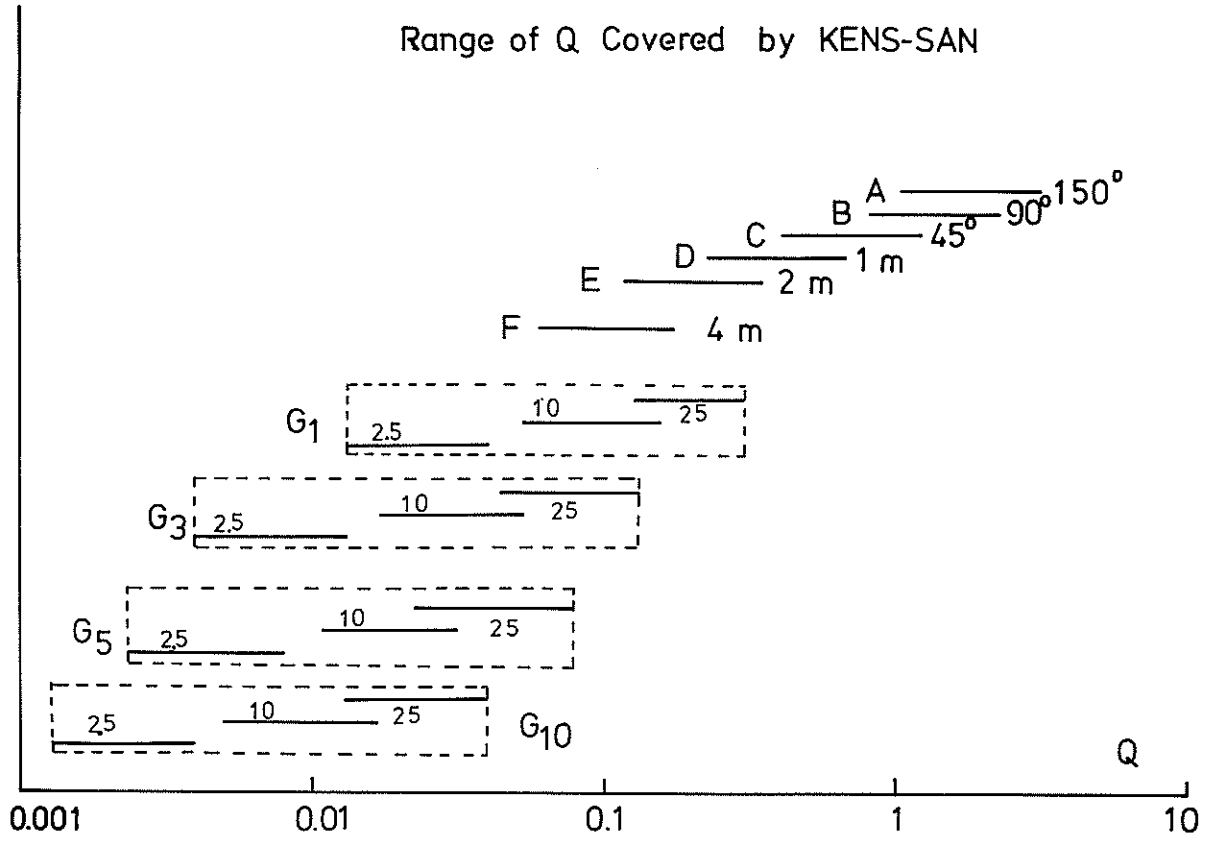
Range of Q Covered by KENS-SAN
A
B
C
D
E
F
150°
90°
45°
1 m
2 m
4 m
G1
G3
G5
G10
2.5
10
25
Q
0.001
0.01
0.1
1
10

Fig. 4

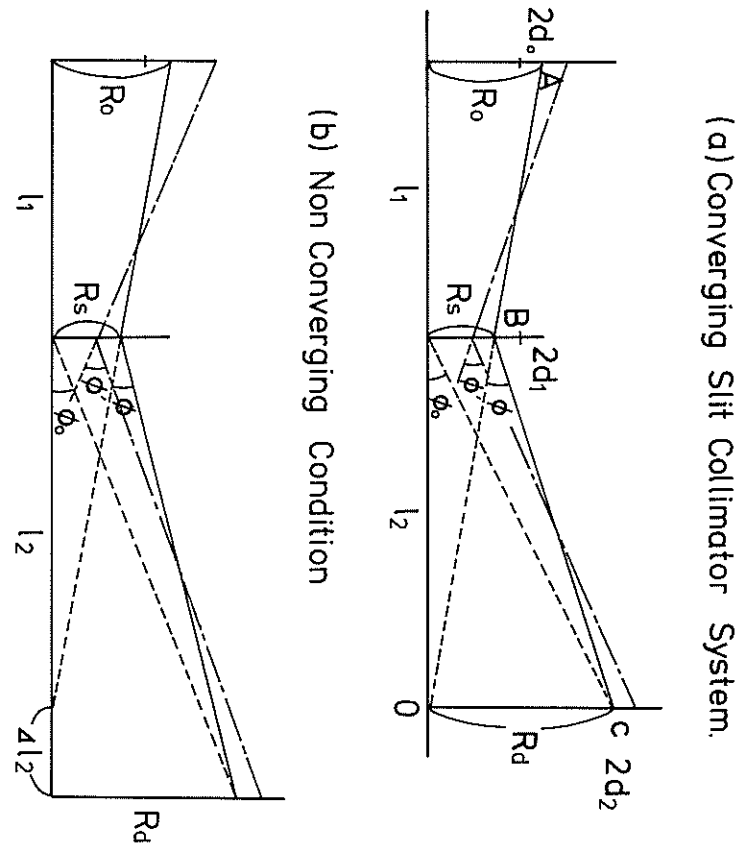
(a) Converging Slit Collimator System.
(b) Non Converging Condition
2d0
Ro
Rs
Rd
l1
l2
A
B
C
2d1
2d2
Δl2
φ
φ0
0

Fig. 5

Resolution Matching of Fixed Counters

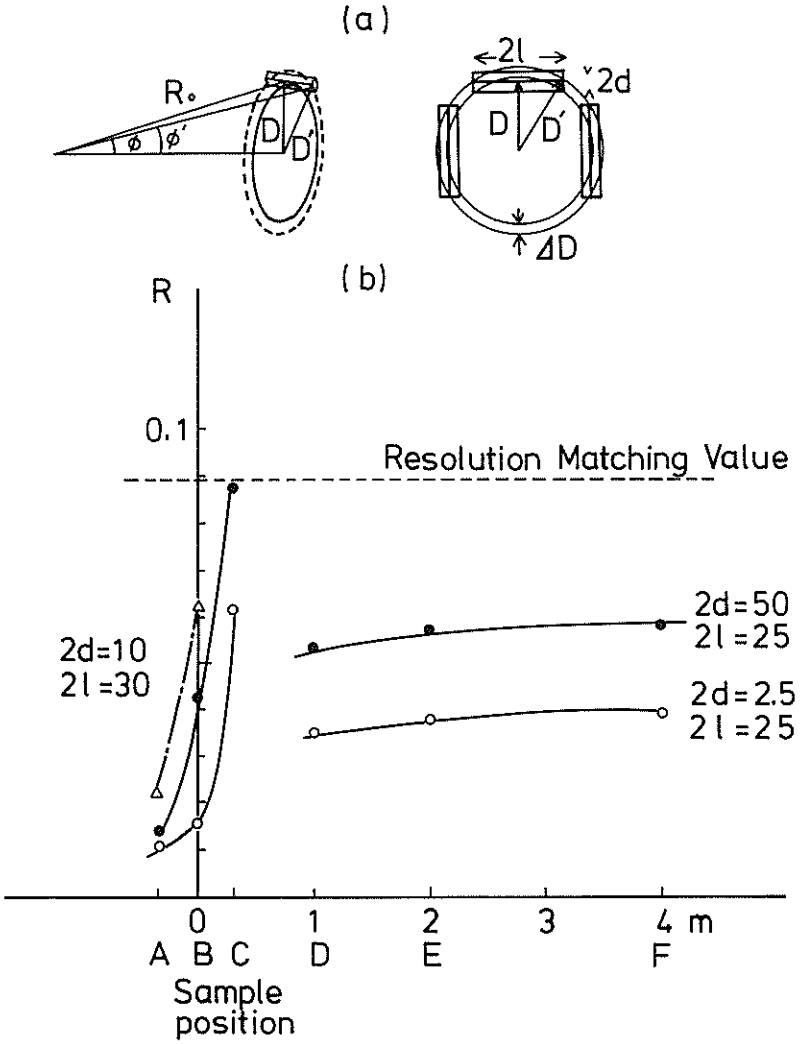

Fig. 6

(1) Chopper for Rejecting Inelastic Part

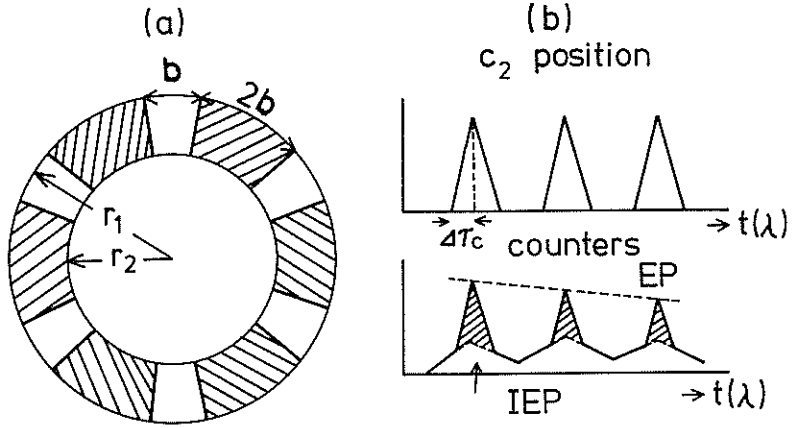

(2) Chopper for Inelastic Scattering

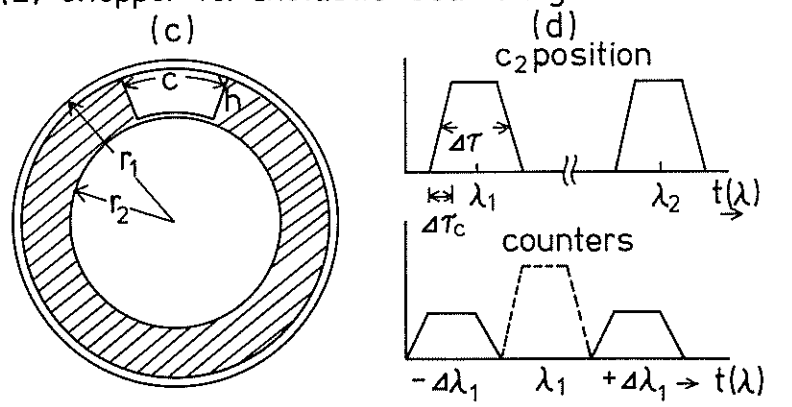

Fig. 7

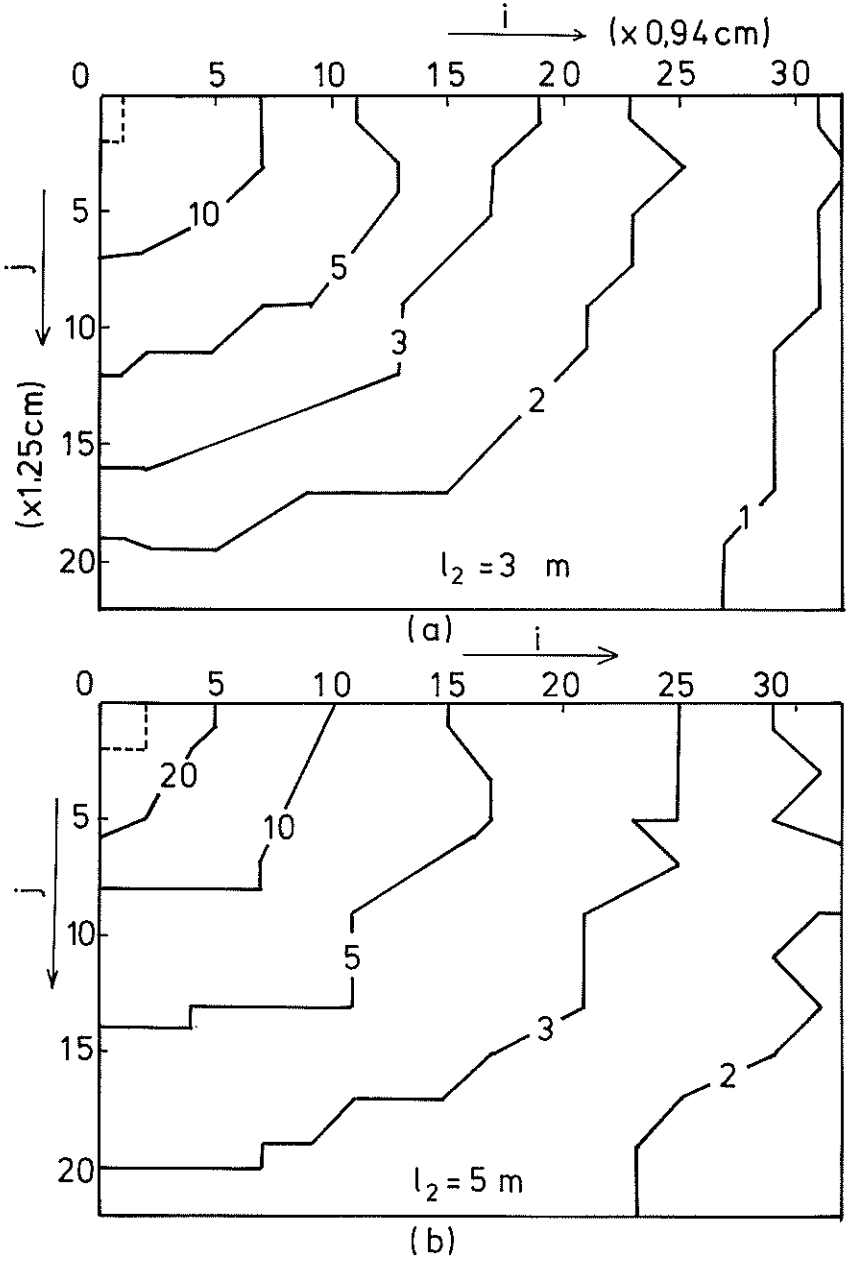
i
(x 0,94 cm)
0
5
10
15
20
25
30
j
(x1,25cm)
10
5
3
2
1
l_2 = 3 m
(a)
i
20
10
5
3
2
l_2 = 5 m
(b)

Fig. 8

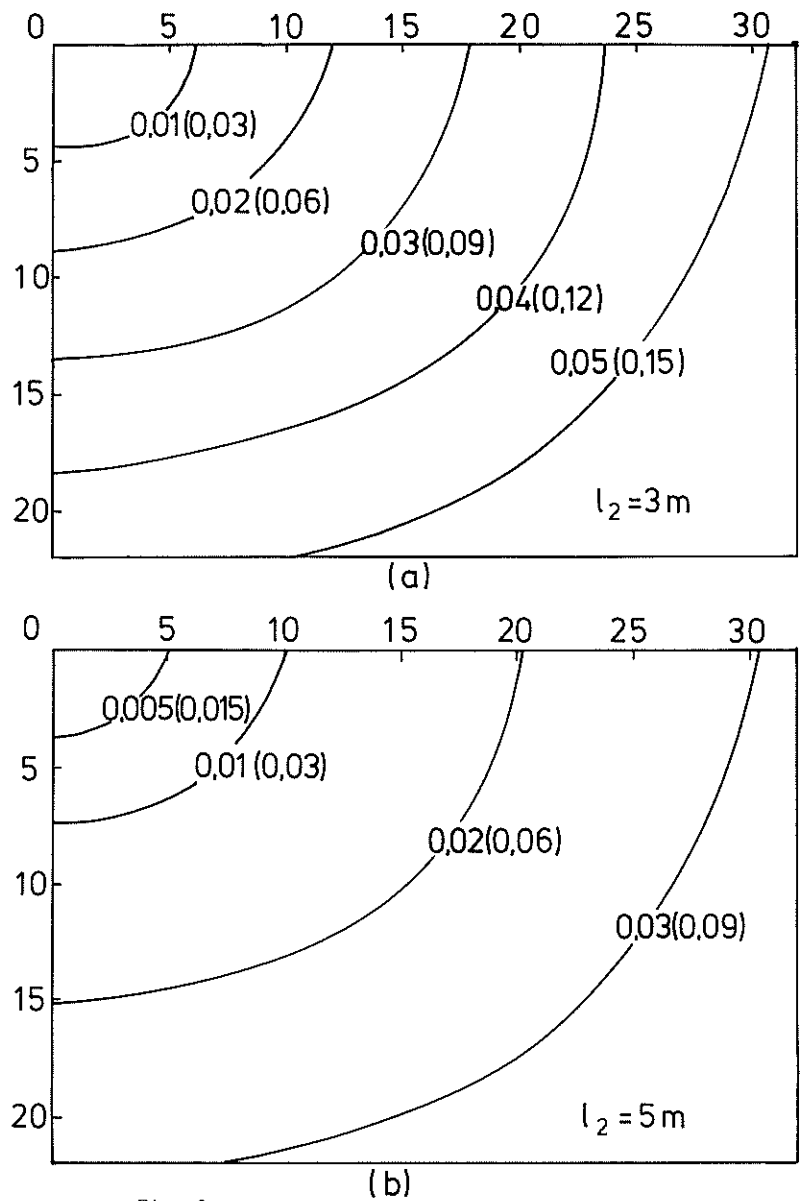
0
5
10
15
20
25
30
0,01(0,03)
0,02(0,06)
0,03(0,09)
0,04(0,12)
0,05(0,15)
l_2 = 3 m
(a)
0,005(0,015)
0,01 (0,03)
0,02(0,06)
0,03(0,09)
l_2 = 5 m
(b)

Fig. 9

Large Analyser Mirror Low Energy Spectrometer (LAM)

K. Inoue*, Y. Kiyanagi*, M. Kogi† and Y. Ishikawa†

* Department of Nuclear Engineering, Faculty of Engineering,
Hokkaido University, Sapporo
† Physics Department, Faculty of Science,
Tohoku University, Sendai

1. Introduction

The large analyser mirror spectrometer (LAM) is a quasielastic spectrometer which has two sets of analyser mirrors for conventional resolutions and high efficiency (Bragg angle ∿40°) and for slightly higher resolutions (Bragg angle ∿80°). The instrument can be readily applied to the studies of non-periodic motions in liquids, ionic solutions, hydrogen diffusion in metals, diffusion and micro-Brawnian motion of polymers, adsorbed materials, various gel materials, and others. In future studies the quasielastic peak profile analysis at large Q-values will be important in the exploration of complicated molecular motions. Precise observation of the quasielastic peak profile, and not only of the peak width, is accomplished by obtaining good statistics and removing spectral distortions. The former object is attainable by using the KENS, and the latter by using inverted geometry and the cold neutron flux property.

2. Design Considerations

The design principle of the LAM is the same as that of the LANDAM quasielastic spectrometer at Hokkaido University, that is, it employs a cold neutron source based upon a 45 MeV electron linear accelerator. Up to now, many quasielastic investigations have been made by measuring energy-gain scattering, and the scattered neutron spectra observed by time-of-flight spectrometers have been considerably distorted by the time factor t^{-3}. Ideally, the scattered neutron spectra should be free of such a large spectral distortion.

Using the inverted geometry method the neutron counts on the n-th time-analyser channel are given by

$$\eta(t_n) = \text{const.}\iiint \phi(E_1,t)\sigma(E_1\to E_2,\theta)R(E_2) \times \delta(t_n - t - L_2/\sqrt{2E_2/m})\,dE_1\,dE_2\,dt, \qquad (1)$$

where $\phi(E,t)$ is the incident neutron spectrum impinging on the specimen, $R(E)$ is the energy resolution function of the analyser mirror, and L_2 is the second flight path length. Data analysis requires precise data for $\phi(E,t)$. Fig. 1 shows the time-energy distribution of neutrons emanating from a surface of the cold source measured on the LANDAM. In the KENS cold source, a similar distribution can be expected.

By using appropriate approximations, i.e., an ideal resolution and a separated expression for incident neutron time-energy spectrum; Eq.(1) can be simplified to

$$\eta(t_n) = \text{const.}F(t_n)\sigma(E_1\to E_2,\theta). \qquad (2)$$

Here F(t) is the neutron time spectrum observed by the time-of-flight method, which is of the nearly flat distribution in the cold neutron energy region as shown in Fig. 2. In energy-gain scattering spectrometers (direct geometry), $\eta(t_n)$ is written approximately as follows

$$\eta(t_n) \approx \text{const.} t^{-3} \sigma(E_1 \to E_2, \theta). \qquad (3)$$

In the latter case, as mentioned above, the spectral shape includes a considerably large distortion. On the other hand, Eq. (2) shows that using inverted geometry no such spectral distortion appears because of the nearly flat distribution of F(t), as illustrated in Fig. 3.

We may also expect to achieve high efficiency by taking advantage of the high neutron flux emanating from the KENS, and by using large area analyser mirrors. In terms of energy resolution, the duration time of the neutron pulse is essential in spectrometers using a pulsed source. We have solved the problem of duration time by adopting a procedure for spectral analysis on the rising side of the peak without using a chopper. Using an elastic scatterer, the scattered neutron spectrum gives a measure for the resolution of the facility, as expressed approximately here

$$\eta(t_n) \approx \text{const.} F(t_n) \int f(t_n - t) \tilde{R}(t) dt, \qquad (4)$$

where f(t) is the time distribution of $\phi(E,t)$ and $\tilde{R}(t)$ is the time resolution function of the analyser mirror. Eq.(4) shows that as long as the peak width of $\tilde{R}(t)$ is sufficiently small, the rise-time of $\eta(t_n)$ can be determined mainly by the rise-time of f(t), which is illustrated in Fig. 1.

3. Description of Spectrometer

3.1 Layout of Instruments

The LAM spectrometer has two sets of analyser mirrors. One of them has four mirrors of the 40° Bragg angle, and the other has two mirrors of 80°. The layouts of these instruments are shown in Figs. 4 and 5. The cold neutrons emanating from the cold moderator chamber impinge directly on the specimen for the 40° analyser mirrors. For the 80° analyser mirrors, the cold neutrons drift along a guide tube from the source to the specimen. The design parameters are given in Table 1.

The specimen and analyser assemblies are shielded by cadmium sheets and by about 10 cm borated plastic. Furthermore, each set of the analyser assembly is shielded by an shield to prevent the stray neutrons scattered from other analyser assemblies.

3.2 Analyser Assembly

Each analyser assembly consists of a mirror, a beryllium filter and a ^{3}He counter. A schematic illustration of the analyser assembly is shown in Fig. 6. The mirror is made of pyrolitic graphite crystals. A small beryllium filter is used to remove the higher order reflections. The 25 mm in diameter ^{3}He counter is located on the opposite focusing point to the specimen.

About 140 pieces of pyrolitic graphite crystals with a mosaic spread of 1.2° and a thickness of about 2 mm are located on an optimally curved array. In order to minimize the energy spread in the analyser assembly, the shapes and dimensions of the specimen and counter window have been determined so that the various neutron flight paths in the analyser assembly have narly the same Bragg angle and the same length. The energy resolution is adjusted by varying the sample shape and dimension.

The angle resolution function of the analyser mirror is

$$R_0(\psi) = \text{const.} \iiint \varepsilon(\vec{r},\vec{\Sigma},\vec{S})\delta[\psi-\psi_0(\vec{r},\vec{\Sigma},\vec{S})]d\vec{r}d\vec{\Sigma}d\vec{S} \ , \qquad (5)$$

where $\vec{r}$, $\vec{\Sigma}$ and $\vec{S}$ denote positions on the specimen, the mirror and the counter window, respectively. Here $\psi_0(\vec{r},\vec{\Sigma},\vec{S})$ is an angle determined by these three positions and $\vec{\Sigma}$ is the vertex of the angle. $\varepsilon(\vec{r},\vec{\Sigma},\vec{S})$ represents the influences of projection and the crystal mosaic spread. The analysed neutron intensity and the energy resolution of the mirror are affected by the shape of the mirror and the dimensions of the analyser assembly, as shown in Fig. 7. In addition, the results of various calculations for the characteristics concerning the effects due to aberration, mosaic spread and Bragg angle are shown in Figs. 8 to 10.

4. Data Analysis

If accurate information from the measured spectra is desired, not only the determination of the FWHM in the quasielastic peaks, but also the analysis of their profiles is required. If the problem of curve fitting is encountered, a technique for statistical data analysis becomes necessary. Plans for the development of such a data analysis computer program are now in progress.

Frequently, the relation between the neutron spectra and unknown parameters which appear in the scattering functions is not linear. The preliminary results of our numerical experiments are shown in Fig. 11. Successive minimization of objective function M has been performed, and after four iterations the fitting curve and non-linear unknown parameters were determined. M was used for the χ^2-test, which tested the validity of the scattering model.

5. Preliminary Experiments on Prototype Spectrometer

Figures 12 and 13 illustrate some of the results we have obtained from the prototype spectrometer LANDAM. Fig. 12 shows the time evolution of neutron spectra from cement paste after it was mixed. By analysing the TOF-spectra we can measure the free and bound water contents at relevant time intervals during the hydration process. Fig. 13 is the raw data showing the TOF-spectrum of para magnetic scattering from $NiTiO_3$ at ambient temperature. In addition to its application in quasielastic experiments, the LAM spectrometer may also be used to investigate low energy transfer phenomena.

Table 1

	LAM 40	LAM 80
Neutron Source	cold neutron	cold neutron
Arrangement	inverted geometry	inverted geometry
Analyser Assembly		
Number of Mirrors	4	2
Bragg angle	40°	80°
Pyrolytic graphite		
number of pieces	144/mirror	144/mirror
size	1.2×1.2×0.2 cm^3	1.2×1.2×0.2 cm^3
mosaic spread	1.2°	1.2°
Filter	Be	Be
Flight Path	direct	guide tube
Energy Resolution	60 - 200 μeV	30 - 60 μeV
Momentum Transfer	0.24 - 2.8 $\mathring{A}^{-1}$	0.2 - 2 $\mathring{A}^{-1}$

Figure Captions

Fig. 1 Neutron time and energy spectrum emanating from surface of 20°K methane cold moderator.

Fig. 2 Neutron spectra from cold moderator and ambient temperature water moderator as a function of time-of-flight.

Fig. 3(a) Typical example of scattering function.

(b) Time-of-flight spectrum corresponding to the scattering function by using an inverted geometry spectrometer.

(c) Time-of-flight spectrum corresponding to the scattering function by using a direct geometry spectrometer.

Fig. 4 Configuration of LAM-40.

Fig. 5 Configuration of LAM-80.

Fig. 6 Sketch showing the use of analyzer mirror and beryllium filter.

Fig. 7 Resolution function of the analyzer mirror LAM-40 versus scattering angle.

Fig. 8 Effect of mosaic spread of the analyzer crystals.

Fig. 9 Correction of aberration of the analyzer mirror; (a) With correction. (b) Without correction. (See the sharper rise-up of the resolution function with the correction than the one without it.) Lower part of the figure; partial resolution functions of the mirror corresponding to (a).

Fig. 10 Resolution functions of the analyzer mirror LAM-80 versus scattering angle.
(a) Sample dimensions are outer diameter 7 mm, inner diameter 6 mm and height 40 mm.
(b) Sample height 80 mm. The other dimensions are same as (a).
(c) The same as (b), but with correction of aberration.
(d) Inner diameter is zero. The other conditions are same as (c).

Fig. 11 Result of the curve fitting. Number of unkown parameters is four. Converged value of minimum function, M, is 127.59, whereas critical value of χ^2 is 143.25 belonging to a level of significance 5% and 117 degrees of freedom. We can therefore conclude that the agreement is very good.

Fig. 12 Results from measurements on the LANDAM for the free water and combined water in cement paste. TOF spectra from specimen were measured at relevant time intervals after preparation.

Fig. 13 Typical spectra of the paramagnetic scattering from $NiTiO_3$ at ambient temperature observed with the LANDAM.

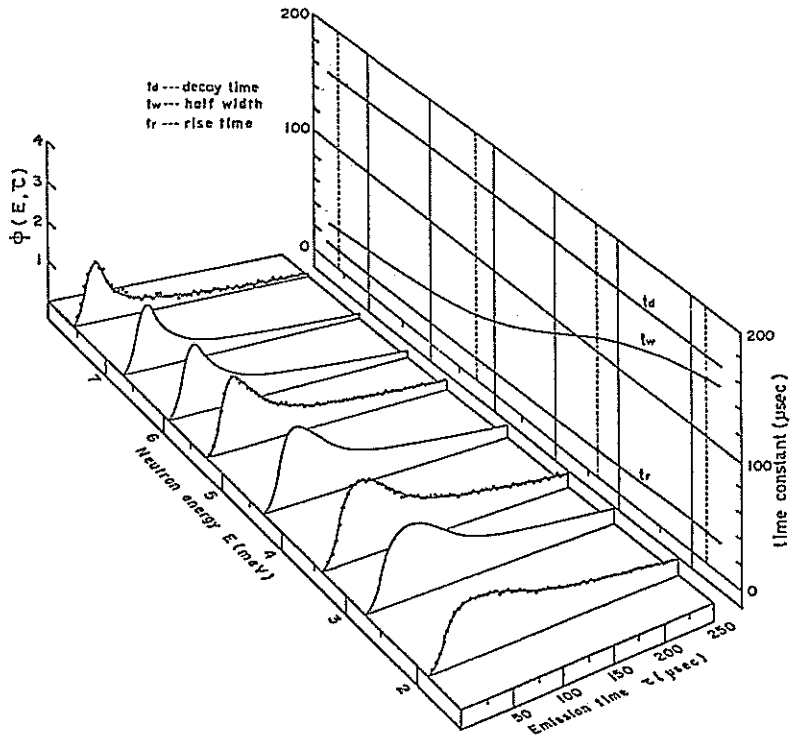

Fig. 1

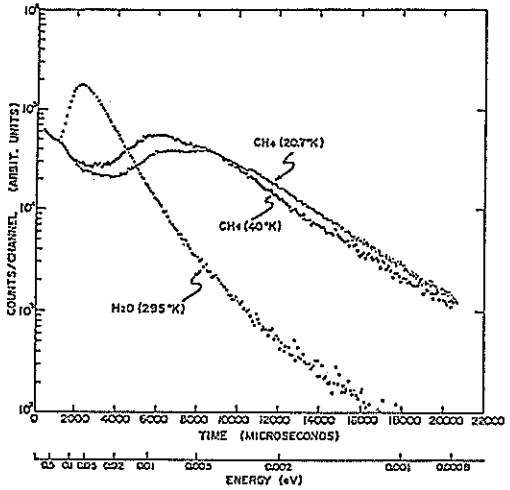
CH4 (20.7°K)
CH4 (40°K)
H2O (295°K)
COUNTS/CHANNEL (ARBIT. UNITS)
TIME (MICROSECONDS)
ENERGY (eV)

Fig. 2

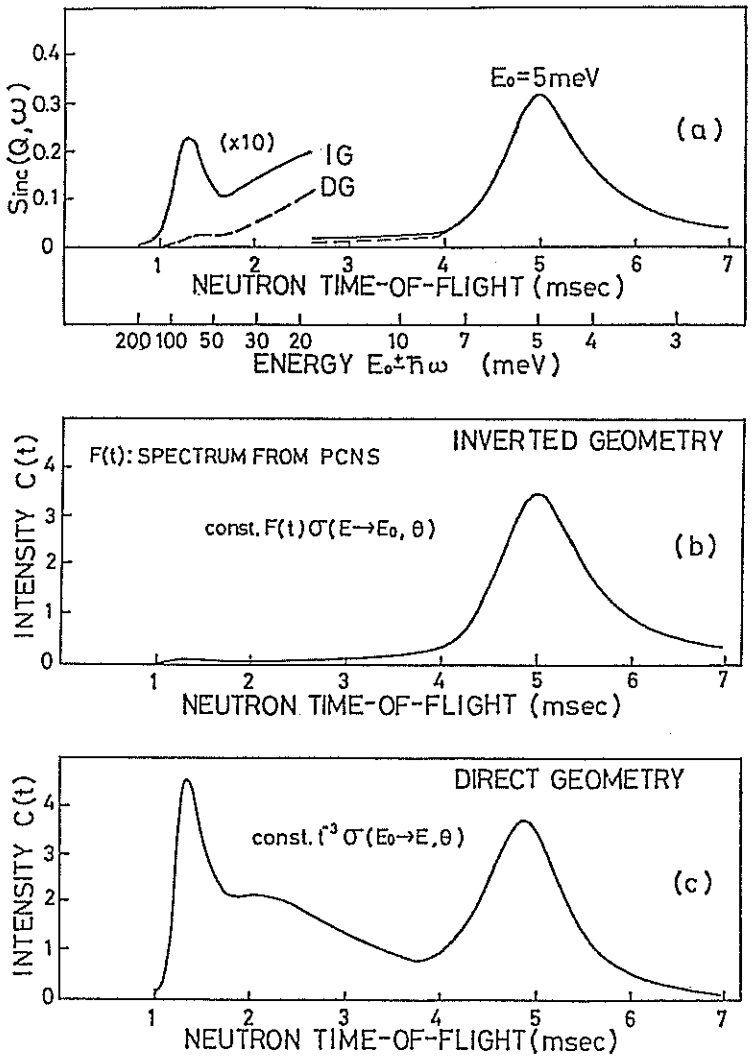
Eo=5meV
(x10)
IG
DG
(a)
Sinc(Q,ω)
NEUTRON TIME-OF-FLIGHT (msec)
ENERGY Eo±ħω (meV)
F(t): SPECTRUM FROM PCNS
INVERTED GEOMETRY
const. F(t)σ(E→Eo, θ)
(b)
INTENSITY C(t)
NEUTRON TIME-OF-FLIGHT (msec)
DIRECT GEOMETRY
const. t^3 σ(Eo→E, θ)
(c)
INTENSITY C(t)
NEUTRON TIME-OF-FLIGHT (msec)

Fig. 3

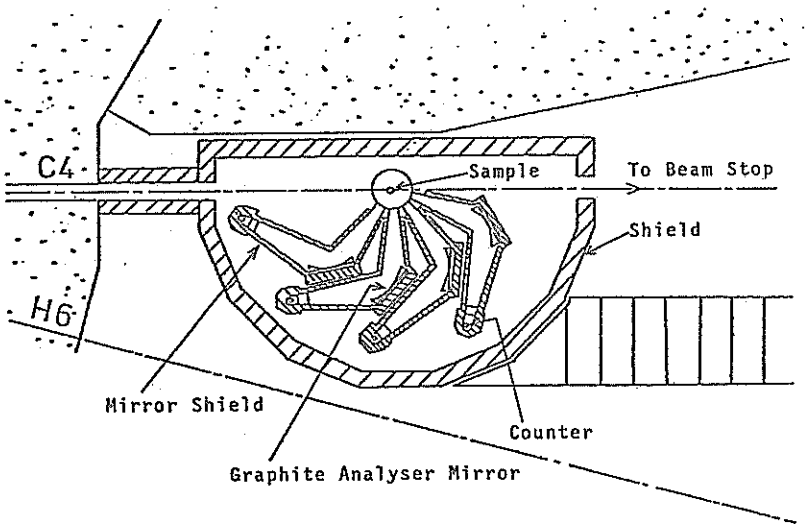
C4
Sample
To Beam Stop
Shield
H6
Mirror Shield
Counter
Graphite Analyser Mirror

Fig. 4

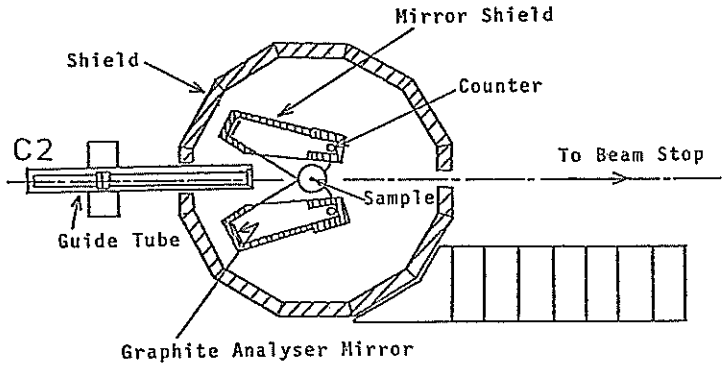
Mirror Shield
Shield
Counter
C2
To Beam Stop
Sample
Guide Tube
Graphite Analyser Mirror

Fig. 5

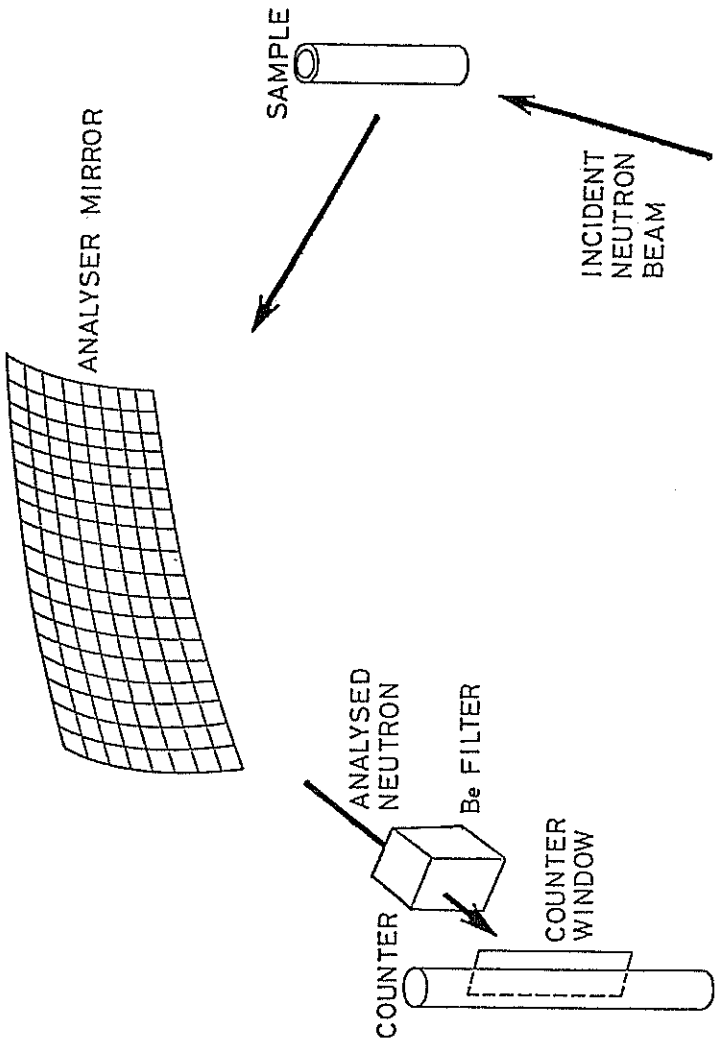
SAMPLE
INCIDENT NEUTRON BEAM
ANALYSER MIRROR
ANALYSED NEUTRON
Be FILTER
COUNTER WINDOW
COUNTER

Fig. 6

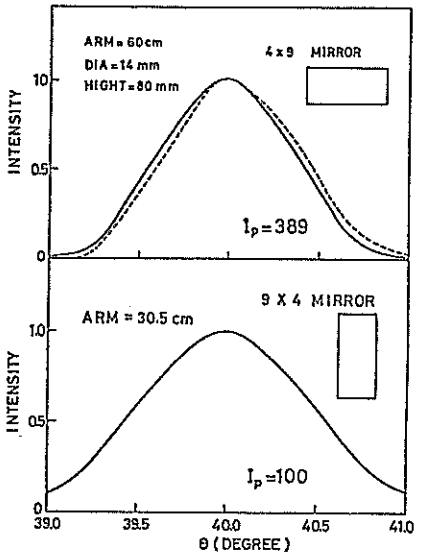
ARM = 60cm
DIA = 14 mm
HIGHT = 80 mm
4 x 9 MIRROR
INTENSITY
10
0.5
0
I_p = 389
9 X 4 MIRROR
ARM = 30.5 cm
1.0
0.5
0
I_p = 100
39.0
39.5
40.0
40.5
41.0
θ (DEGREE)

Fig. 7

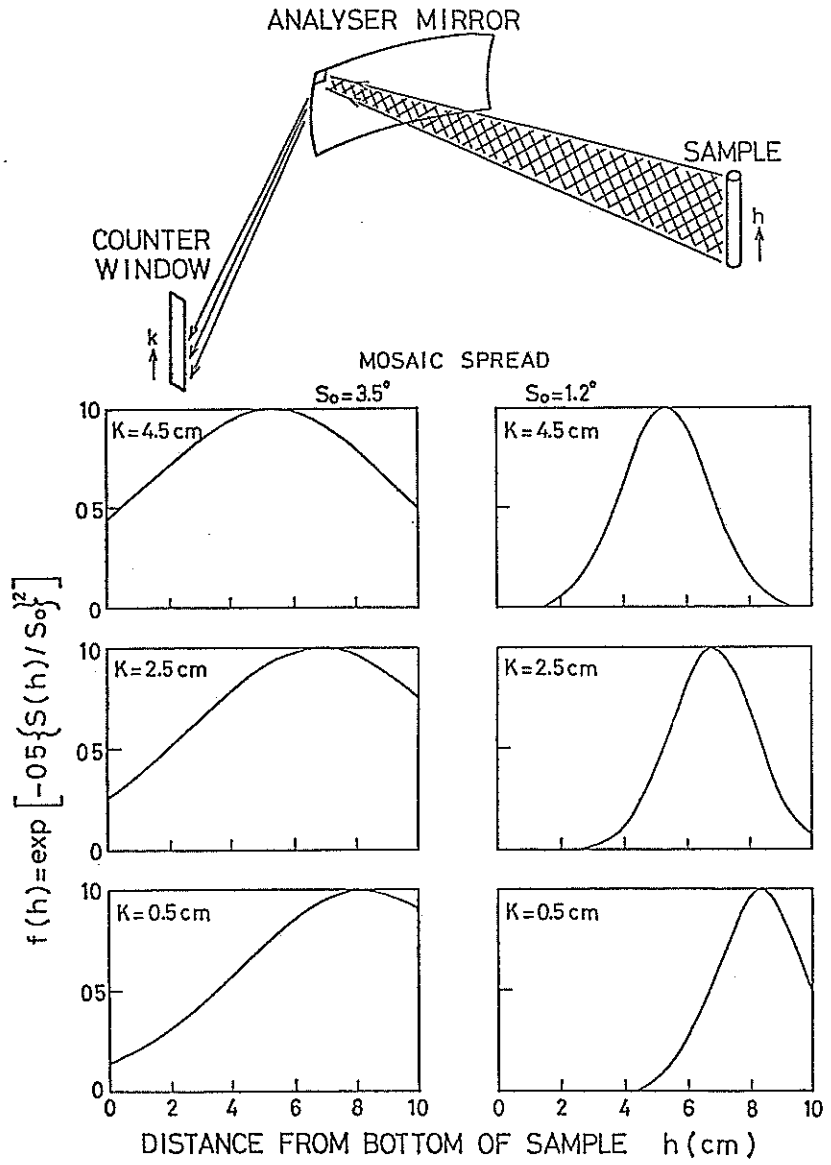
ANALYSER MIRROR
SAMPLE
COUNTER WINDOW
k
h
MOSAIC SPREAD
So=3.5°
So=1.2°
K=4.5 cm
K=2.5 cm
K=0.5 cm
f(h)=exp [-05{S(h)/So}^2]
DISTANCE FROM BOTTOM OF SAMPLE h (cm)

Fig. 8

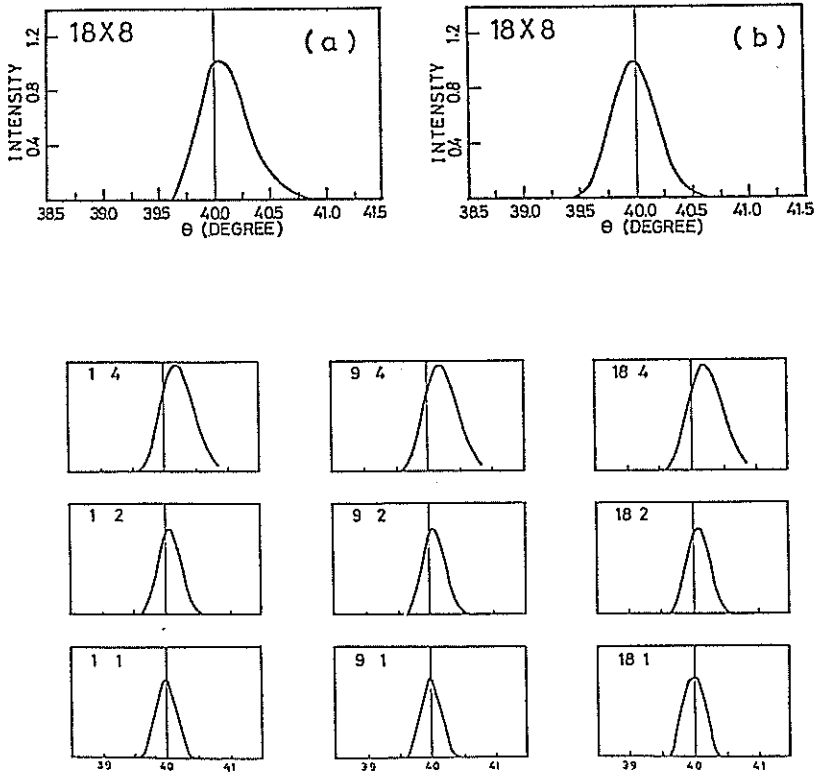
18X8
(a)
(b)
INTENSITY
θ (DEGREE)
1 4
9 4
18 4
1 2
9 2
18 2
1 1
9 1
18 1

Fig. 9

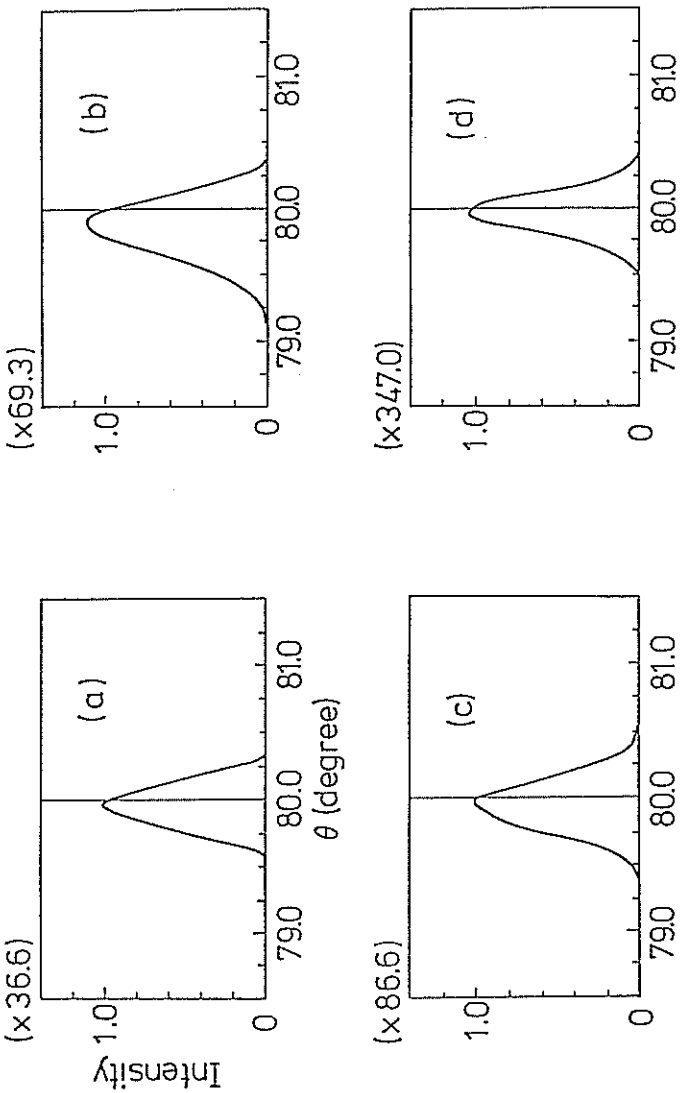
(b)
(d)
(a)
(c)
(x69.3)
(x347.0)
(x 36.6)
(x 86.6)
1.0
0
79.0
80.0
81.0
Intensity
θ (degree)

Fig. 10

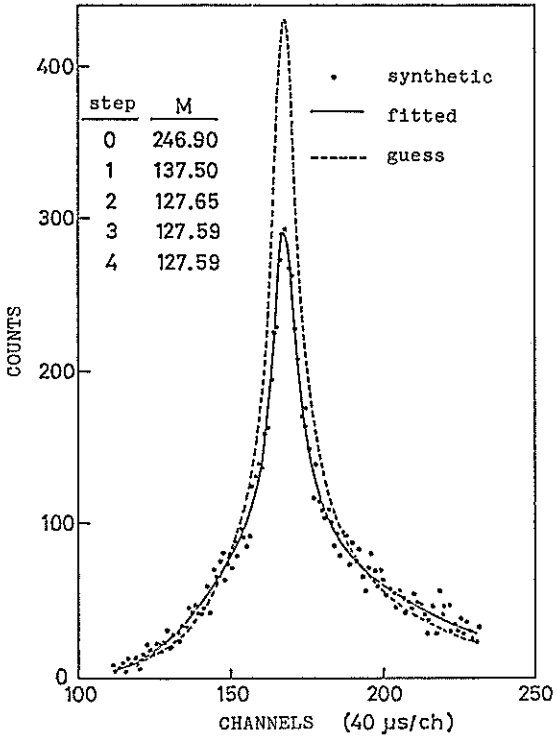
step
M
0 246.90
1 137.50
2 127.65
3 127.59
4 127.59
synthetic
fitted
guess
COUNTS
CHANNELS (40 μs/ch)
0
100
200
300
400
100
150
200
250

Fig. 11

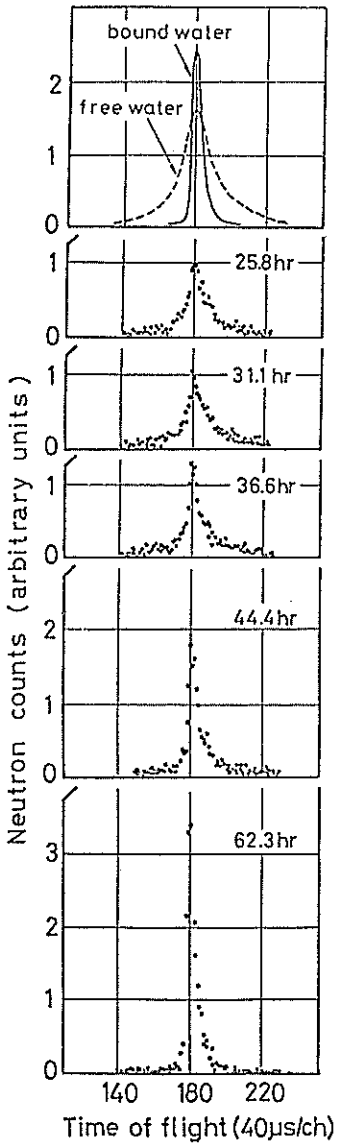
bound water
free water
25.8hr
31.1 hr
36.6hr
44.4hr
62.3hr
Neutron counts (arbitrary units)
140
180
220
Time of flight (40μs/ch)

Fig. 12

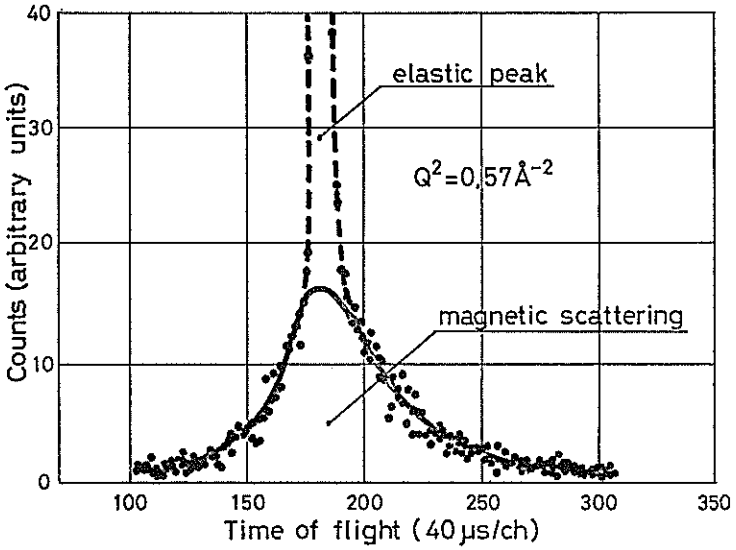
elastic peak
Q^2=0.57Å^{-2}
magnetic scattering
Counts (arbitrary units)
Time of flight (40μs/ch)

Fig. 13

4.5 Cold Polarized Neutron Spectrometer at KENS

Yasuo ENDOH and Yoshikazu ISHIKAWA

Department of Physics
Tohoku University, Sendai 980
Japan

§1. Introduction

In this report we introduce one of the projects using cold neutrons which will be transmitted through the guide tubes installed at the CH_4 cold moderator section. The sepctrometer named as TOP (TOF machine with Optical Polarizer) Spectrometer consists of a polarizer and a TOF machine. We are now at the status preparing a polarizing Soller mirror, designing spectrometer assembly, and testing a prototype magnetic channel to control neutron spins.

In the following section we will briefly explain the TOP spectrometer. We will also speak about the present status of the polarizer. Finally we will present a current research project of the surface magnetism which will be continuously investigated with this TOP spectrometer.

§2. TOP spectrometer

The TOP spectrometer will be located at the end of C3 guide tube in an experimental floor of "cold neutron wing". As mentioned in a preceding section, this machine consists of the polarizing mirror, the magnetic channel, a crystal table, polarization analysers and neutron detectors, which is illustrated in Fig.1. The machine control will be facilitated with a microprocessor which sits on a control panel near the machine. Neutron spectrum will be transferred to a medium size computer at the control room and data acquisition will be carried. Data will be processed in order to visualize as the crude data, for instance, as the diffraction patterns from samples. They will be transferred back to a display device on the control panel. A total system of the spectrometer is seen in Fig.2.

Let us explain the machine in more detail. Reflected neutrons by the curved magnetized Soller mirrors should be polarized with 100 % in principle due to the total reflection which depends on neutron spin direction. Thus, if the amplitude for the minus (antiparallel to the magnetic field) spin component is negative, all the reflected neutrons should be polarized. According to various conditions; for instance, the cutoff wave length is 4 Å, maximum length of mirror should be less than 40 cm and so forth, the curved Soller mirror must be designed such that the curvature is 2327 cm, each Soller is stacked by every 0.65 mm and 28 sheets are necessary to yield 20 mm wide beam. Principle of the polarizer structure as well as a prototype Soller polarizer are seen in Fig.3. As will be mentioned, we found that the magnetic field of 1000 Oe is enough to obtain sufficient polarization.[1] We designed an electromagnet which produces about 2000 Oe in a 50 mm gap with a current density of 6 A/mm^2.

We are now testing a prototype guide channel assembled permanent magnets, Helmholz coils as a flipper and a spin turner. We measured the field distribution in this channel, and found it reasonably working. Since all the neutron spins in a bunch of pulses must flip simultaneously, regardless the energy difference, we adopt the method of the nonadiabatic or adiabatic reversal for neutron spins. In the former cases of the nonadiabatic reversal, if the direction of the magnetic field is made to reverse in a very small distance, the neutron pass through this space with their spins unaltered. In other words, neutrons experience the reversal of the magnetic field in a short time compared to its Larmor precession period. Consequently neutron spin directs against the magnetic field direction in the reversal field. Flipping actions will be coincident with the period of the pulsed neutron burch so that the spin dependent scattering data are easily obtained. We designed an AC current generator of a stabilized power supply, which can produce either plus or minuns voltage with 20 Hz and also can control the timing. Fig.4 and 5 show these concepts.

The TOF machine has a heavy duty crystal table on which (maximum load ∿300 kg) an electromagnet ($\geq$ 12 koe) or a superconducting magnet with a temperature controlled cryostat can be loaded. Crystals can be set with three dimensional adjustment within accuracy of 0.01°. A bank of neutron detectors sits around the crystal table. Although the scattering angle can be changed freely, a symmetric set up with respect to the neutron path was designed in order to gain the scattering intensity. These detectors may cover the scattering length with the range between 0.02 Å and 1.5 Å. Standard resolution is set as 1° and therefore Soller collimators will be used for the counter at a small angle.

§3. Magnetized polarizing mirror

The magnetized polarizing mirror has been developed in Rutherford Laboratory;[2] and a similar type of the polarizer has also been prepared in our laboratories independently.[1] We made magnetized mirrors depositing FeCo alloys on myler films[3] by using a vacuum evaporation apparatus of the wet type. We will soon use a dry type apparatus which has a large chamber of 45 cm in diameter. Then we designed a device to apply a uniform tention necessary to obtain a flat surface like an ideal mirror. We obtained so far the following experimental condition for making thin films with adequate quality for the polarizer.

The effect of the various factors has been studied extensively;[1] such as tention, evaporation speed, the change of the glancing angle from an evaporating source to films, on the magnetization of FeCo thin films deposited on the myler films. Typical hysteresis curves are illustrated in Fig.6. We found, for instance, that the evaporation condition gives an anisotropy in magnetization, which is understood as so called the self shadow effect during the evaporation. Furthermore a large tensile force causes an appreciable decrease of the magnetization. However, when we apply the magnetic field of about 700 Oe, we notice that these effects may not be serious. Nevertheless we observed how the magnetic characters of thin films are modified during the synthesis of the polarizer.

We have been testing the quality of polarizer of these magnetic mirrors by the pulsed neutron facility at Laboratory of Nuclear Science, Tohoku University. We evaluated the reflectivity with respect to the function of wave length, postulating the reflectivity of the FeCo mirror evaporated on a float glass as perfect. In comparison to the calculation,

these observed results are interpreted by introducing the surface irregularity or the imperfect flatness as well as the decrease of the magnetization which was mentioned above.[1,4)]

We have also been testing their polarizability by using a polarized neutron spectrometer. At present, we obtained the preliminary results of the polarizability using polarized neutrons of 2.44 Å. Typical scans are shown in the following figure. We are now making new polarizers using OPP films as substrate, which gives a negative scattering amplitude.

§4. Interface magnetism[5)]

Recently considerable attention has been directed to the surface magnetism of mainly transition metals. The increase of numbers of studies on this problem using various techniques creates more and more controversies among their results. Therefore there should be desired a direct evidence that surface magnetization values change from the bulk values. We demonstrated that the neutron diffraction technique offers the potential tool to investigate these problems.[6)]

The idea is very simple that the neutron diffraction method for such films composed of the periodic stacking of bilayers with d Å in thickness will give a direct evidence for the interface magnetism. Bragg condition with respect to the scattering vector normal to the plane of films are given by

$$\lambda = 2d/m \sin\theta_B \ ,$$

In the case of bilayer films of the periodic stacking of magnetic components, the magnetic scattering potential superposes the nuclear scattering potential. Then the existence of either "dead" or "enhanced" interface magnetic layers brings a fine structure into the magnetic potential.

This pontential creates the difference of the form factor between the magnetic and the nuclear distributions along the direction normal to the surface. Since the scattered intensity depends sensitively on the distance of the magnetic layer as well as the magnetization, the spin dependent scattering power should give the direct evidence of the existence of the interface magnetization. Furthermore the interface irregularity and the smearing of bilayers give no serious effect on the difference of the form factor between nuclear and magnetic distribution.

Usually we can synthesize the bilayer crystals which consists of ∿50 bilayers with d ≃ 100 ∿ 200 Å in thickness. Therefore long and intense cold neutron sources should have a great potential for investigating these problems.

So far we have studied Fe-SiO and Ni-SiO bilayer crystals, and we could have an appreciable difference between the interface magnetization of Fe and Ni metals.[5)]

We are now proceeding to study the magnetization of FeCu or FePd bilayer crystals.

Acknowledgements

Technical development for making magnetic mirrors which will be used as the TOP polarizers has been achieved by a number of technical assistances. Authors are much obliged to Y. Honma, Y. Sasaki and M. Onodera for their invariable efforts. They are also indebted to H. Ishii of Toray Co. and to H. Ito of Mitsui Petrochemical Ind. for their kind advices and for supplying high quality polymers.

References

1) Y. Sasaki and Y. Endoh: Res. Rep. Lab. Nucl. Sci., Tohoku Univ. 12 (1979) 65 (in Japanese).

2) J.B. Hayter, J. Penford and W.G. Williams: J. Phys. E 11 (1978) 454 .

3) Y. Endoh: Progress Rep. on "Research for development of neutron polarization and its polarization analysis" edited by Y. Yamada (1977 April) 22 (in Japanese).

4) Y. Honma: Thesis for master degree of science Tohoku Univ. (1978 March) (in Japanese).

5) M. Sato, K. Abe, Y. Endoh and R.D. Lowde: J. Phys. C to appear

6) M. Sato, K. Abe, and Y. Endoh: J. de physique C2 supp. 3 (1979) 72.

Figure Cpations

Fig.1 Views of TOP spectrometer at C1 part on the experimental floor of "C.N. Wing".

Fig.2 Block diagram of TOP system.

Fig.3 Structure of the Sollare polarizer and its photograph.

Fig.4 Concepts on the nonadiabatic spin flipping.

Fig.5 Concepts on TOF polarized neutron spectroscopy.

Fig.6 Magnetization curve of $Fe_{25}Co_{75}$ thin film deposited on myler films. Film thickness, 1025 Å, X// direction along neutron beam tensile force was applied to the film perpendicular to X.

Fig.7 Polarization vs scattering angle (2θ). Measurements were carried with polarized beam of 2.44 Å wave length.

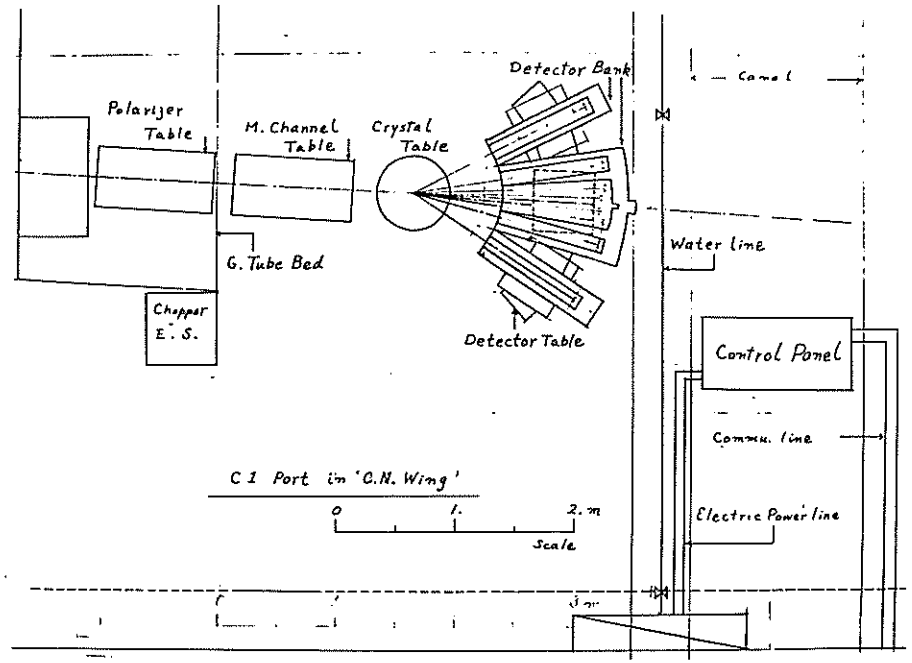

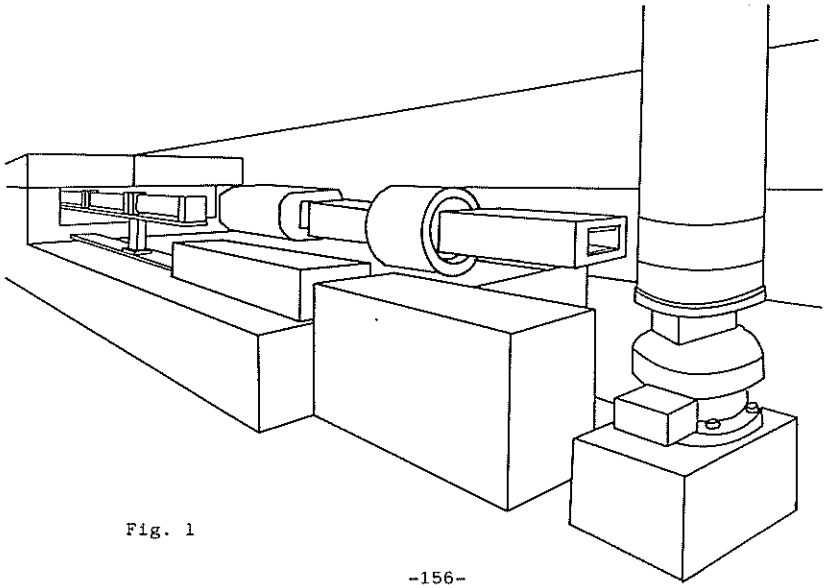

Fig. 1

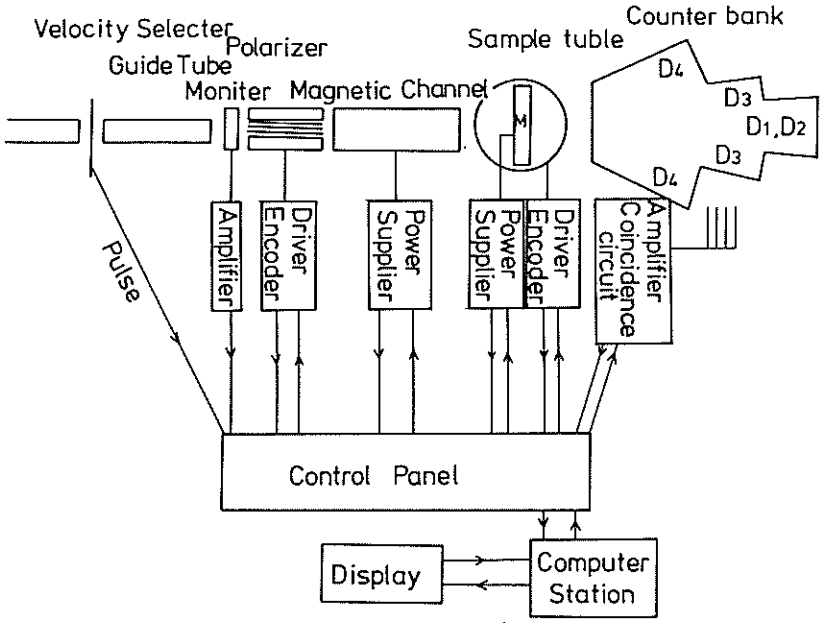
Velocity Selecter
Polarizer
Guide Tube
Moniter
Magnetic Channel
Sample tuble
Counter bank
D4
D3
D1,D2
D3
D4
M
Pulse
Amplifier
Driver Encoder
Power Supplier
Power Supplier
Driver Encoder
Amplifier Coincidence circuit
Control Panel
Display
Computer Station

Fig. 2

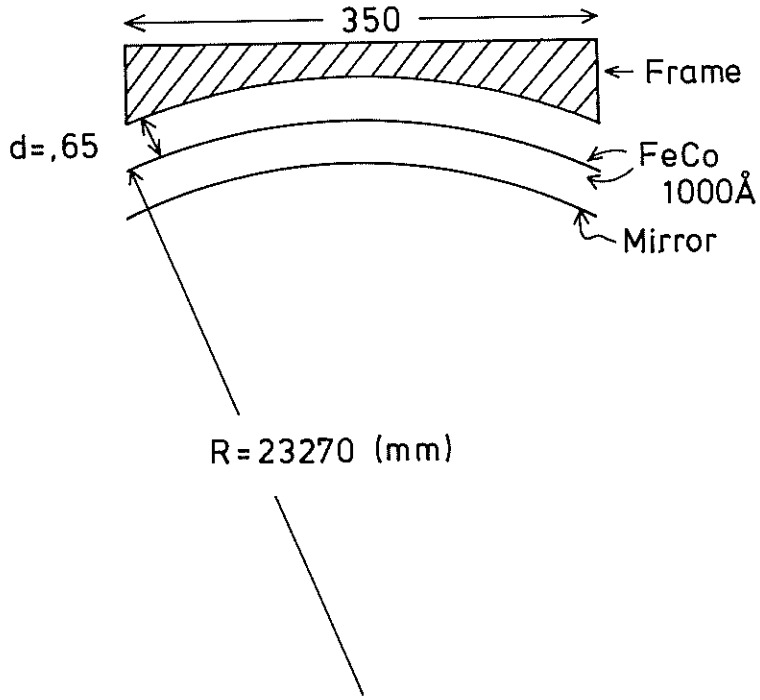
350
Frame
d=,65
FeCo
1000Å
Mirror
R=23270 (mm)

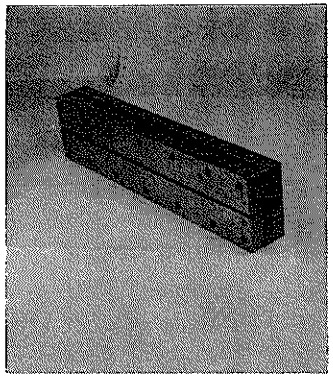

Fig. 3

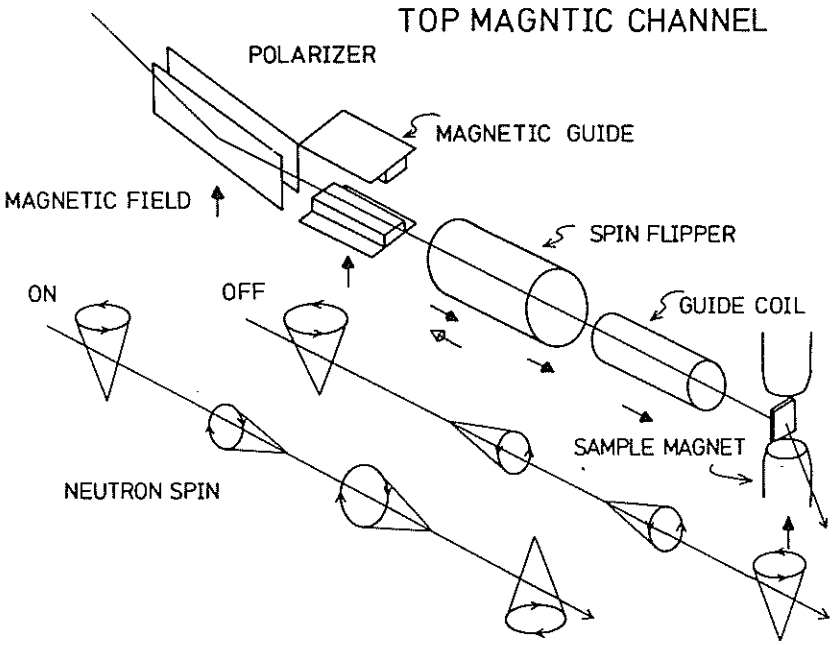
TOP MAGNTIC CHANNEL
POLARIZER
MAGNETIC GUIDE
MAGNETIC FIELD
SPIN FLIPPER
ON
OFF
GUIDE COIL
SAMPLE MAGNET
NEUTRON SPIN

Fig. 4

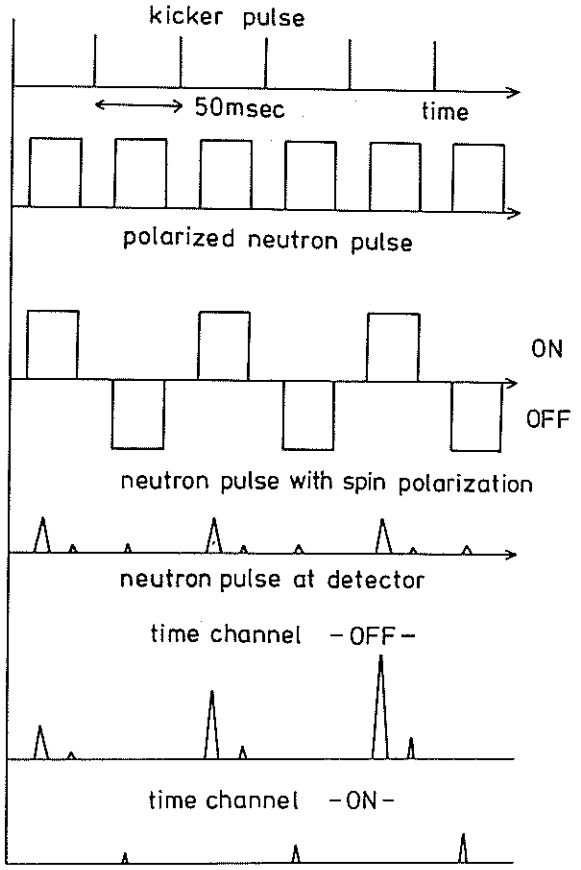
kicker pulse
50msec
time
polarized neutron pulse
ON
OFF
neutron pulse with spin polarization
neutron pulse at detector
time channel -OFF-
time channel -ON-

Fig. 5

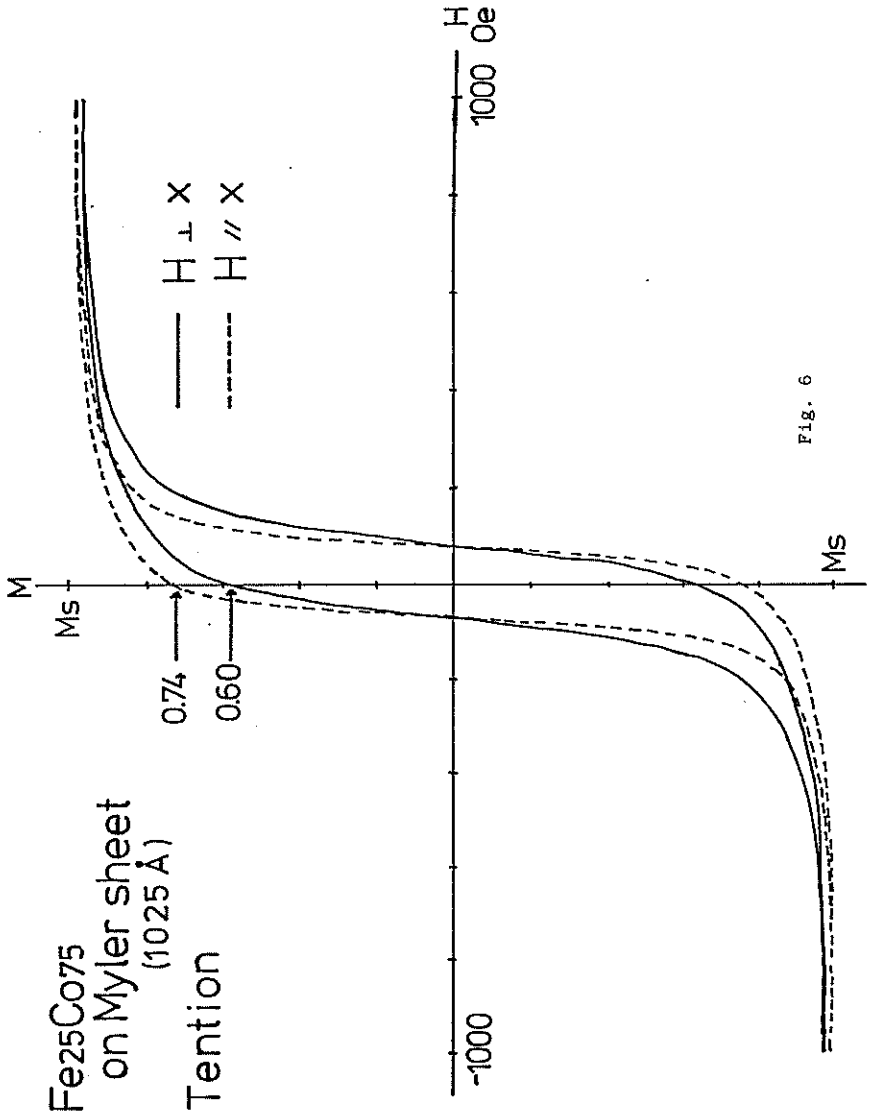
H
1000 Oe
H ⊥ X
H // X
M
Ms
Ms
0.74
0.60
-1000
Fe25Co75
on Myler sheet
(1025 Å)
Tention

Fig. 6

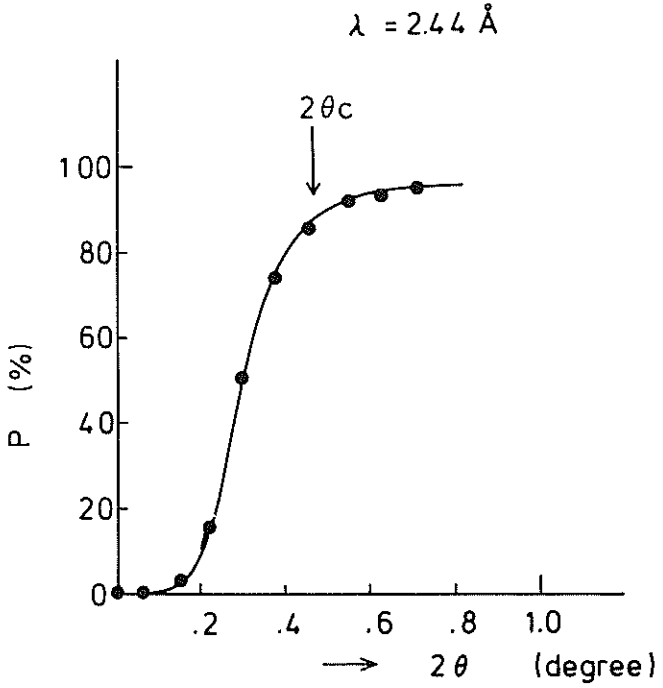
λ = 2.44 Å
2θc
100
80
60
40
20
0
P (%)
.2
.4
.6
.8
1.0
2θ (degree)

Fig. 7

5 KENS data acquisition system

N. Niimura*, M. Kohgi** and N. Watanabe*†

* Laboratory of Nuclear Science, Tohoku University
Mikamine 1-2, Sendai

** Physics Department, Faculty of Science
Tohoku University, Sendai

† Present address: National Laboratory for
High Energy Physics,
Oho-machi, Tsukuba-gun, Ibaraki

§1. General view of the system

The basic philosophy of the KENS data acquisition system is summarized as follows:

i) At present the installation of 5 spectrometers is scheduled.

They are MAX (Multi-Analyzer Crystal Spectrometers),
LAM (Low-energy Crystal Analyzer Spectrometer, or Large Analyzer Mirror),
TOP (TOF Machine with Optical Polarizer)
HIT (High Intensity Total Scattering Spectrometer), and
SAN (Small Angle Scattering Instruments).

The neutron scattering data from these spectrometers are stored and handled by a single medium scale computer. More than 10 spectrometers are expected to be installed in KENS in future. In such a case, large data acquisition system should be introduced, and the system should be expanded.

ii) Each spectrometer has a dedicated time analyzer and a control panel.

iii) CAMAC system is adopted for the interface.

The system configuration is shown in Fig. 1.

The specifications of each device are as follows:

i) CPU (Central Process Unit)

The computer is OKITAC-System 50/model 60. The main memory is 576 KB-IC and its cycle time is 600 nsec.

ii) MD (Magnetic Disc)

Memory size of the MD is 64 MB and its data transfer speed is 806 KB/sec. Main part of the MD is used for the

data storage. 128 KB memories are given to each spectrometer and more than 4 MB memories are given to SAN in the MD.

iii) MT (Magnetic Tape)

Each user has a personal magnetic tape and the final data should be transferred from the MD to his MT. This operation is carried out by a user himself. The frequency of this operation is not so much (It depends on the experiment.), since 128 KB memory size in the MD is given to each spectrometer. In order to avoid the overcrowded state of the operation, two MT control units are available. The memory size of the MT is about 10 MB (800 BPI, 1200 ft).

iv) ET (Electric Type-writer)

This is used for the simple conversation with the computer. The ET consists of a typewriter, a paper tape reader and a paper tape puncher. This might not be used for the output device of data.

v) DLP (Dotted Line Printer)

This is used for drawing of a figure with an aggregation of dots. This can be also used as a line printer.

vi) LP (Line Printer)

The printing speed is 313 lines per a minute.

vii) PTR (Photo-Tape Reader)

The reading speed is 30,000 characters per a minute.

viii) GD (Graphic Display) & HC (Hard Copy)

These are a storage graphic display and its hard copy connected to this GD. The size of a display surface is 381 mm in length and 279 mm in height.

§2. Time analyzer unit

There are three types of time analyzer units. These are called TA (Time analyzer), HTA (Time analyzer for high counting rate) and MDTA (Time analyzer for the multi-dimensional detectors) respectively.

i) TA

TA is a normal time analyzer unit which is used for the general sepctrometer. The block diagram of TA is shown in Fig. 2. The specifications are given as follows: 16 inputs can be accepted. One input connects with one bundle of detectors. The TA is synchronized with a booster trigger which defines the origin of the time of flight combined with the following delay time. The delay time is varied from 1 μsec to 49,999 μsec. A total channel number is selected amongst 512, 1024, 2048 and 4096. Channel width is selected separately in each quarter of the total channel number amongst 0.25, 1, 2, 3, 4, 6, 8, 12, 16, 24, 32, 48, 64, 96, 128, 192, 265, 384, 512, 768, 1024, 1536, 2048, 3072 and 4096 μsec. We call this system as an accordion method. An example showing the merit of the accordion method is as follows: We suppose that delay time is 128 μsec and the channel width of the 1st, 2nd, 3rd and 4th quarter is selected as 2 μsec, 8 μsec, 16 μsec and 32 μsec respectively. We can meausre the time of flight till 7552 μsec with the time resolution of about 1% by using only 512 words memory. The time resolution coming from channel width is shown in Fig. 3. The nearly constant time resolution is obtained in the whole region. If we try to realize this situation without an accordion method and a delay time, 3776-

words memory is necessary. For, the time resolution in such a case depends on the channel width of the small time of flight and this is 2 μsec. (3776=7552/2). The resolution of the range of the large time of flight becomes automatically much less than 1%. Such a good resolution is often unnecessary.

The add-one data are stored temporarily in the buffer memory (8 KW RAM) by a direct memory access. When all 16 inputs are connected, it takes 4 μsec to take in one datum into RAM.

ii) HTA

HTA is a time analyzer unit which is used for the high intensity total scattering spectrometer (HIT). The block diagram of the HTA is shown in Fig. 4. HTA consists of 8 units. One unit corresponds to one input, and has a 4-bits counter, the content of which is transferred to a register according to the 4 MH_z clock signal. Then the counter is re-set and starts to count again. Meanwhile the content of the register is added to the content of the buffer memory (1 KW RAM). The buffer memory is dedicated to one unit. Maximum counting rate is 16 cts/250 nsec in principle.

The selection of the total channel number and the delay time, and the accordion method are the same as the TA unit. But the selection of the channel width is limited to 1, 2, 3, 4, 6, 8, 12 and 16 μsec.

iii) MDTA

MDTA is a multi-dimensional time analyzer which is used for the small angle scattering instrument (SAN). 2-dimensional detector system in this instrument consists of

43 one-dimensional detectors. In the MDTA, the position where a neutron hits and the time when the neutron arrives at any detector are analyzed. The block diagram of MDTA is shown in Fig. 5. The position is determined by the following expression,

$$x \propto \frac{Q_A}{Q_A + Q_B} \qquad (1)$$

where Q_A and Q_B are the quantity of the charge generated at each end of a detector. A pre-amplifier is connected to either end of the detector. The pre-amplifier outputs Q_A and Q_B are taken to main amplifiers which amplify and shape the signals. The main amplifier outputs are summed and fed to a single channel analyzer (Discriminator). When the sum of Q_A and Q_B are within the pre-set limits, in the discriminator standard step signals are generated, which are used for the gate signals of the sample & holder (S & H), and an analogue to digital converter (ADC) and a time analyzer.

° Position

The outputs from the main amplifiers are taken to the S & H to adjust the timing to be fed to the ADC. Since the conversion speed of the ADC is fast (∿5 μsec), one ADC is used for handling the signals from 4 different detectors. Converted 8-bits data are transferred to the registers and the summation of Q_A and Q_B is carried out. As shown in Fig. 5, the elements to handle the signals from 4 detectors are packed in one circuit board. There are 11 circuit boards since there are 43 detectors. The multiplexer in the common controller on the other circuit board scans the registers on the 11

circuit boards sequentially (the scanning speed is 1 μsec/1 board). Then the value of Q_A, and $Q_A + Q_B$ are transferred to the address register of the P-ROM, in which positions calculated by the expression (1) are tabulated. Therefore, the operation time of the expresssion (1) is equal to the access time of P-ROM, that is, 1 μsec. Thus the position is defined.

° Detector number

First the number of the detector receiving a neutron is encoded to a 2 bits datum, and next the number of the circuit board, to which the detector belongs, is encoded to a 4 bits datum. Finally a datum of the detector number is given as a 6-bits datum.

° Time of flight

The discriminator outputs are used to determine the time of flight. The method is quite the same as TA. The total channel number is selected amongst 32, 64, and 128 and the delay time is varied from 0 to 50 msec with 0.1 msec step. The accordion method is applied and the channel width of each quarter section is selected amongst 24, 32, 48, 64, 128, 192, 256, 384, 512, 768, 1024, 1536, 2048, 3072, and 4096 μsec.

Finally the data of the position, the detector number, and the time of flight are synthesized to 18, 19 or 20 bits data. At present, 18 bits data are available because of the limit of the main memory capacity. The final data are taken through the digital in CAMAC module.

§3. Control Panel (CP)

Data aquisition and processing control are carried out

by using a control panel (CP). Each spectrometer has one CP. It consists of a count unit, a display unit and an output unit. The layout of the CP is shown in Fig. 6.

i) Count Unit

Start and stop of measurement are controlled here. Accumulation area indicates the memory area on the MD where the data are transferred. A data clear switch clears the data in the buffer memory and/or the accumulation area.

ii) Display Unit

Data in any accumulation area and buffer memory are displayed on the cathode ray tube (CRT). Edited data are stored in 1 KW RAM module in the CAMAC. CRT is controlled by a CRT controlled module in the CAMAC.

iii) Output Unit

An output device is selected by pushing the corresponding button. Output data in any accumulation area and buffer memory are selected with a switch named DETECTOR and a button named DISPLAY/OUTPUT AREA.

The intermission and the status of the switches and buttons in every unit are read through DI/DO module in the CAMAC.

§4. Flow of the Data and the control

i) TA and HTA

When a start button on the control panel (CP) is pushed, a LAM (look at me) signal is sent to a BD (branch driver) through a DI/DŌ module connected to the CP. Then the BD requests an intermission signal to a LAM grader (LG).

Then the LG sends a graded LAM to the CPU and the CPU understands the status of the intermission and orders the TA to start measurements. Neutron data are stored in buffer memory (8 KW RAM) in the TA by the direct memory access.

When a stop button on the CP is pushed, the measurement is stoped by the above mentioned sequence. The data stored in the buffer memory are transferred to the specified area in the MD. The flow of the data and the control are shown in Fig.7.

ii) MDTA

The flow of the control signal of the MDTA, that is, start and stop of measurement are the same as those of TA. Since the MDTA has not the buffer memory as the TA has, neutron data are also taken to the main memory with the same squence of other controle. It takes 10 μsec for one datum to be taken in from the MDTA to the main memory. The flow of the data and the control are shown in Fig. 8.

Figure Captions

Fig. 1 KENS data acquisition system.

Fig. 2 The block diagram of the normal time analyzer (TA).

Fig. 3 The time resolution of TA when the accordion method is adopted.

Fig. 4 The block diagram of the time analyzer for the high intensity spectrometer (HTA).

Fig. 5 The block diagram of the time analyzer for the multi-dimensional detectors (MDTA).

Fig. 6 The layout of the control panel.

Fig. 7 The flow of the data and the control for TA & HTA.

Fig. 8 The flow of the data and the control for MDTA.

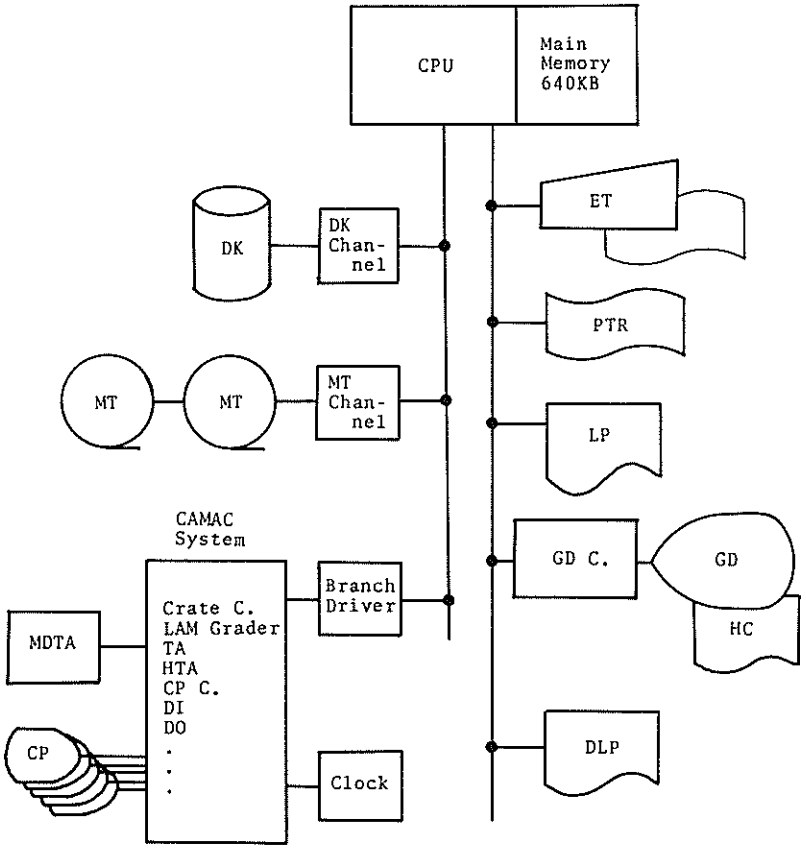
CPU
Main Memory 640KB
DK
DK Chan-nel
ET
PTR
MT
MT
MT Chan-nel
LP
CAMAC System
GD C.
GD
HC
MDTA
Crate C.
LAM Grader
TA
HTA
CP C.
DI
DO
Branch Driver
CP
Clock
DLP

Fig. 1

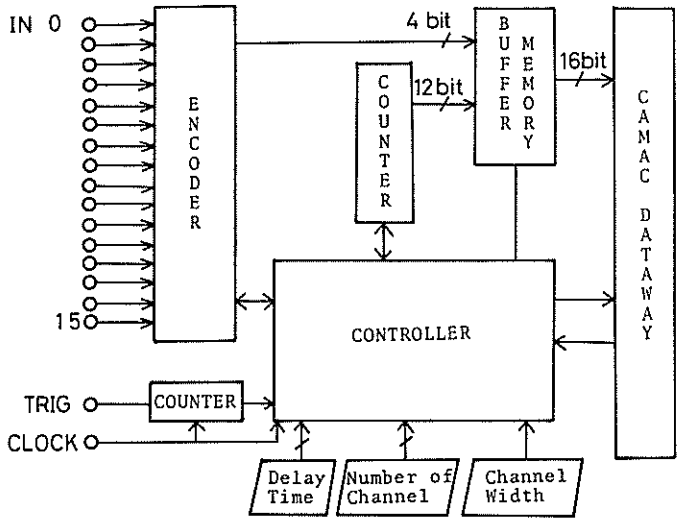
IN 0
15
ENCODER
4 bit
COUNTER
12bit
BUFFER MEMORY
16bit
CAMAC DATAWAY
CONTROLLER
TRIG
CLOCK
COUNTER
Delay Time
Number of Channel
Channel Width

Fig. 2

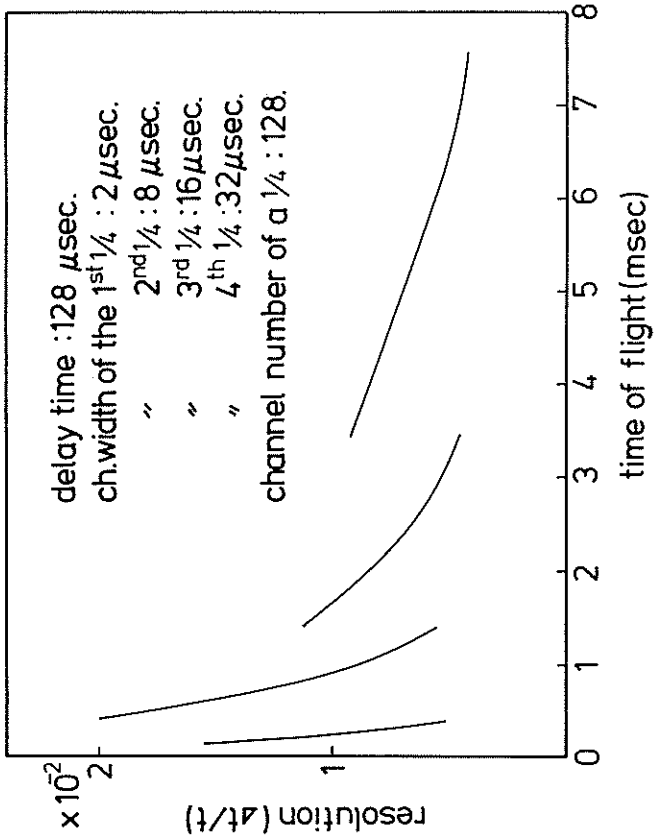

Fig. 3

KEK HIT Electronic System

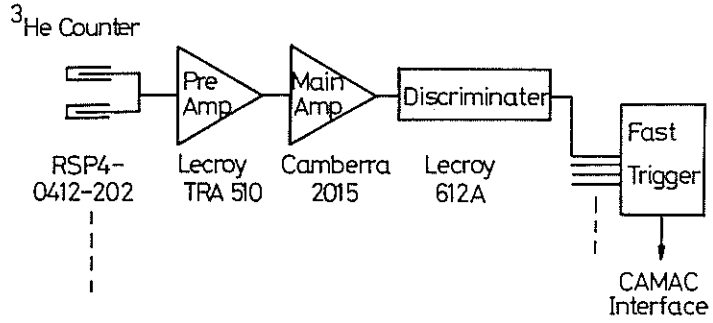

CAMAC Interface System

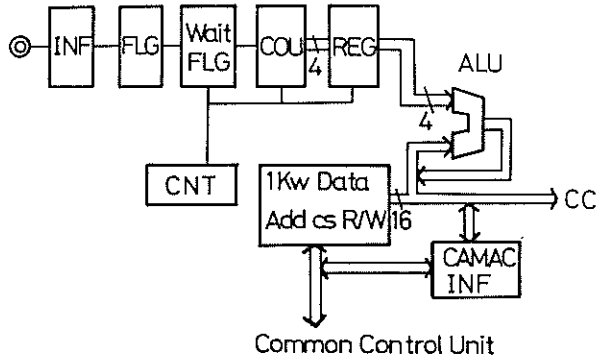

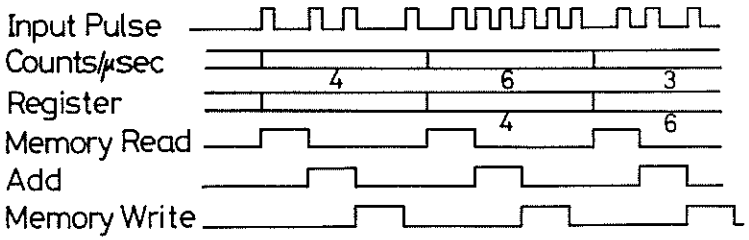

Fig. 4

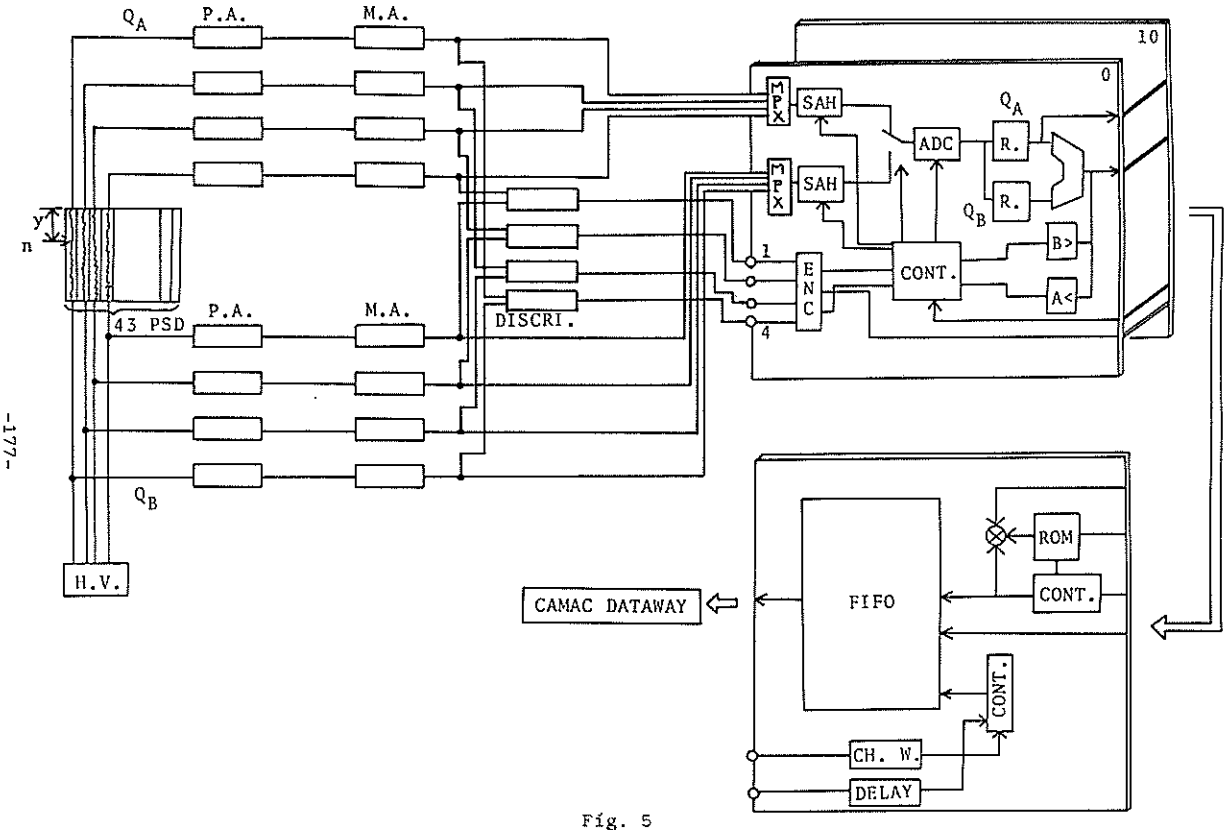
Q_A
P.A.
M.A.
y
n
43 PSD
P.A.
M.A.
DISCRI.
Q_B
H.V.
10
0
MPX
SAH
MPX
SAH
ADC
Q_A
R.
R.
Q_B
B>
A<
CONT.
1
4
ENC
CAMAC DATAWAY
FIFO
ROM
CONT.
CONT.
CH. W.
DELAY

Fig. 5

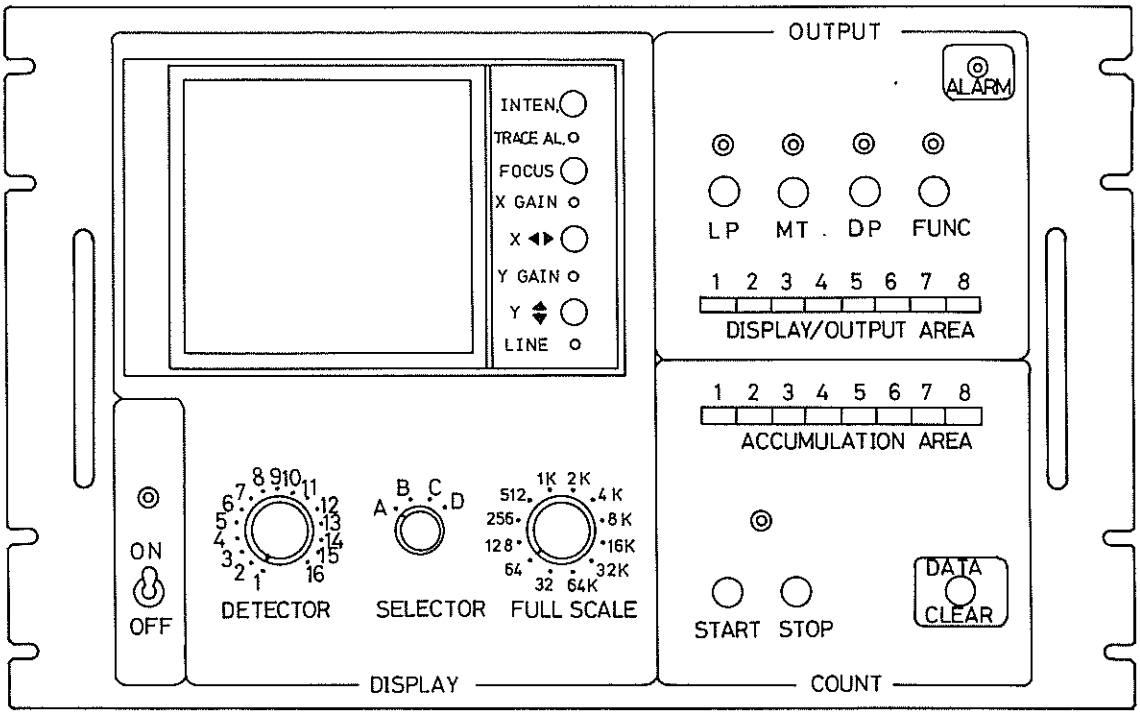
OUTPUT
ALARM
INTEN.
TRACE AL.
FOCUS
X GAIN
X
Y GAIN
Y
LINE
LP
MT
DP
FUNC
1 2 3 4 5 6 7 8
DISPLAY/OUTPUT AREA
1 2 3 4 5 6 7 8
ACCUMULATION AREA
ON
OFF
DETECTOR
SELECTOR
FULL SCALE
START
STOP
DATA
CLEAR
DISPLAY
COUNT

Fig. 6

FLOW OF CONTROL & DATA FOR TA & HTA

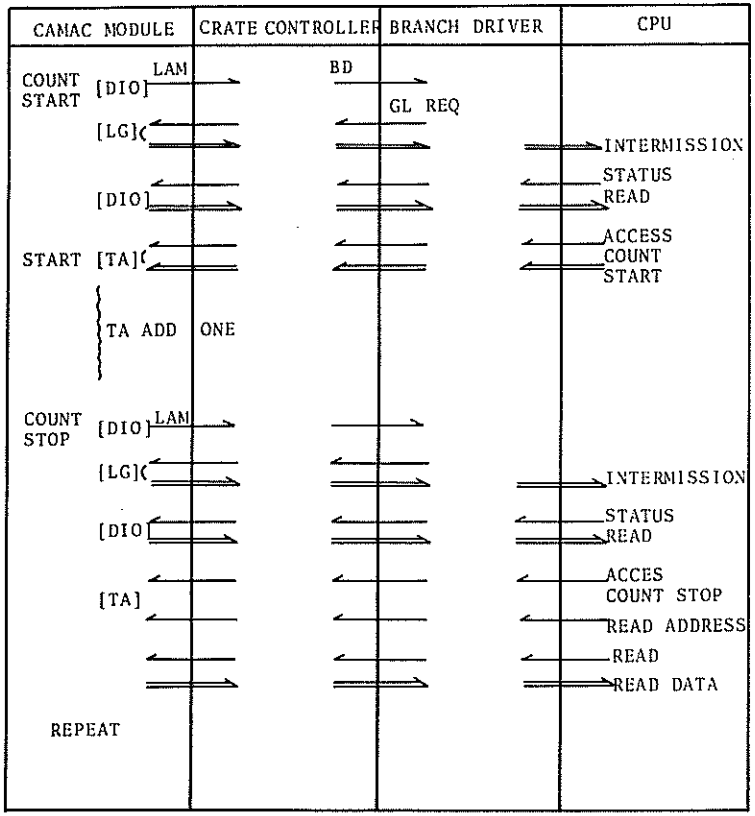

Fig. 7

FLOW OF CONTROL & DATA FOR MDTA

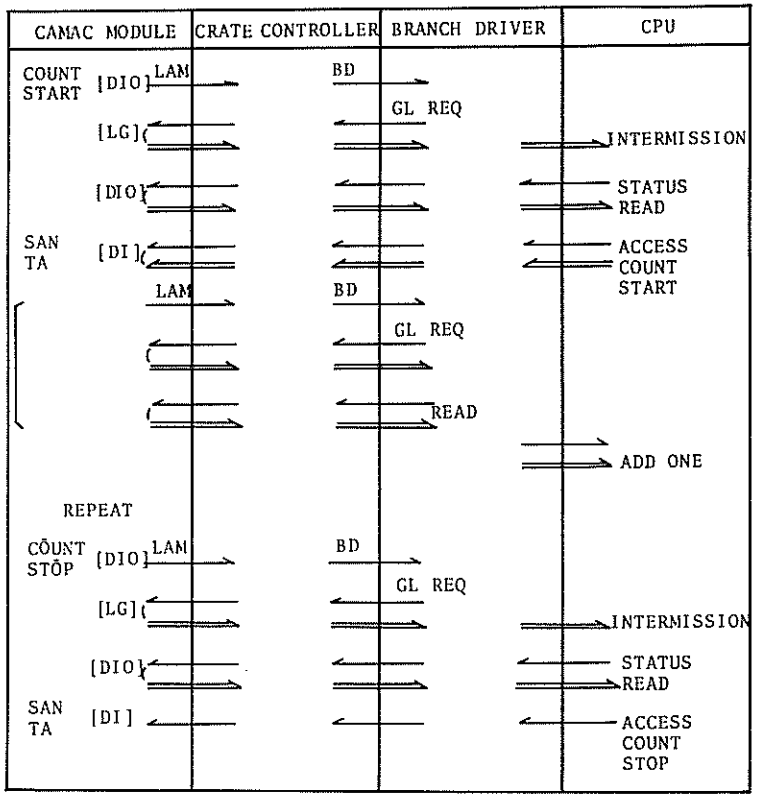

Fig. 8

6. Test experiments with pulsed neutron sources

6.1 A Time-Focussing Crystal Analyser and Measurement of Local Modes of TaH_x

Noboru Watanabe† and Michihiro Furusaka*
Laboratory of Nuclear Science and *Physics Department
Tohoku University, Sendai, Japan

Abstract

A high resolution energy loss spectrometer, designed to measure the incoherent neutron scattering at $\hbar\omega > 0.1$ eV, was constructed using time focussed crystal analyser and was installed at the pulsed neutron source at Tohoku linac. Local modes of the hydrogen motion in TaH_x system were measured at various temperatures with various hydrogen concentrations x. Energy resolution is fairly good which is 2.5 ∿ 4% in $\Delta\hbar\omega/\hbar\omega$ in the range of $\hbar\omega$=0.1 ∿ 0.6 eV and small changes in the peak position and the peak width of the local mode associated with the phase transition were observed.

Presented at ICANS Meeting, Rutherford Lab., 10-12 Sept. (1979)

† Present address: National Laboratory for High Energy Physics
Oho-machi, Tsukuba-gun, Ibaraki

1. Spectrometer[1)]

1.1. Time Focussing Crystal Analyser

Down scattering technique using the pulsed neutron source based on the pulsed accelerator is very useful for the incoherent neutron scattering at $\hbar\omega > 0.1$ eV.[2)] Crystal analyser method in the inverted geometry is very conventional where the sample is bathed in a white incident beam and the scattered neutrons at a selected energy E_s are detected by a crystal analyser. In case of the incoherent scattering, we can improve the counting efficiency by viewing the scattered neutrons over a large solid angle. Generally speaking the energy resolution becomes poor with increasing solid angle. Particularly it becomes very poor for large energy transfer, because uncertainty in time of flight for the incident neutrons increases due to the uncertainty of the correction in time of flight for scattered neutrons. In order to improve these situations, the time focussing method[3)] was adopted in the analyser system (sample-analyser crystal-detector). If we employ an equal flight path $L_2=L_3$ as shown in Fig. 1, we obtaine following time focussing condition,

$$\tan \alpha_S = \cot \theta_A,$$
$$\tan \alpha_D = \cot \theta_A,$$
$$\tan \alpha_A \to \infty,$$

that is

$$\alpha_S = \alpha_D = 90° - \theta_A,$$
$$\alpha_A = 90°.$$

This condition means that the sample, the analyser crystal and the detector are parallel with each other, and the net plane of the analyser crystal is also parallel to the analyser surface. The last condition makes it possible to use a pyrolitic graphite as an analyser which provides the good reflectivity.

Another important contribution to the energy resolution comes from the uncertainty in the incident flight path, and which is minimized by setting the sample and the moderator perpendicular to the incident beam.

Figure 2 shows the plan of the spectrometer. The incident flight path is 5.874 m in length and the neutron beam 7 cm wide and 10 cm high is extracted. The sample is usually packed in an aluminum container having dimensions of 8.5 cm × 11 cm with a thickness corresponding to about 10% scattering, and is put perpendicularly to the incident beam. The scattering apparatus has an enough space around the sample to accept a cryostat or a furnace. Scattered neutrons of energy 4 meV are selected using an analyser 10 cm wide, 10 cm high and 0.5 cm thick of pyrolitic graphite with 3.5° mosaic spread. The analyser is set parallel to the sample and the (002) reflection is used with Bragg angle $2\theta_A = 85°$. To eliminate higher order reflections, a cooled beryllium filter 11 cm in diam. and 15 cm in length, as shown in Fig. 3, is inserted between the analyser and the detector followed by a square grid collimator 5 cm in length with a 2.5 cm by 2.5 cm spacing. The measured transmission of the beryllium filter cooled down to 77 K was 83% for 4 meV neutrons, while that for

thermal neutrons corresponding to the higher order reflections were reduced to be less than one thousandth by the aid of the grid collimator. Four helium-3 proportional counters 1" diam. and 6" in active length filled to 760 cm Hg were aligned parallel to the analyser to detect the scattered neutrons. (Replacement of the present counters to 1/2" diam. ones filled to lower pressure is under way. This will improve the energy resolution due to the ambiguity in the scattered flight path length as well as signal to background ratio.)

1.2. Performance

In Fig. 4 are shown the calculated values of the energy resolution as a function of the energy transfer. Upper thick solid curve represents the overall resolution for the present apparatus with 1" diam. counters and 8 μsec time channel. The resolution is better than the reported values by Pan et al.[4], with a Be-BeO difference method, which varies from about ±4% at $\hbar\omega$=0.1 eV to ±8% at 0.5 eV, and also than the figure quoted by Day et al.[5] by means of a crystal analyser. Main reason of the advantage in the energy resolution of the present spectrometer compared to the latter is considered to be due to the longer incident flight path with smaller uncertainty in it because the sample is set perpendicular to the incident beam. Lower four solid curves show the partial contributions due to the uncertainty in the scattered flight path (Δt_3), the finite channel width of the time analyser (Δt_c), uncertainty in time of flight originating from the pulse width of the neutron source $[(\Delta t_p)^2+(\Delta t_m)^2]^{1/2}$, and

the finite energy band of the detected neutrons (ΔE_s). The contribution due to Δt_3 is significant which comes from the finite diameter of the detector, and therefore the thinner detector is preferable. Overall resolution for the 1/2" diam. detector with 4 μsec time channel is also depicted by a dot-dashed curve in the figure for the future improvements.

To examine the performance of the present spectrometer, the local mode of the hydrogen motion in a polycrystalline sample of TiH_2 at room temperature was measured. The result obtained with measuring time of 1 day is shown in Fig. 5 where the coordinate is the differential cross section multiplied by k/k'. The local mode is clearly observed up to the third level and it is very interesting to find that the first peak is splitting as seen in an enlarged energy spectrum in the inset. Similar fine structures have been observed in ZrH_x using a high resolution rotating crystal spectrometer and have been interpreted to be attributed to the hydrogen-hydrogen interaction.[6] The present results demonstrate a higher resolution of this spectrometer.

2. Local Modes of Tantalum hydrides[7]

One phonon spectra of the local modes of four polycrystalline samples of TaH_x with hydrogen-to-tantalum ratio x of 0.15, 0.50, 0.60 and 0.69 have been measured at various temperatures using the present spectrometer. The method to prepare tantalum hydrides was similar to that of vanadium deuterides which has been described elsewhere.[8] The hydrogen contents were

determined by the known relation between x and the lattice parameters which were determined by X-ray power diffractometry. The crystal structure of TaH_x is shown in Fig. 6 and a phase diagram has been proposed[9], which is shown in Fig. 7, where the measured points are also plotted.

In Fig. 8 is shown a typical TOF spectrum of $TaH_{0.5}$ at room temperature obtained with measuring time of 1 day, where clearly separated two peaks of the local mode are observed. An early data[10] obtained by a simple inverted BeO filter method is also shown in the inset to the figure for comparison.

The raw TOF data have been converted to double differential cross sections with normalizations by the incident spectrum after the subtraction of background obtained by an empty holder run, subtraction of the leakage spectra due to the higher order reflections, and corrections for absorption. The leakage spectra have been confirmed to be very small in case of hydrogenous sample. The distribution functions of frequencies $g(\hbar\omega)$ were, then, obtained from double differential cross sections by the method mentioned in the reference 10. $g(\hbar\omega)$ were fitted by two Gaussian or by two Lorentzian with a multiple scattering contribution properly assumed as shown in Fig. 9. From the figure, it is apparent that the Lorentzian fitting is clearly superior to the Gaussian. Since energy resolution width of the present spectrometer is very much better than the natural width of the optical peaks, it can be concluded that the peak shape is a Lorentzian, in

contrast to the early data which were like Gaussian because of the limited energy resolution of the instrument. The result provides the first clear experimental evidence for the shape of the optical peaks of this kind of metalic hydrides. The result also suggests that the dispersion of the local mode is very small; less than the half width of the Lorentzian, and therefore we can estimate the phonon lifetime from the half width.

In Fig. 10 are shown $g(\hbar\omega)$ for $TaH_{0.69}$ at various temperature with Lorentzian fitting. The variation in peak width as well as in the energy of peak center with temperature is apparent in the figure.

Center energies and widths of the optical peaks for all samples are plotted in Fig. 11 against temperature, where open symbols are for the optical peaks at about 120 meV and solid ones are for that at about 170 meV. Widths for lower energy peaks are almost-independent of x and lie on a line which increase slightly with temperature, exhibiting typical weak unharmonicity, while thosefor higher energy peaks jump drastically at temperatures of order-disorder transition. Similar jumps have been observed in the temperature dependence of the electrical resistivity of $TaH_{0.5}$ [9]. If we assume that the lower energy peak corresponds to the local vibration of hydrogen atom in the z direction and higher one to that in the xy directions, the results suggest the existence of an anisotropy in hydrogen motion across order-disorder phase transition, which is very interesting in relation to the anisotropy in the

hydrogen diffusion in this type of metal hydrides.

Energies of the peak center for both levels are independent of hydrogen concentration x below 0.5, and almost unchanged with temperature, while those for x above 0.5 exhibit a jump and strong concentration dependence below transition temperature. This variation may be partly interpreted by hydrogen configuration, but the true reason is not still apparent.

Measurements of the local modes of TaH_x at low temperature are in progress.

References

1) N. Watanabe, M. Furusaka and M. Misawa, Research Rep't. Lab. Nucl. Sci., Tohoku Univ. 12 (1979) 72 (in Japanese).

2) F. J. Webb, Harwell Report AERE-R4263 (1965).

3) A. Holas, Nucleonika 13 (1968) 871.

4) S.S. Pan, F.J. Webb and M.L. Yeater, Nucl. Instrum. Methods 42 (1966) 197.

5) D.H. Day and R.N. Sinclair, U.K. AEA Research Group Report AERE-R6717 (1971).

6) G.J. Couch, O.K. Harling and L.C. Clune, Phys. Rev. B4 (1971) 2675.

7) M. Furusaka, N. Watanabe and H. Asano, Research Rep't. Lab. Nucl. Sci., Tohoku Univ. 12 (1979) 83 (in Japanese).

8) H. Asano and M. Hirabayashi, Phys. Status solidi (a) 15 (1973) 267.

9) H. Asano, R. Yamada and M. Hirabayashi, Trans. JIM 18 (1977) 155.

10) R. Yamada, N. Watanabe, K. Sato, H. Asano and M. Hirabayashi, J. Phys. Soc. Jpn. 41 (1976) 85.

11) T.G. Berlincourt and P.W. Bickel, Phys. Rev. B2 (1970) 4838.

Figure Captions

Fig. 1. Time focussing condition for L_2=L_3 analyser.

Fig. 2. Schematic diagram of the spectrometer.

Fig. 3. Cooled Be filter for higher order rejection.

Fig. 4. Calculated values of the energy resolution $\Delta E/E$.

Fig. 5. Energy spectrum of the local mode from TiH_2 at room temp. Coordinate shows (differential cross section) $\times(k/k')$, the insert shows first peak enlarged in abscissa.

Fig. 6. Structure of TaH.

Fig. 7. Phase diagram of TaH, measured points are shown by ●.

Fig. 8. TOF spectrum of $TaH_{0.5}$ at room temp. The insert shows a data obtained by a inverted BeO filter method.

Fig. 9. Fitting of $g(\hbar\omega)$ for $TaH_{0.69}$: (a) Gaussian, (b) Lorentzian.

Fig. 10. Frequency distributions $g(\hbar\omega)$ of the local mode of $TaH_{0.69}$ at various temperatures.

Fig. 11. Temperature dependence of the peek energy and the peak width in FWHM of the local mode for various hydrogen concentrations x. Open symbols are for the peaks at about 120 meV and solid ones are for those at about 170 meV. Broken lines are for eyes only.

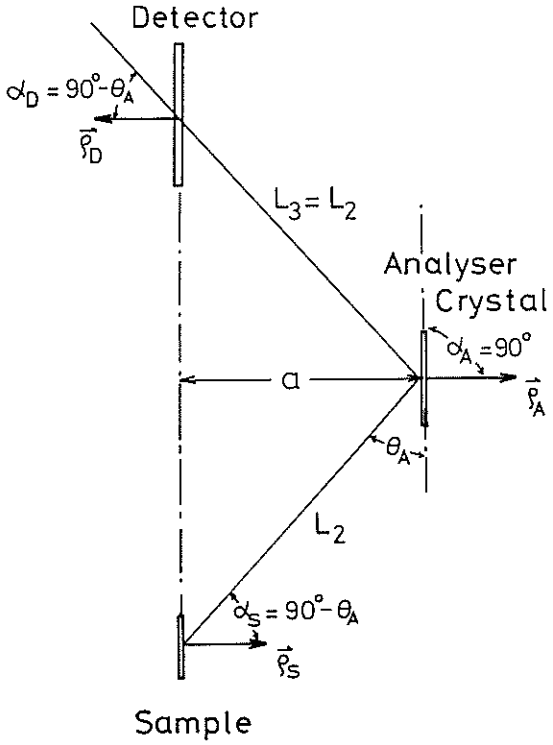
Detector
$\alpha_D = 90° - \theta_A$
$\vec{\rho}_D$
$L_3 = L_2$
Analyser
Crystal
$\alpha_A = 90°$
a
$\vec{\rho}_A$
θ_A
L_2
$\alpha_S = 90° - \theta_A$
$\vec{\rho}_S$
Sample

Fig. 1

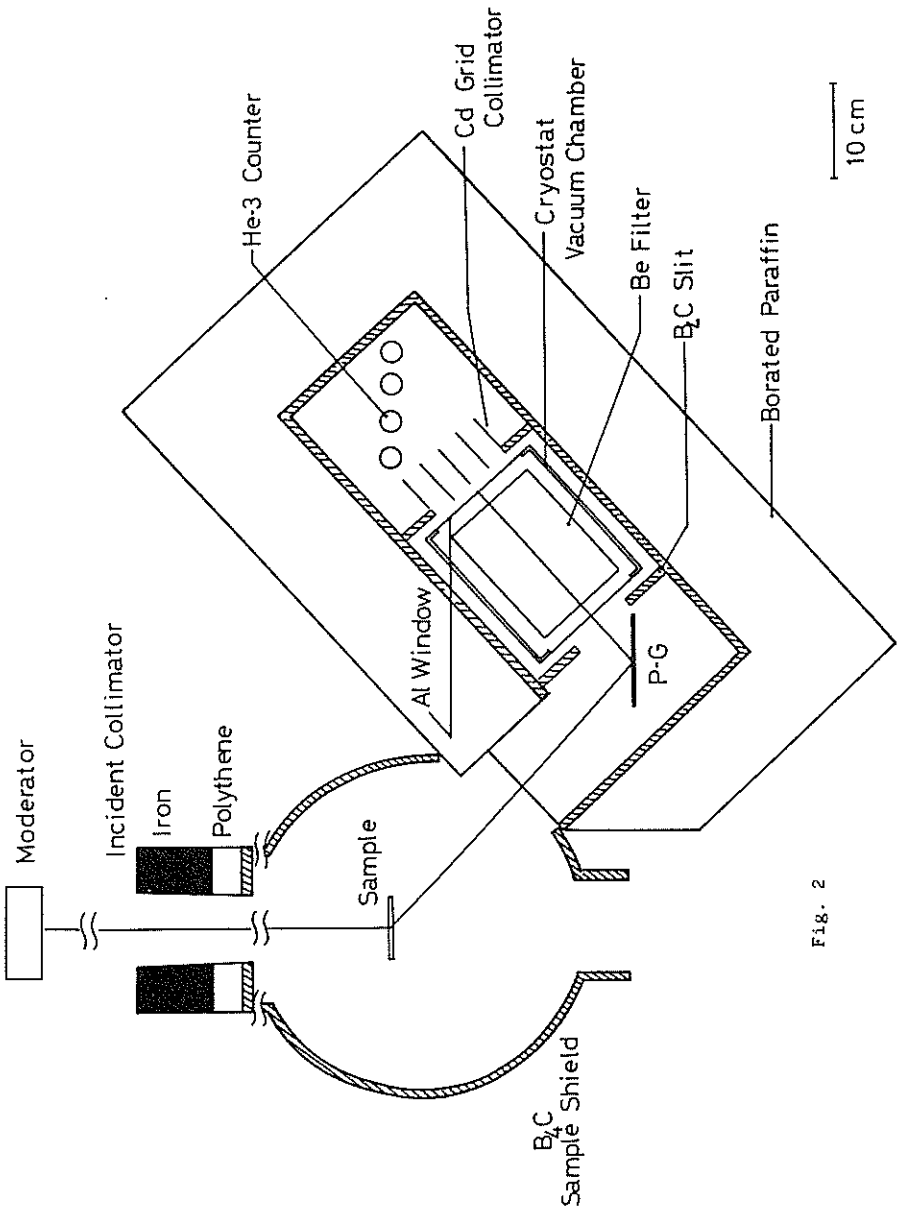
He-3 Counter
Cd Grid
Collimator
Cryostat
Vacuum Chamber
Be Filter
B_2C Slit
Borated Paraffin
10 cm
Al Window
P-G
Moderator
Incident Collimator
Iron
Polythene
Sample
B_4C
Sample Shield

Fig. 2

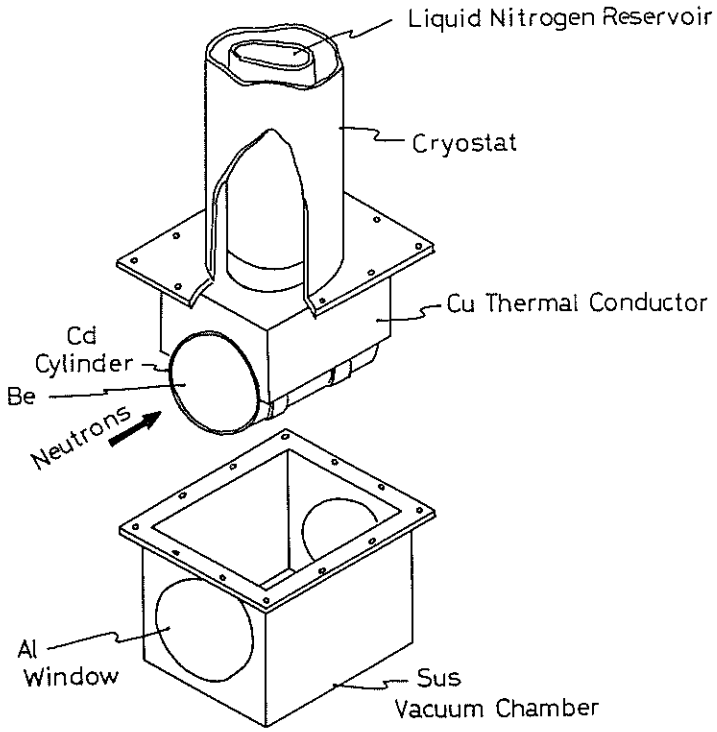
Liquid Nitrogen Reservoir
Cryostat
Cu Thermal Conductor
Cd
Cylinder
Be
Neutrons
Al
Window
Sus
Vacuum Chamber

Fig. 3

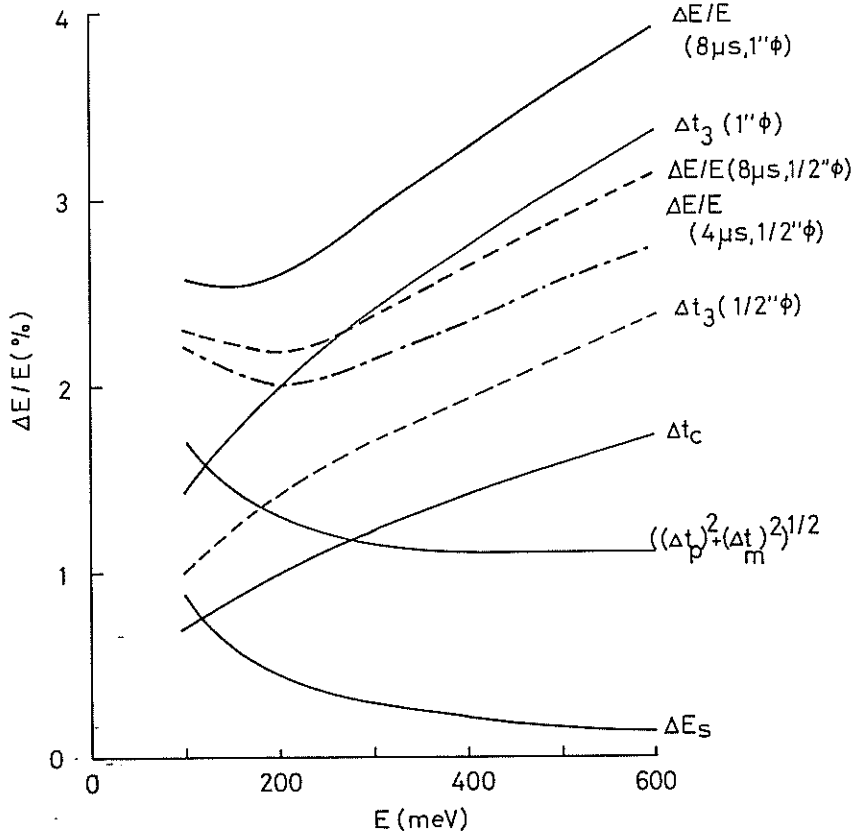
ΔE/E
(8μs,1"φ)
Δt3 (1"φ)
ΔE/E(8μs,1/2"φ)
ΔE/E
(4μs,1/2"φ)
Δt3(1/2"φ)
Δtc
((Δtp)2+(Δtm)2)1/2
ΔEs
ΔE/E(%)
E (meV)
0
1
2
3
4
0
200
400
600

Fig. 4

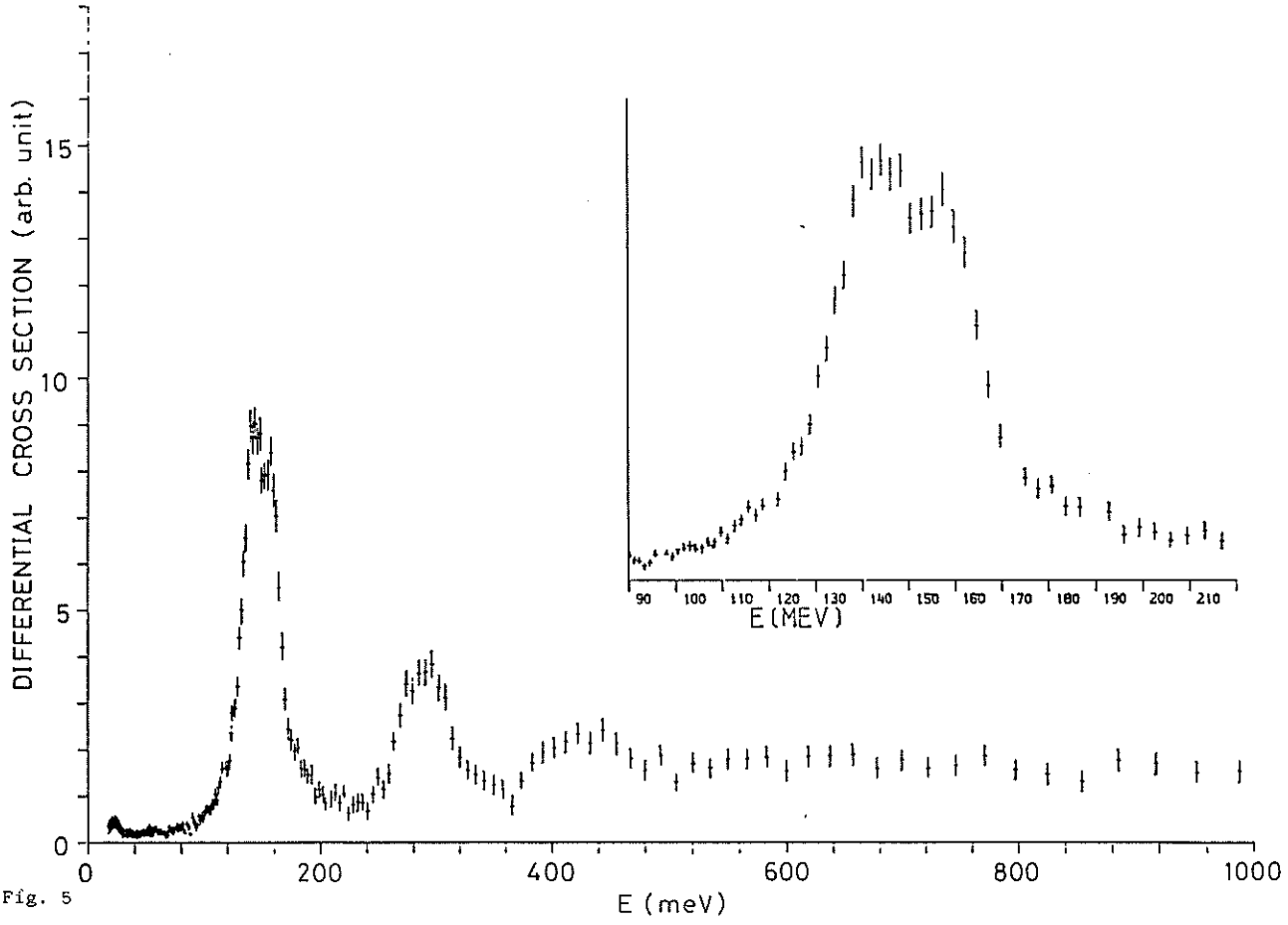
DIFFERENTIAL CROSS SECTION (arb. unit)
0
5
10
15
0
200
400
600
800
1000
E (meV)
90
100
110
120
130
140
150
160
170
180
190
200
210
E (MEV)

Fig. 5

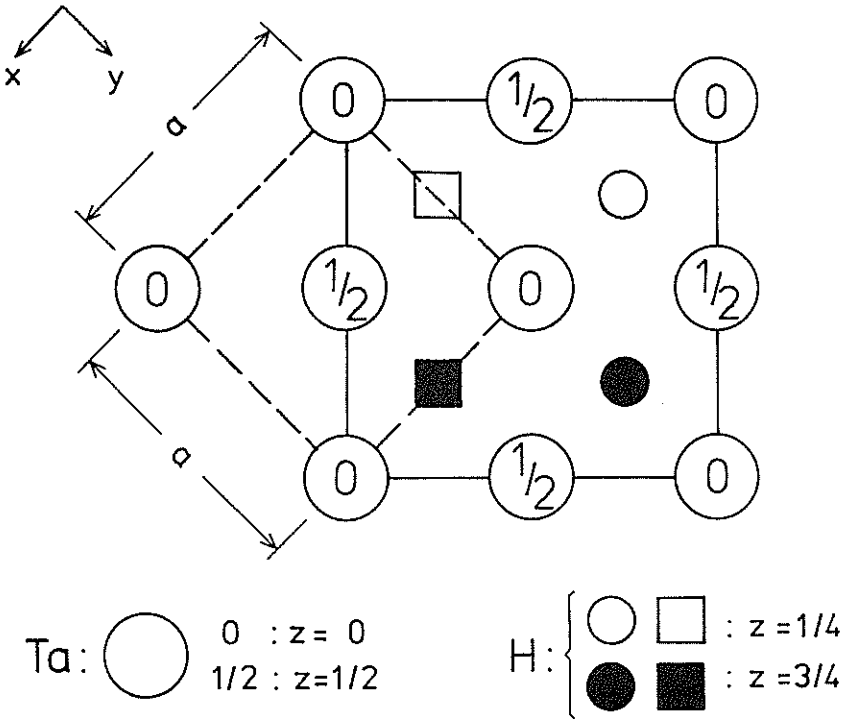
x
y
a
a
0
1/2
0
0
1/2
0
0
1/2
0
Ta:
0 : z= 0
1/2 : z=1/2
H:
: z =1/4
: z =3/4

Fig. 6

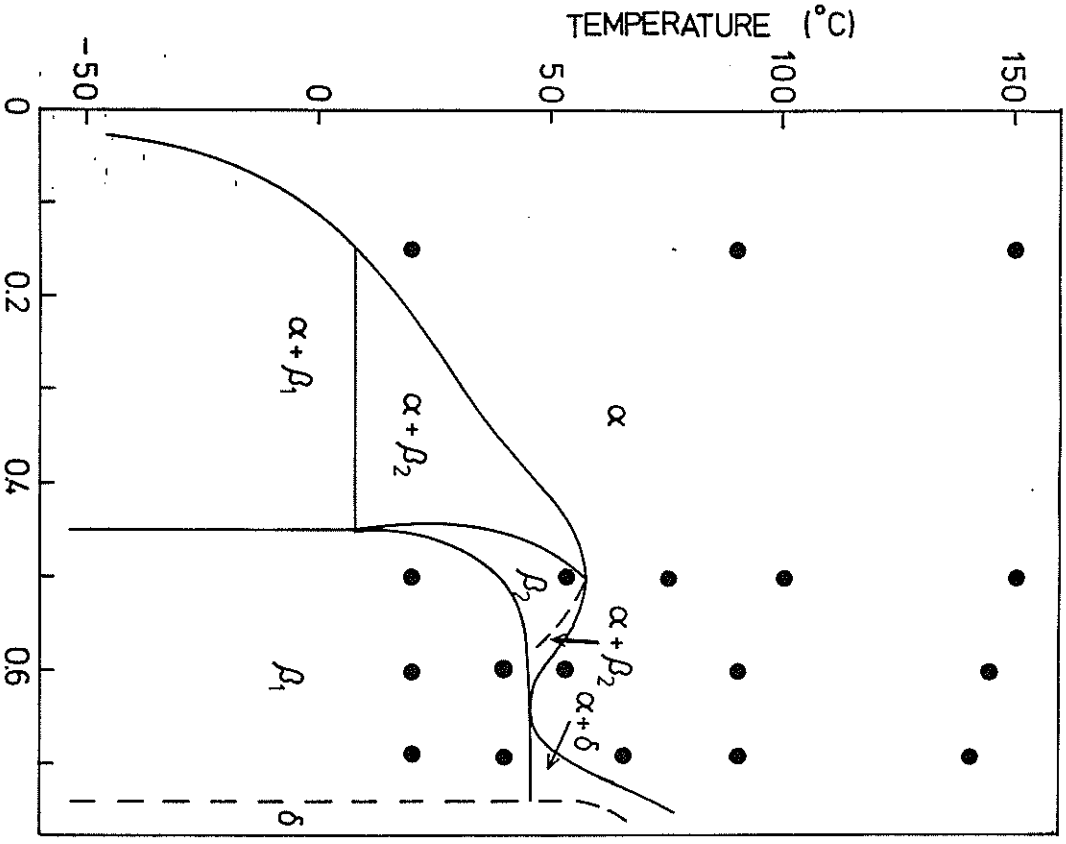
TEMPERATURE (°C)
-50
0
50
100
150
COMPOSITION (H / Ta)
0
0.2
0.4
0.6
α + β1
α + β2
α
β2
β1
α + β2
α + δ
δ

Fig. 7

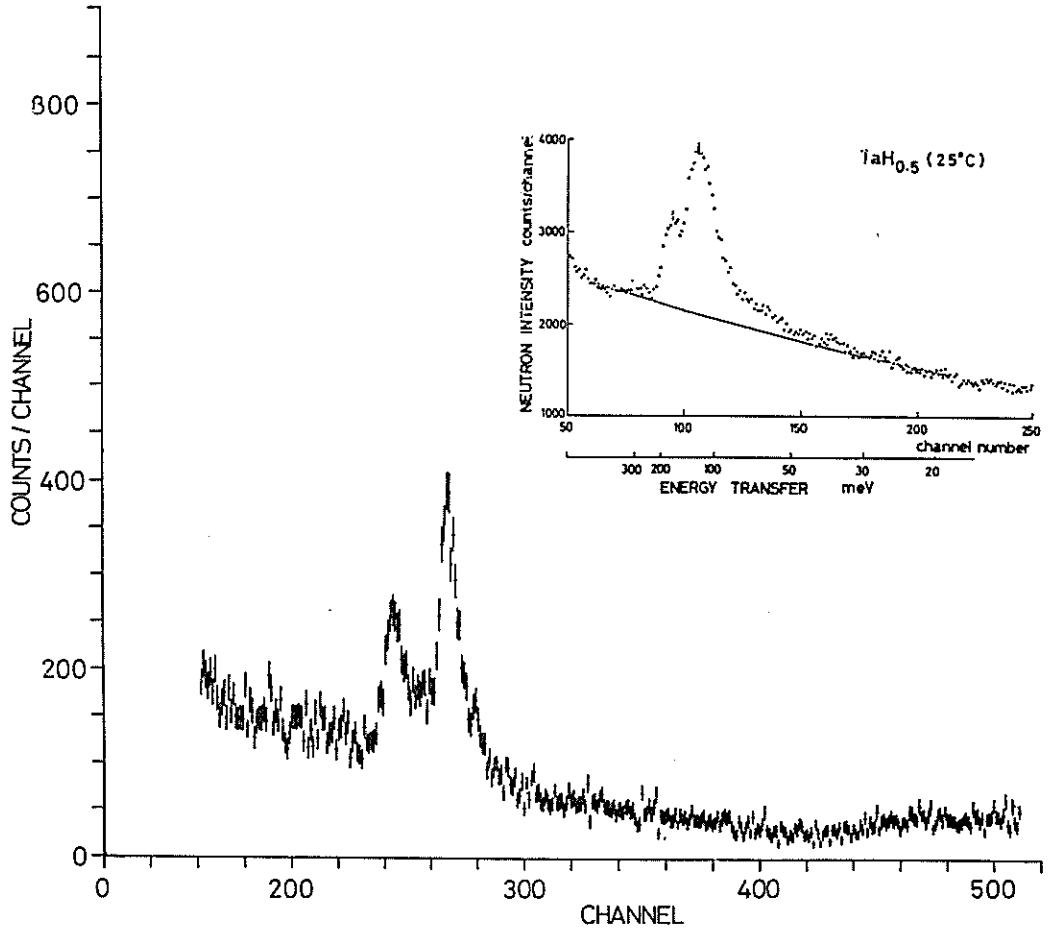
COUNTS / CHANNEL
800
600
400
200
0
0
200
300
400
500
CHANNEL
TaH0.5 (25°C)
NEUTRON INTENSITY counts/channel
4000
3000
2000
1000
50
100
150
200
250
channel number
300
200
100
50
30
20
ENERGY TRANSFER meV

Fig. 8

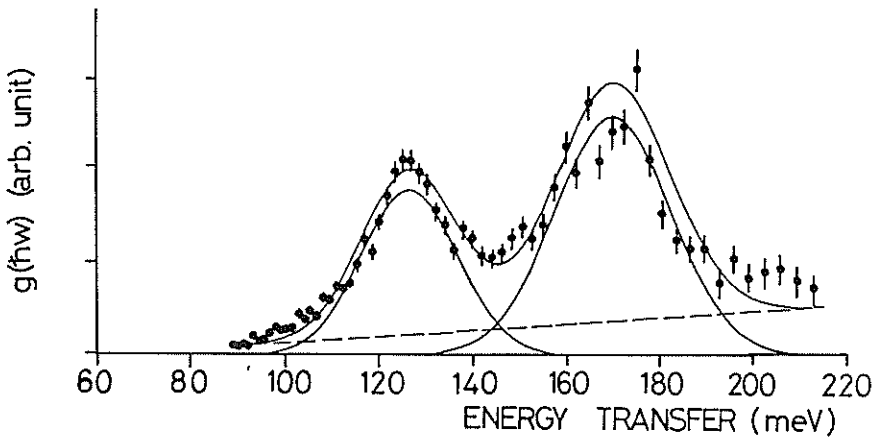

(a) GAUSSIAN FITTING

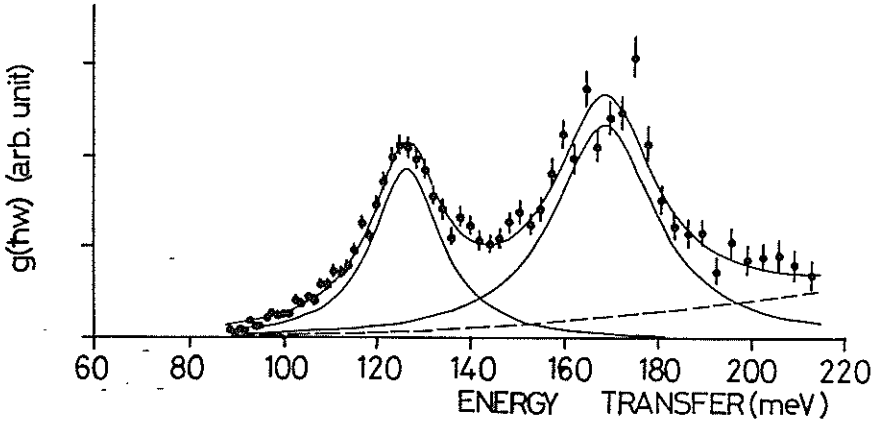

(b) LORENTZIAN FITTING

Fig. 9

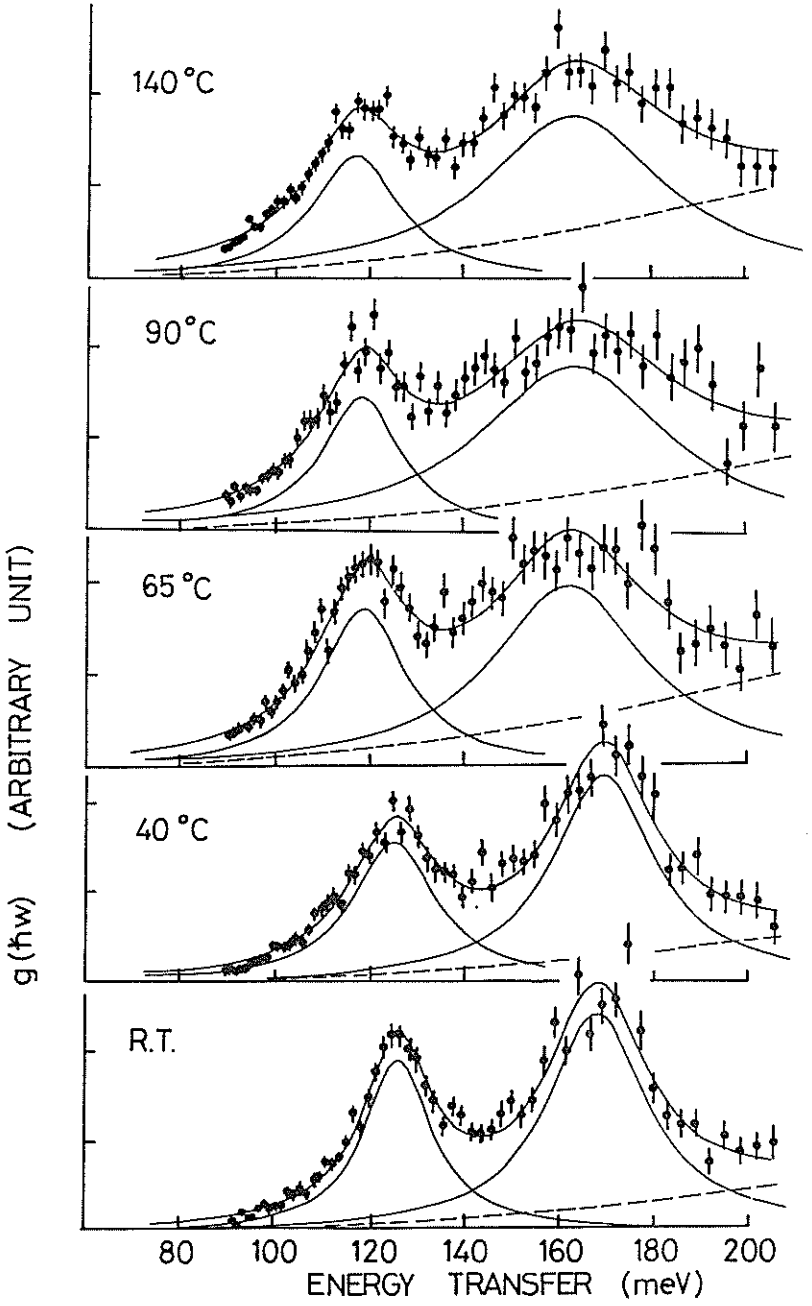

Fig. 10

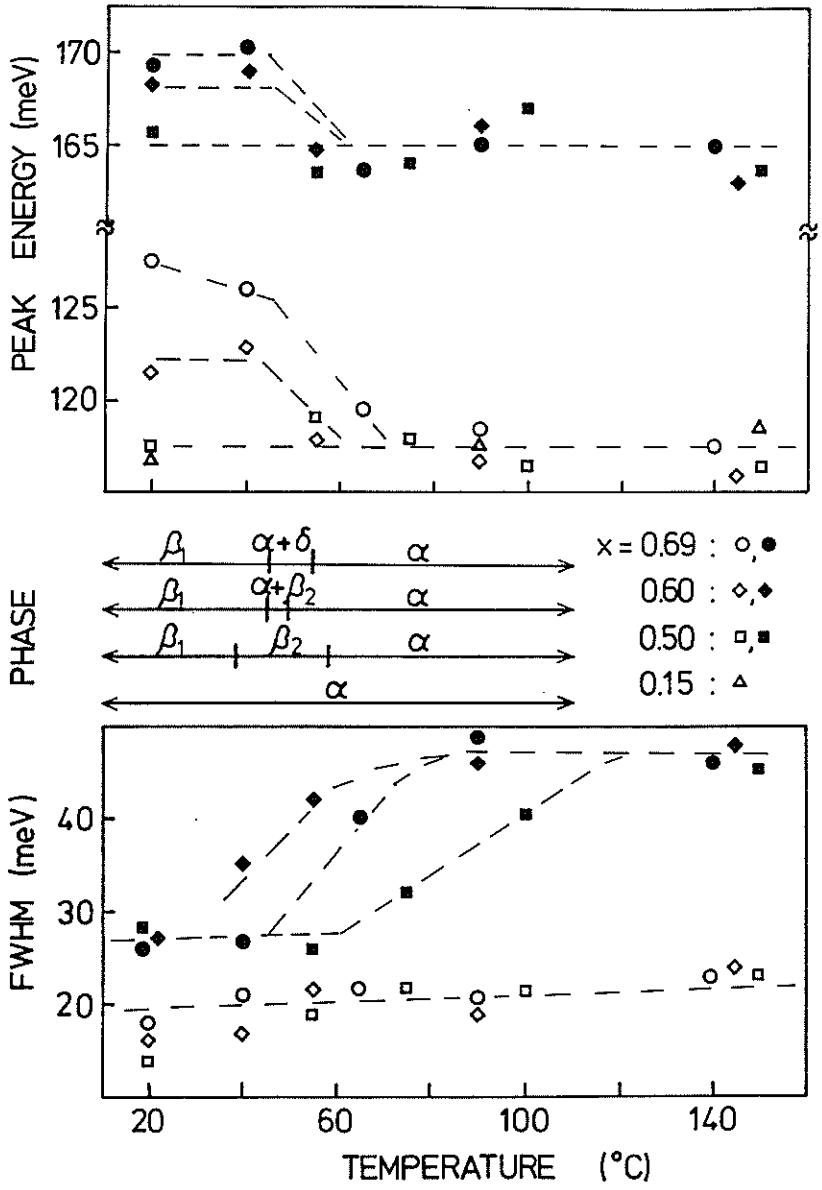

Fig. 11

6.2 Single crystal diffractometer using a position sensitive detector

N. Niimura, T. Kubota, M. Sato
Laboratory of Nuclear Science, Tohoku University
Sendai, Japan

and

M. Arai, and Y. Ishikawa
Physics Department, Faculty of Science,
Tohoku University,
Sendai, Japan

§1 Introduction

Neutron diffraction using pulsed neutron source combined with TOF method to analyse the structure of a single crystal has been widely discussed and also experimentally tested by several authors. One of the distinctive features of the neutron TOF diffractometry for a single crystal is that all the reciprocal points on the rod passing through the origin in the reciprocal space can be scanned by each burst of white neutrons. Therefore, when one dimensional position sensitive detector (PSD) is used, two dimensional areas of the reciprocal lattice space can be observed. The portion of reciprocal space accessible by use of $\lambda_{min} < \lambda < \lambda_{max}$ and $\phi_{min} < \phi < \phi_{max}$ is shown in Fig. 1. The circles with radii $1/\lambda_{min}$ and $1/\lambda_{max}$ are drawn through the origin, and the direction of the radii represents the direction of the incident beam. All reciprocal lattice points within the shaded area will simultaneously diffract and may be sampled by a PSD. Considering this distinctive feature, we can easily understand that this is promising for the measurement of intensity distribution on the reciprocal lattice space. The measurement of the thermal diffuse scattering and collection of many Bragg reflections for the structure analysis are the typical examples. But there remains many problems to be solved in this method. They are given as follows:

i) data acquisition system,

ii) how to determine both the position where, and the time when the neutron injects into the PSD,

(iii) effective display of the data,

(iv) reduction of the background, and

(v) the correction of the resolution, Lorentz factor and so on.

In order to assess this method we have made a system of a single crystal diffractometer using a position sensitive detector.

§2 The selection of the PSD

There are two types of position sensitive proportional detectors for neutrons which have been already developed and are commercially available. One is a resistive wire type and the other is a multi-wire type. The former is adopted because of the simplicity of the electronics. When we use the former PSD, position information may be obtained in one of three ways. One is to measure the rise-time of the pulse from one end only, and the second is to measure the timing of the zero crossings of the doubly differentiated pulses from each end of the proportional counter tube. The third method takes the ratio of the heights of the two pulses which has a linear relation with position of incident excitation. In order to avoid the confusions of the time measurement between the time of flight and the electronics timing, we have adopted the pulse height division method. In this method, it is necessary to measure the charge at both ends A and B(Q_A, Q_B) of the resistive electrode and then compute the distance from an end A from the expression.

$$d \sim \frac{Q_A}{Q_A + Q_B} \qquad (1)$$

Since the resistance between the ends is not so large, the difference between the times when the pulses on the electrode reach to each end is not so large. When we calculate the order of magnitude of the time, it is less than 1 μsec in the case of C ∿ 10 PF, R ∿ 50 KΩ. This does not effect to determine the time of flight of neutrons.

In our experiment the PSD made in AERE Harwell has been used. The specifications of this PSD are summarized in Table 1.

Table 1

active length	∿50cm
conversion time	20 μsec
positional resolution	< 1 cm
filling gas	^{3}He 4 atmospheres
	Quench gas 4 atmospheres
detector diameter	2.5cm
electrode wire diamter	15 μm
wire resistance	∿60 KΩ
detector capacity (calculated)	∿5 PF

The diameter of 2.5 cmϕ is proper as a detector for a single crystal diffractometer. All the diffracted neutrons should be received to correct Lorentz factor exactly.

§3 Electronics and data acquisition

The block diagram of a whole system is shown in Fig. 2.

A pre-amplifier (P A) is connected to either end of the detector. The detector bias is applied by a high voltage power supply. The pre-amplifier outputs are fed to main amplifiers (MA) which amplify and shape the signals. The shape of MA outputs is an approximate Gaussian and its full width at half maximum is about 5 μsec. The MA outputs are fed to a single channel analyzer. If an MA output is within the pre-set limits, there appears an SCA output, the shape, pulse height and width of which are rectangular, 5 V_{p-p} and 500 nsec respectively. These amplifiers and so on are settled closed to the diffractometer in the experimental room. MA and SCA outputs are transferred on 3C-2V lines to the interface in the measurement room separated about 200m far from the experimental room. Though MA outputs are attenuated about 15% while passing the 200 m 3C-2V lines, it is not necessary to correct this since the attenuation factors of the MA outputs from the both ends are nearly the same. Only when the interface accepts the SCA outputs from the both SCA and they are coincide within the pre-set time, the interface accepts the MA outputs (Q_A,Q_B) from the both MA. Q_A and Q_B are added by an analogue adder and the sum (Q_A+Q_B) is fed to a denominator input, and Q_A is fed to a numerator of the analogue divider, (Type 4291) made in Burr-Brown Research Cooperation. The speed of a division is about 10 μsec on the average. The quotient $Q_A/(Q_A+Q_B)$, which gives the required position information is fed to the analogue to digital converter (ADC)(10 bits). A 10 bits-word is converted to a 6 bits-word to save the memory capacity by considering

the spacial resolution of the PSD.

One SCA output is fed to a time analyzer which is synchronized with a burst of neutrons, and neutron time of flight is determined. The specifications of the time analyzer are summarized in Table 2.

Table 2

delay time	0 ∿ 65,536 μsec (variable)
channel width	an accordion method (4-quarters) 2 ∿ 32 μsec (variable)
total chennel	256

An accordion method saves the memory capacity very much, and the details of this method is explained in a separated paper.

The final data composed of position and time information are 14 bits-words. This shows that it is necessary to define the area of 16 KWords in the computer. 128 KW IC memory is dedicated to the diffractometer. Add one process is carried out by a soft ware.

Intensity, the position and the time of flight (3-dimensional information) are displayed on the storage graphic diaplay unit and the figures are obtained with a hard copy unit. Some examples are shown in the later section.

§4 Experiment and results

The experiment was carried out on a four-circle diffractometer installed at the 300 MeV Tohoku University electron

linac which produces pulsed neutrons.

First, the linearity and the uniformity of the PSD were tested.

i) Linearity

A vanadium cylinder (10 mm in diamter) is used as a sample. By changing the position of the solar slit in front of the PSD we have measured the linearity of the PSD. The width of the slit is 4.5 mm, and the aperture angle of the slit is about 1.8°. The relations between the obtained peak position and the PSD position where neutrons are injected are shown in Fig. 3. The abscissa indicates the position of the PSD where neutron was irradiated, and the center of the PSD is chosen as an origin. The ordinate indicates the channel of the maximum intensity of the observed peak. The linearity is quite satisfactory.

ii) Resolution

Because of the divergence of scattered neutrons, the portion of the PSD where the neutrons irradiates is larger than the width of the slit. From the aperture angle and the distance between the PSD and the sample, the beam size was estimated and was about 2.2 cm. Observed resolution was also 2.2 cm. Unless the beam collimation is improved better than 1 cm, the nominal value of the spacial resolution cannot be obtained.

iii) Uniformity

The Uniformity of the PSD was examined by using an incoherent scatterer vanadium as a sample. The results are shown in Fig. 4. Observed intensities of the both ends

decreases because of the insensitivity of the PSD and the inclined irradiation of the neutrons. The correction of the inclined irradiation effect was carried out from the geometrical consideration. The results after the correction are shown in Fig. 4. Intensities are nearly constant with the position within the statistical error.

iv) The measurement of the Bragg reflections.

The Bragg reflections of a single crystal of KBr ($7\times7\times7$ mm^3) were measured. The results are displayed on the graphic display unit during the measurement, and the figures are obtained on the hard copy unit. Several examples are shown in Fig. 5, Fig. 6 and Fig. 7. All the results are raw data. In Fig. 5 , the reciprocal lattice plane perpendicular to [100] axis is observed. In Fig. 6, the reciprocal lattice plane perpendicular to [110] axis is observed. The channel width of the time is 16 μsec in the case of Fig. 5, and Fig. 6. In Fig. 7, the observed reciprocal lattice plane is the same as the one in Fig. 6. The channel width of the time is selected as 8 μsec. The measuring time in all cases is about 1 hour. The Bragg indices are written in the figure.

v) The measurement of the atomic short range order diffuse scattering.

When there is an atomic short range order in the crystal, we can expect the diffuse scattering. The measurements of diffuse intensity distribution over reciprocal space give us the information of a short range order parameter.

First we have measured the intensity distribution of

the diffuse scattering of Cu_3Mn with a single normal counter. In order to obtain the two dimensional intensity distribution the crystal was rotated in each measurement. The results are shown in Fig. 8. The results of 45 measurements are summarized in the figure. The portion of diffuse scattering are pointed by arrows. It took 3 or 4 hours to measure one line, so the net total spent time for the measurement were about 150 hours. The final intensity distribuion over reciprocal space thus obtained after the necessary corrections are shown in Fig. 9. The details of the discussion on this result are abbreviated here.

Next we have carried out the measurement of the diffuse scattering of the same sample by use of the PSD. The result is shown in Fig. 10. It takes 6 hours to get this result. The quality of the result is much better than the one of Fig. 8. A signal to background ratio is very good, and diffuse scattering intensity distribution is clearly separated from the background. The measuring time is extremely shortened. When we have measured the same diffuse scattering without the PSD, we had to rotate the crystal, and to measure each line separately. Therefore the normalization of the each measurement was very important. However, in this case, the normalization is not necessary. Fig. 10 is a preliminary result and no correction is processed, we can say that a single crystal diffractometer combined with the PSD is a very poweful instruments.

Our results obtained by use of the PSD system are pre-

liminary. No corrections for the background, the absorption, the multiple scattering, the resolution, the Lorentz factor and so on are carried out. These corrections will be tried soon. There might be some difficulties amongst the corrections, but these would be solved mainly by the geometical consideration of the diffraction phenomena. Finally, we can conclude that a single crystal diffractometer combined with the PSD is a very powerful instrument for the study of the diffuse scattering as well as the measurement of the many Bragg reflections.

Figure Captions

Fig. 1 The portion of reciprocal space accessible by use of the PSD.

Fig. 2 The block diagram of the PSD system.

Fig. 3 The linearity of the PSD.

Fig. 4 The uniformity of the PSD.

Fig. 5 The reciprocal lattice plane of KBr perpendicular to [100] axis observed by use of the PSD.

Fig. 6 The reciprocal lattice plane of KBr perpendicular to [110] axis observed by use of the PSD.

Fig. 7 The reciprocal lattice plane of KBr perpendicular to [110] axis obtained by use of the PSD.

Fig. 8 Intensity distribution of the diffuse scattering of Cu_3Mn measured by use of the normal detector.

Fig. 9 Intensity distribution over reciprocal space of Cu_3Mn

Fig. 10 Intensity distribution of the diffuse scattering of Cu_3Mn measured by use of the PSD.

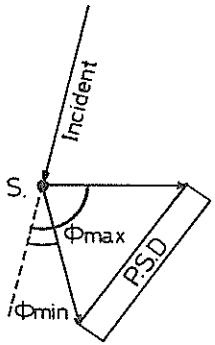

$k_{min} = 2\pi/\lambda_{min}$

$k_{max} = 2\pi/\lambda_{max}$

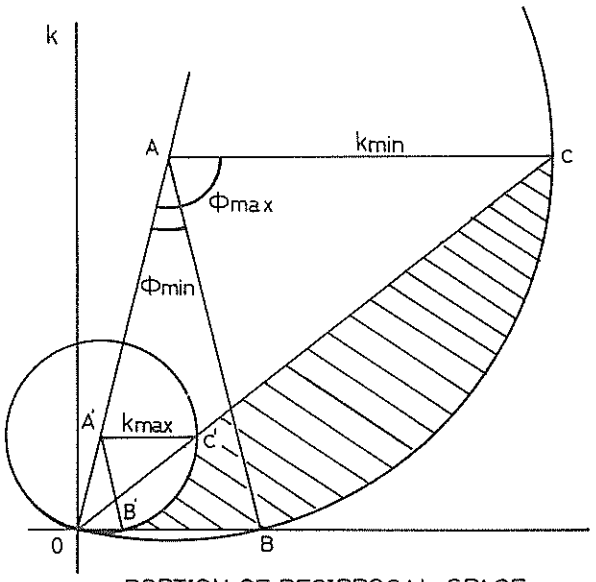

PORTION OF RECIPROCAL SPACE
ACCESSIBLE BY USE OF $\lambda_{min} < \lambda < \lambda_{max}$
AND $\Phi_{min} < \Phi < \Phi_{max}$

Fig. 1

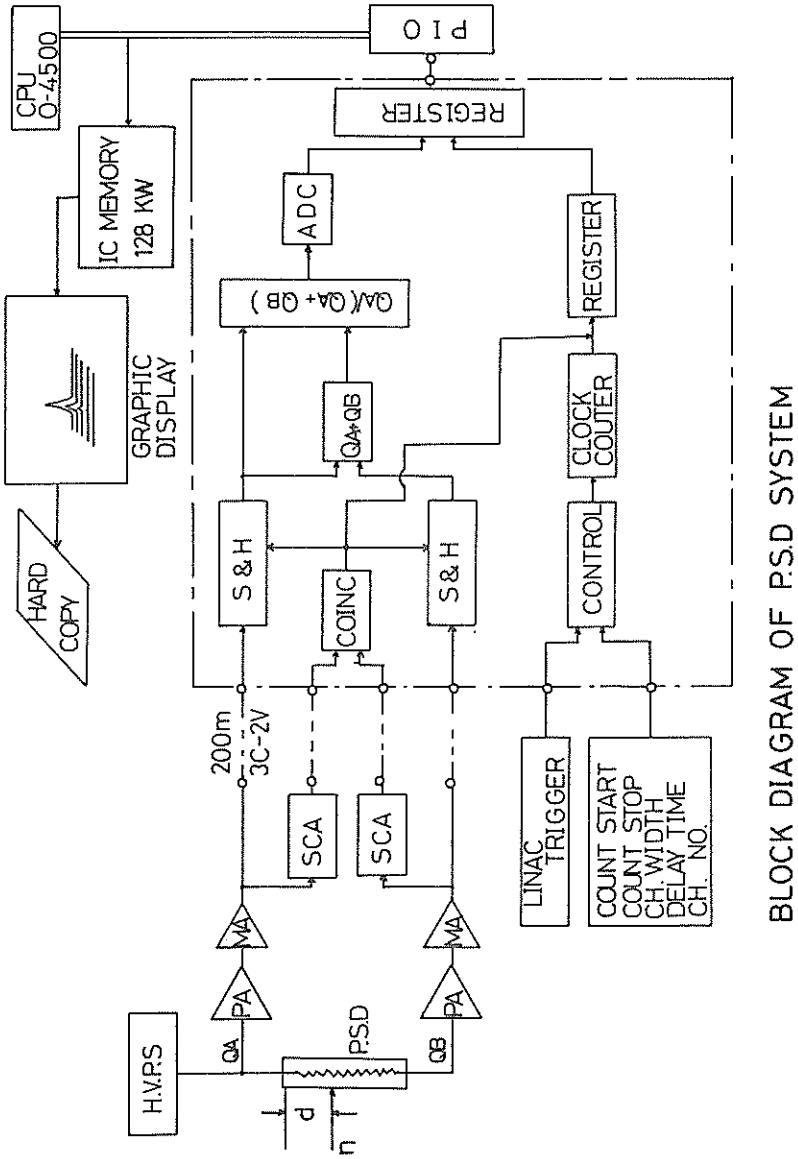

BLOCK DIAGRAM OF P.S.D SYSTEM

Fig. 2

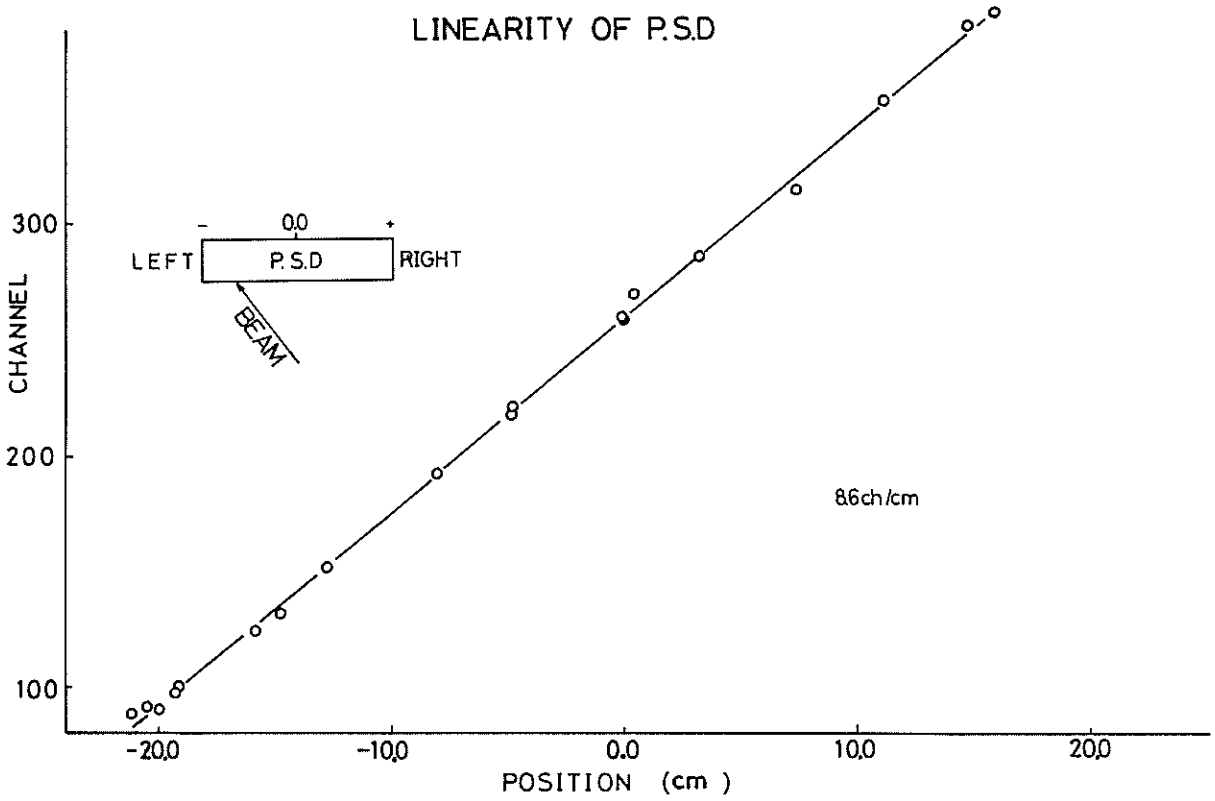
LINEARITY OF P.S.D
CHANNEL
300
200
100
0.0
LEFT
P.S.D
RIGHT
BEAM
8.6ch/cm
-20.0
-10.0
0.0
10.0
20.0
POSITION (cm)

Fig. 3

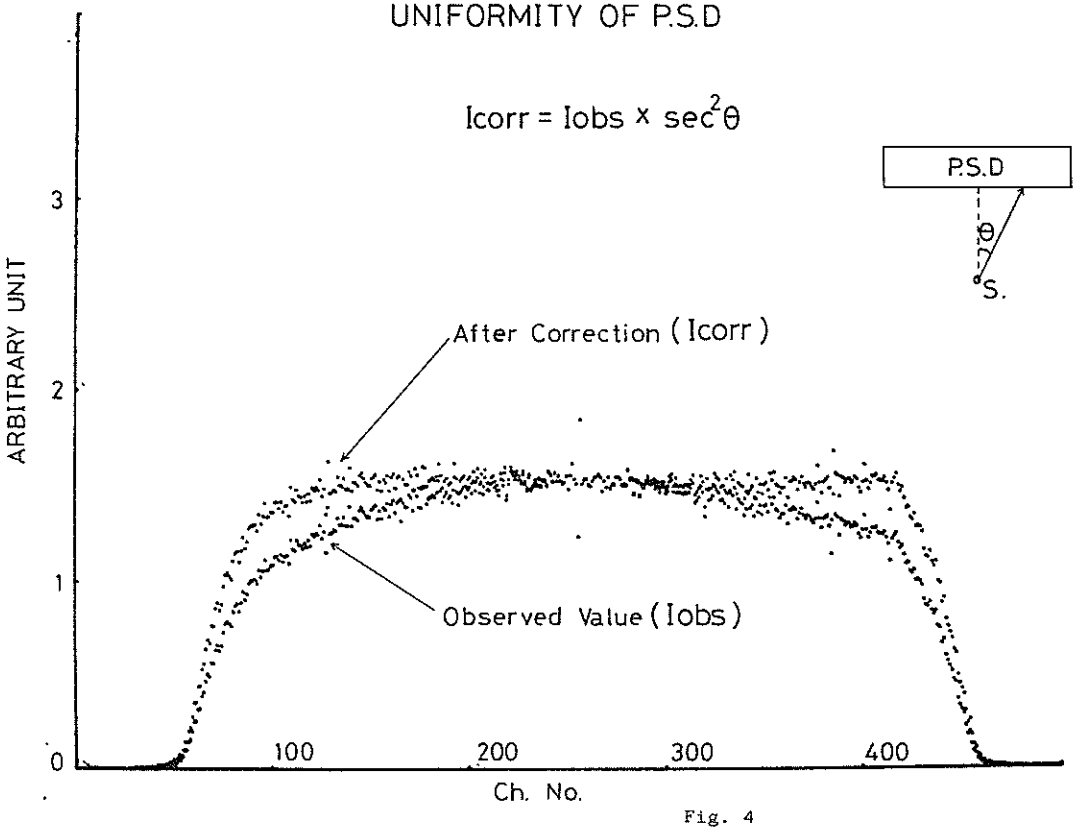
UNIFORMITY OF P.S.D
Icorr = Iobs x sec²θ
P.S.D
θ
S.
ARBITRARY UNIT
3
2
1
0
After Correction (Icorr)
Observed Value (Iobs)
100
200
300
400
Ch. No.

Fig. 4

KBr

Rotation axis: [100]

Ch. width: 16 μsec

Delay time: 500 μsec

-217-

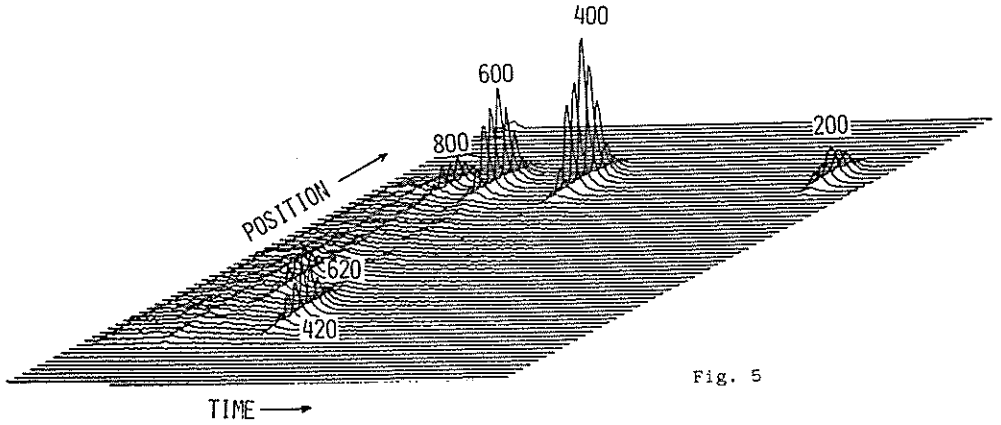

Fig. 5

KBr

Rotation axis: [110]

Ch. width: 16 μsec

Delay time: 500 μsec

-218-

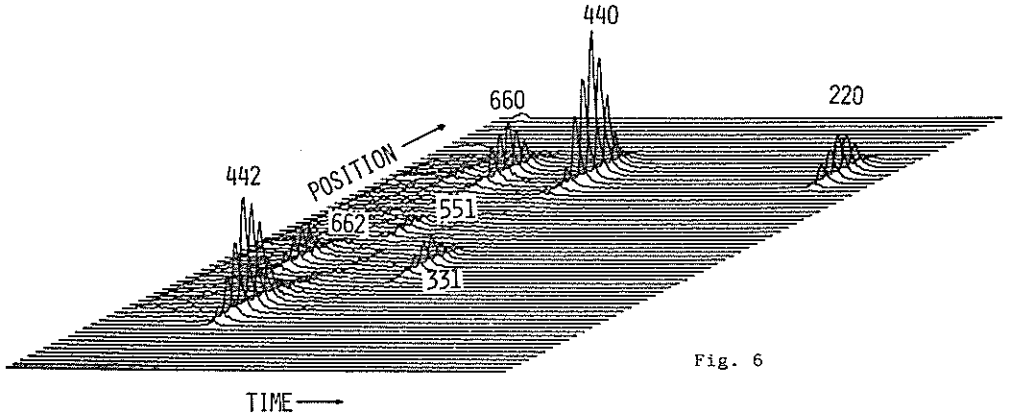

Fig. 6

KBr

Rotation axis: [110]

Ch. width: 8 μsec

Delay time: 500 μsec

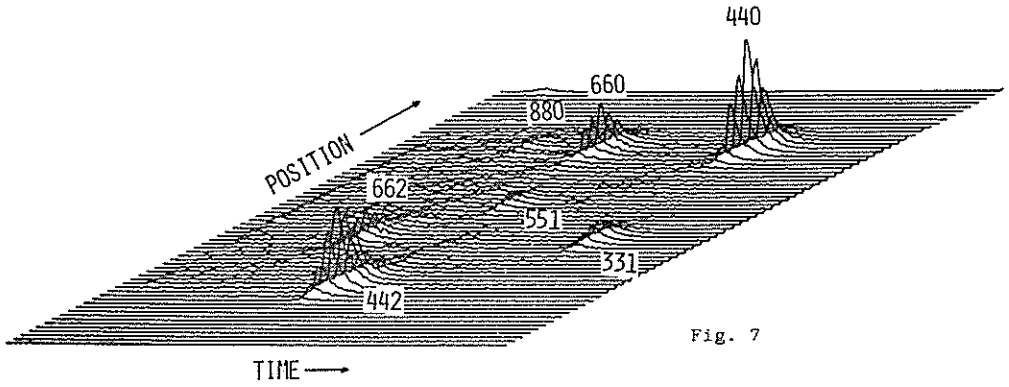

Fig. 7

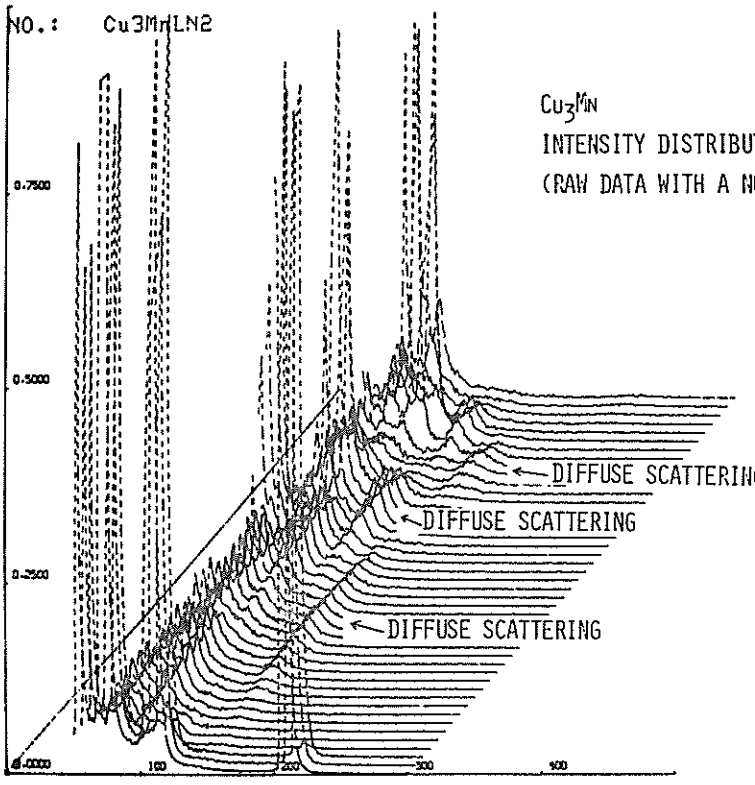

Cu_3Mn

INTENSITY DISTRIBUTION OF DIFFUSE SCATTERING

(RAW DATA WITH A NORMAL DETECTOR)

Fig. 8

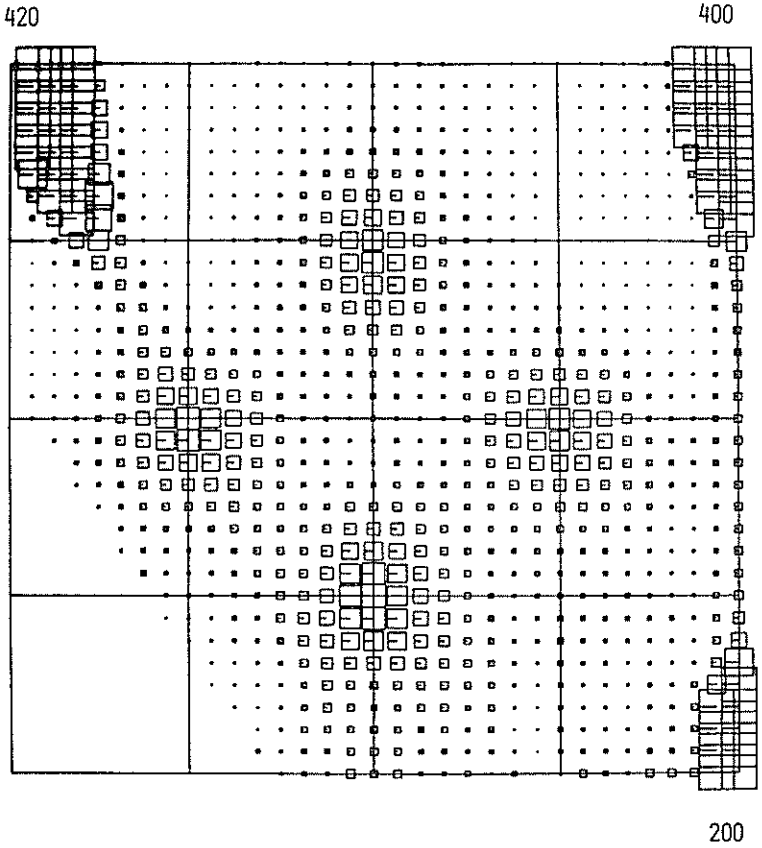

Cu_3Mn

INTENSITY DISTRIBUTION OF DIFFUSE SCATTERING

(AFTER CORRECTIONS OF ANSORPTION & MULTIPLE SCATTERING)

Fig. 9

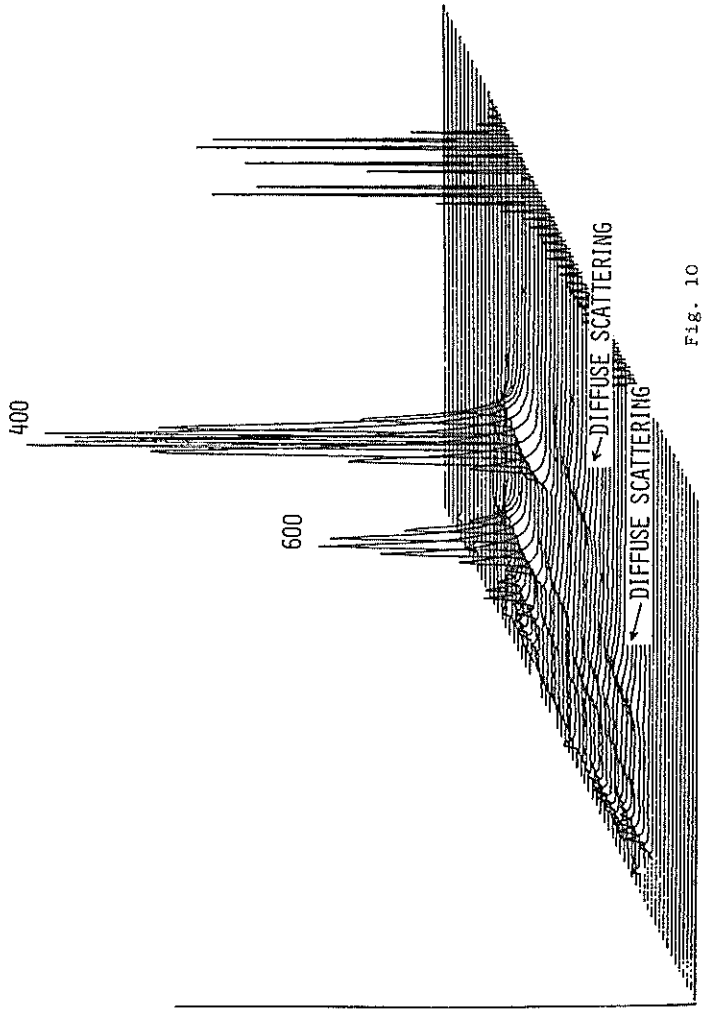

Cu_3Mn

INTENSITY DISTRIBUTION OF DIFFUSE SCATTERING

(RAW DATA WITH PSD)

Fig. 10

6.3 Neutron Diffraction Study of Structure Change in a Process of Solidification from a Supercooling State

Y. Ishikawa, S. Ikeda*, T. Shinohe and N. Niimura†

Physics Department and †Laboratory of Nuclear Science
Tohoku University, Sendai

1. Introduction

This paper describes a preliminary experimental result of neutron diffraction from liquid metal Sn in a process of solidification from supercooling state. The experiment was attempted in order to establish the experimental technique for measuring the atomic structure in non-equilibrium state induced by rapid change of the temperature. The T-O-F diffraction method incorporated with the pulsed neutron source is one of the most promissing method to study these non equilibrium state[1] and some trials as the study of structural change in a process of polarization reversal in a ferroelectric crystal $NaNO_2$[2] have been performed using this technique.[1] The study of non-equilibrium state induced by rapid temperature change has the widest field of research but it has a technical difficulty of keeping the temperature of the sample homogeneous in non-equilibrium state. We paid an attention that the solidification process from the supercooling liquid state occurs homogeneously and reproducibly in the sample and the structural change of liquid tin in a process of solidification from the supercooling state has been studied using the Tohoku pulsed neutron source.[3),4)] This paper describes the outline of

---

* Present address: National Laboratory for High Energy Physics, Tsukuba, Ibaraki

the technical development and a preliminary experimental result. The problem is also quite interesting from the physical point of view, because some amorphous materials as Ge made by rapid quenching from the liquid state have different atomic structure from that in liquid.

2. Experimentals

The block diagram of the measuring system is displayed in Fig.1. The metal Sn of about 21 gr was melted in a thin quartz crucible, 10 mm in diameter by using a tungsten wire sealed in a quartz tube (Shinku Ricō, N lamp) with a radiation reflector to focus the radiation on the sample. The sample temperature was detected by a Almel-Chromel thermocouple inserted in the sample using a digital voltmeter, which was read in micro-computer COMPO 80 through a PIO system. Then the heater was controlled by the order of the micro computer following the program stored in the computer. One example is that; when the sample temperature exceeds T_1 in Fig.2, the heater current was switched off, then the sample was naturally cooled to T_2 where sudden solidification starts. The time of the temperature change was detected. The TOF total scattering from the sample was measured by a conventional spectrometer, but the data from different time intervals as between t_0 and t_1, t_1 and t_2 etc. in Fig.1 are accumulated in different memory areas in the mini-computer (OKITAC 4500) through a signal distributor and the process of the cycle from t_0 to t_5 was repeated until the statistics of the data was increased. If the time intervals are selected as given in Fig.2, we found that the final stage starting from t_4 is in the solid state. The variation of T_2, ΔT_2 is almost 1.5 % of T_2 through the whole experiment and the temperature gradient in the sample during this cycle is ±0.5 deg. Therefore we are convinced that the result obtained is meaningfull.

3. Experimental results and discussion

The experimental results obtained are displayed in Fig.3 after converting them to the scattering law S(Q). They are normalized to that of Vanadium. The scattering from the sample container was not yet subtracted. If we compare the pattern for the liquid state with that for the Zone 1, we find that a small shoulder at right hand side of the first peak is clearly depressed in the Zone 1, while, in approaching to the solid state (Zone 4), the shoulder is again developing into a Bragg peak. The pattern in Zone 1 could not be reproduced by superposition of patterns of liquid and solid states. Therefore, a simple picture that the solid state coexists with the liquid state without modifying each structure in the solidification process does not seem correct. The result suggests that a metastable state where the atomic order is destroyed more easily than in the liquid state is realized before the solid state starts to develop in the sample.

Although the experiment performed is still in a preliminary stage, the results obtained suggest that this kind of measurement is quite promissing , having many applications. The detailed measurement as well as the results of the analysis will be soon published eleswhere.

References

1) N. Niimura and M. Muto: Nucl. Instrum Methods 126 (1975) 87.

2) N. Niimura and M. Muto: J. Phys. Soc. Japan 35 (1973) 628.

3) Y. Ishikawa, S. Ikeda and N. Niimura: Research Report of Laboratory of Nuclear Science, Tohoku Univ. 11 (1978) 22.

4) S. Ikeda, N. Niimura and Y. Ishikawa: ibid 12 (1978) 55.

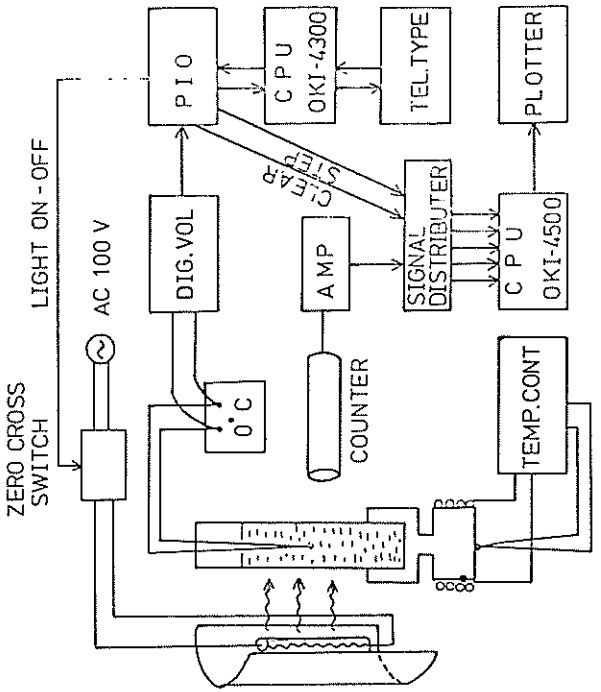

Fig. 1

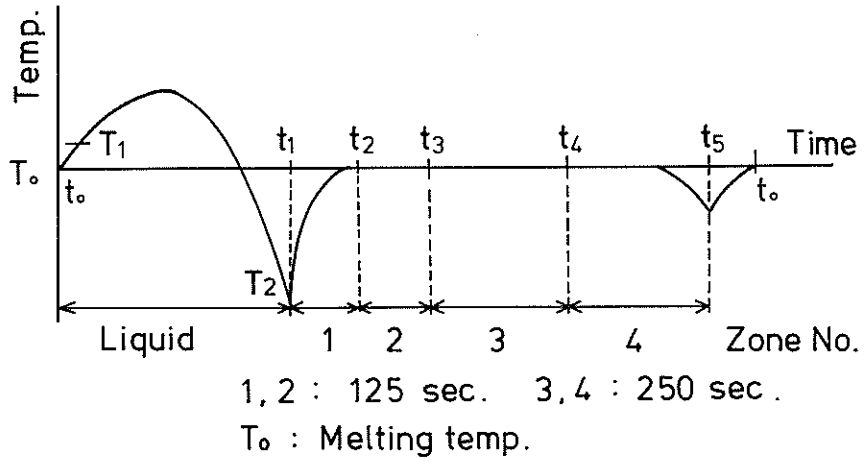

1, 2 : 125 sec. 3, 4 : 250 sec.

T_0 : Melting temp.

Fig. 2

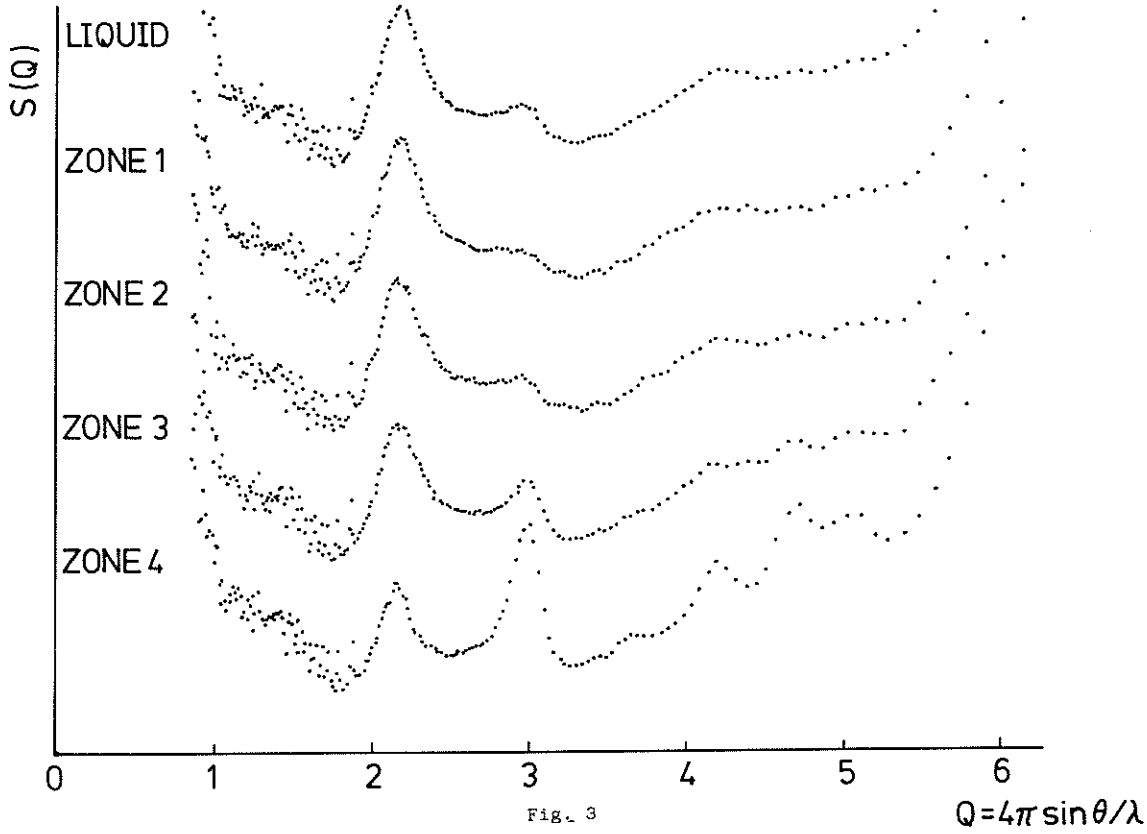

Fig. 3